NANOCOMPOSITE PASTE FOR THERMAL AND MECHANICAL BONDING

BY

TINGTING ZHANG

BS, Nanjing University, 2012

DISSERTATION

Submitted in partial fulfillment of the requirements for
the degree of Doctor of Philosophy in Materials Science & Engineering
in the Graduate School of
Binghamton University
State University of New York
2017

المنارة للاستشارات

www.manaraa.com

ProQuest Number: 10278033

All rights reserved

INFORMATION TO ALL USERS
The quality of this reproduction is dependent upon the quality of the copy submitted.

In the unlikely event that the author did not send a complete manuscript
and there are missing pages, these will be noted. Also, if material had to be removed,
a note will indicate the deletion.

ProQuest 10278033

Published by ProQuest LLC (2017). Copyright of the Dissertation is held by the Author.

All rights reserved.
This work is protected against unauthorized copying under Title 17, United States Code
Microform Edition © ProQuest LLC.

ProQuest LLC.
789 East Eisenhower Parkway
P.O. Box 1346
Ann Arbor, MI 48106 – 1346

المنارة للاستشارات
www.manaraa.com

© Copyright by Tingting Zhang 2017

All Rights Reserved

للاستشارات المنارة

www.manaraa.com

Accepted in partial fulfillment of the requirements for
the degree of Doctor of Philosophy in Materials Science & Engineering
in the Graduate School of
Binghamton University
State University of New York
2017

May 1, 2017

Dr. Howard Wang, Faculty Advisor
Department of Materials Science of Engineering, Binghamton University

Dr. Guangwen Zhou, Chair and Faculty Advisor
Department of Materials Science of Engineering, Binghamton University

Dr. Bahgat Sammakia, Member
Department of Mechanical Engineering, Binghamton University

Dr. Seungbae Park, Member
Department of Mechanical Engineering, Binghamton University

Dr. William Chen, Member
Senior Technical Advisor, ASE Group, USA

Dr. Xiaohua (Edward) Li, Outside Examiner
Department of Electrical and Computer Engineering, Binghamton University

المنارة للاستشارات
www.manaraa.com

Abstract

Heat dissipation is a major challenge in high performance electronic devices. Current thermal interface materials (TIMs) have either low conductivity, such as conventional thermal greases, or high costs, such as solder materials. We address TIM challenges by fabricating resin-free nanocomposite TIM paste that integrates silver nanoparticles (AgNPs), Ag nanoflakes (AgNFs) and copper micro-particles (CuMPs). The nanocomposite TIMs optimize both the bulk and interfacial thermal performances; CuMPs with a particle size of 1~10 μm offer the assurance of high bulk thermal conductivity (*k*), while AgNPs with a diameter of 3~8 nm and ~10 nm thick AgNFs provide the flexibility and the bondage in interfacial engineering. TIM assemblies have been prepared upon sintering at temperatures from 125 to 225 ^{o}C for 5~20 min. Morphological and compositional analyses have shown percolated network structures connected with fused AgNPs and AgNFs in TIMs and strong metallic bonds formed with CuMPs and the substrates, resulting in good mechanical and thermal performance and excellent thermo-mechanical reliability. Steady state heat flow and flash diffusivity measurements have shown *k* of nanocomposite TIMs in the range of 15~140 W/mK, and the contact resistance as low as 1.3×10^{-6} m^2K/W, comparable to high-end solder TIMs. Using analytical models, the role of void volume fractions and interfacial resistance in the hybrid composites on thermal conductivity has been assessed. Data shows the particularly contiguous network structure favors the symmetric model. Shear and tensile tests have shown that both bond strength and relative energy density of TIMs increase with higher sintering temperature

المنارة للاستشارات

www.manaraa.com

and longer sintering time. The thermo-mechanical reliability of hybrid TIMs bonding solid substrates with coefficients of thermal expansion (CTE) differences exceeding 15 ppm/^{o}C has been tested. The assemblies have gone through more than 10^4 cycles of thermal shocks between -50 and 150 ^{o}C without failure. This study has shown the promises of the hybrid TIMs for thermal, mechanical and thermo-mechanical applications in electronics packaging.

المنارة للاستشارات
www.manaraa.com

Acknowledgements

I would like to take this opportunity to thank my committee, my colleagues, my friends and my family for their assistance and full support through my Ph.D studies.

I wish to express my heartfelt thanks to Prof. Howard Wang for his thoughtful guidance, insightful suggestions and warm encouragement on the successful completion of this research. Prof. Wang has been a great mentor to develop my interests in the nano-technology fields and broaden my knowledge and perspective of thermal interface materials on electronics packaging.

Many thanks, also, to Prof. Guangwen Zhou, Prof. Baghat Sammakia, Prof. Seungbae Park and Dr. William Chen for being on my dissertation committee and for providing valuable comments and helpful suggestions to my research work. I would also like to thank Prof. Xiaohua (Edward) Li for serving as the outside examiner for my dissertation defense.

I would like to thank Dr. Lawrence Lehman, Dr. Dae Young Jung, Dr. Anju Sharma and Mr. William Butler at the Analytical and Diagnostics Laboratory (ADL) and Dr. Stephen Cain at the Integrated Electronics Engineering Center (IEEC), for their valuable ideas and insights on the experimental studies of this research.

I would also like to give my special thanks to all my co-workers and friends in Binghamton University: Dr. Yuping He, Dr. Lianfeng Zou, Dr. Liwei Huang, Dr. Drew Davidson, Dr. Xiaoming Chen, Dr. Sandeep Mallampati, Dr. Ruiyang Liu, Dr. Wenhui

المنارة للاستشارات

www.manaraa.com

Zhu, Mr. Feilin Gou and Mr. Xianhu Sun, for their help and recommendations whenever needed in my school work and life. Thanks to Dr. Hongwen Zhang from Indium Corporation for providing the copper microparticles for our TIM preparation and his valuable technical expertise. We have had ups and downs during this long journey, and I believe that our friendship and passion for life will carry into the future chapters of our lives.

Last but not the least, I would like to thank my parents and my only brother for their firm emotional support and encouragement regardless of the location and time. They have always shown unconditional and deep love for me, making this research become a reality.

This work was supported financially by the Small Scale Systems Integration and Packaging Center (S^3IP) and the Integrated Electronics Engineering Center (IEEC) in Binghamton University.

المنارة للاستشارات
www.manaraa.com

Table of Contents

List of Tables x

List of Figures xi

Chapter 1 Introduction 1

1.1 Current thermal interface materials (TIMs) 1

1.2 Key properties of TIMs 7

1.2.1 Mechanical properties 7

1.2.2 Reliability properties 9

1.2.3 Thermal properties 12

1.3 Thermal conductivity measurements 15

1.4 Theoretical effective thermal conductivity models 21

1.5 Chapter flow 26

Chapter 2 AgNPs synthesis and sintering 33

2.1 Introduction 33

2.2 Experiments 36

2.3 Results and discussions 38

2.4 Conclusion 41

Chapter 3 Nanocomposite TIM assembly preparation and characterizations 49

المنارة للاستشارات

www.manaraa.com

3.1 Introduction 49

3.2 Experiments 50

3.3 Results and discussions 52

3.4 Conclusion 55

Chapter 4 Mechanical and thermo-mechanical properties of the hybrid TIM assemblies 62

4.1 Introduction 62

4.2 Experiments 64

4.3 Results and discussions 66

4.4 Conclusion 70

Chapter 5 Thermal conductivity of the hybrid TIMs 82

5.1 Introduction 82

5.2 Experiments 85

5.3 Results and discussions 89

5.4 Conclusion 93

Chapter 6 Conclusion and future work 107

6.1 Conclusion 107

6.2 Future work 108

References 110

المنارة للاستشارات

www.manaraa.com

List of Tables

Table 2-1 The parameters for some possible chemicals in AgNPs 42

Table 5-1 Thermal results from steady state measurement in figure 5-8 94

Table 5-2 Parameters and k result from diffusivity method 95

Table 5-3 Parameters for thermal diffusivity calculation 95

المنارة للاستشارات

www.manaraa.com

List of Figures

Figure 1-1 Scheme of contact interfaces at the joint of two materials without TIMs use (Note: R_{int} is the thermal contact resistance at the interface.). The micro and macro roughness of the joint of two surfaces can be seen even under the loading pressure, and most interface area is separated by air filled gaps. 29

Figure 1-2 Schematic illustration for single lidded flip chip packaging [8], where a heat sink is attached to the lid of a heat spreader. In the commercial microelectronics packaging, TIM1 is the TIM to bond a chip with the heat spreader, where the expensive high-end solder is usually used. TIM2 is the TIM between the heat spreader and the heat sink, which is what most researchers have been work on. 30

Figure 1-3 Schematic of the effective thermal resistance at the interfaces of the TIMs, R_{TIM} consists of the bulk resistance R_{bulk}, and two contact resistances at the interfaces R_{c1} and R_{c2}. 31

Figure 1-4 Comparisons of the novel hybrid TIMs in this study with various current TIMs on their thermal properties (k and R_c) as discussed in chapter 1. The cheaper polymeric TIMs have poorer thermal performances comparing with the expensive solders. High-performing CNTs and graphene cannot be applied to the market yet. The thermal conductivity of the hybrid TIMs in this study can compare to the high-end solder TIMs and their contact resistance achieves as low as that of the best thermal greases. 32

Figure 2-1 SEM image of AgNPs (a) shows that AgNPs have a uniform size, and TEM characterizations (b) show AgNPs have a size around 6 nm with a narrow distribution of ± 2 nm. 43

Figure 2-2 SEM characterization of AgNPs synthesized using a different amine with shorter alkane chains as surfactant, showing the size is less uniform ranging from tens to hundreds of nanometers. 44

Figure 2-3 TGA analysis of smaller and larger AgNPs, showing isothermal weight loss in nitrogen upon heating. Both have three stages of weight loss, but the smaller AgNPs lose much more weight than the bigger AgNPs, which is consistent with the fact that smaller particles trap more surfactant and solvent. 45

المنارة للاستشارات
www.manaraa.com

Figure 2-4 Schematic illustration of metal nanoparticle sintering upon heating. The sequence of the chemicals leaving the system with increasing temperature is solvent, free surfactant and bonded surfactant. After this, the nano-sized particles start to diffuse to form bigger ones, corresponding to the law of thermodynamics. 46

Figure 2-5 XRD spectra of neat and sintered AgNPs at 120 ºC for different durations. According to the calculation based on the Scherrer equation, the AgNPs grow to 22 nm after 1 min heating, and to 65 nm after 5min from 10 nm as synthesized. 47

Figure 2-6 1D in-situ SAXS images for neat AgNPs at 180 ºC, showing that AgNPs grow larger with longer heating times, for the peak shifts to a lower Q value, which is accordant with the XRD result in figure 2-5. 48

Figure 3-1 SEM images of hybrid TIM pastes of 10 µm CuMPs and AgNPs with a mass ratio of 7:3 sintered at 125 ºC (a), 150 ºC (b), 175 ºC (c) for 20 min; and at 200 ºC for 5 min (d), 10 min (e), and 20 min (f), showing the contiguous networks connected through fused AgNPs. 56

Figure 3-2 SEM images in higher magnification of hybrid TIM pastes of 10 µm CuMPs and AgNPs with a mass ratio of 7:3 sintered at 125 ºC (a), 150 ºC (b), 175 ºC (c), and 200 ºC (d) for 20 min, showing AgNPs grow larger and are distributed on the surfaces of and in between CuMPs. The higher the sintering temperature with the same sintering duration time, the more the large Ag particles grow. 57

Figure 3-3 SEM images of hybrid TIM pastes sintered at 200 ºC for 20 min of CuMPs and AgNFs with a mass ratio of 6:4 (a) and (b), of CuMPs, AgNFs, and AgNPs with a mass ratio of 6:2:2 + 2 % P4VP by weight (c) and (d). Fig. (b) and (d) are the magnified images corresponding to (a) and (c), showing the contiguous networks connected through fused AgNFs and AgNPs. 58

Figure 3-4 SEM and EDX analysis of sintered TIMs consist of CuMPs, AgNFs and AgNPs with a mass ratio of 6:2:2. The EDX data shows that copper is dominant at the large particles, and silver is dominant at the interval of large particles, which helps confirm the distribution of metal particles within paste. 59

Figure 3-5 The SAM image (a) and the X-ray imaging (b) of the TIM layer in between two copper foils as the substrates. The TIM paste contains 10 µm CuMPs and AgNPs and was sintered at 200 ºC for 20 min. Both images show the uniform and non-uniform parts of the sintered TIM layer, and voids can be seen in the assembly. 60

Figure 3-6 XRD patterns for a sintered TIM paste consisting of CuMPs and AgNPs with a mass ratio of 7:3, and sintered at 200 ºC for 20 min. The TIM spectrum is composed of

المنارة للاستشارات
www.manaraa.com

both neat Cu and Ag peaks, and there is no appearance of new peaks, implying no formation of other significant phases. 61

Figure 4-1 Schematic of five typical loading categories on the materials: tension, compression, bending, shear and torsion, which are classified by where the force loaded on the materials and the directions of the force. 71

Figure 4-2 Schematic of the Dage series 4000 and 4000+ bond tester, which can perform shear, pull and push testing, covering all test applications. With the assistance of the microscope, it is ideally suited for macro positioning. 72

Figure 4-3 Schematic illustration of the TIM sample design for shear test (a) and an example of the shear stress-strain result (b). In the sandwich sample for shear test, the larger Cu foil is about 100 µm thick, while the smaller Cu foil piece is about 1 mm thick and with an area of about 3 mm x 3 mm. The TIM layer in between is about 50~100 µm thick. .. 73

Figure 4-4 Schematic illustration of the TIM sample design for tensile test (a) and an example of tensile stress-strain result from the wire pull mode (b). The TIM assembly for tensile test is prepared with two identical 100 µm Cu foils as the substrates, and the size of the TIM paste is about 3 mm x 10 mm. The TIM layer between the two cooper foils is also about 50~100 µm thick. 74

Figure 4-5 Thermal profiles of 50 thermal cycles from -50 to 150 ºC in the Espec TSE-11-A thermal shock chamber. The duration of each cycle is set for 20 min with the sample 10 min at the cold compartment and then 10 min in the hot compartment. 75

Figure 4-6 Ultimate strength comparisons of the TIM samples at different sintering temperatures for 20 min (a), and of the TIM samples at 200 ºC for different sintering times (b). The two compositions are AgNPs with 3 or 10 µm CuMPs with a mass ratio of 3:7. The higher the sintering temperature and the longer the sintering time, the higher the strength needed to take the samples to failure. 76

Figure 4-7 Comparison of the relative energy density of the TIM assemblies containing AgNPs and 10 µm CuMPs with a mass ratio of 3:7, sintered at different temperatures for 20 min (a), and at 200 ºC for different times (b). The higher sintering temperature and the longer sintering time makes the TIM assemblies tougher. 77

Figure 4-8 Comparison of the relative integral energy density of the TIM assemblies after different numbers of thermal cycles of -50 and 150 ºC. The TIM contains AgNPs and 10µm CuMPs (a) 3 µm CuMPs (b) with a mass ratio of 3:7, and both TIM samples were sintered at 200 ºC for 10 min. The relative integral energy density of the TIM sample decreases with the thermal cycling, and decreases more quickly at the first few thermal cycles. 78

المنارة للاستشارات
www.manaraa.com

Figure 4-9 SAM images for the TIM paste containing 10 μm CuMPs sintered at 200 °C for 20 min as prepared (a), and after 50 thermal cycles (b). After 50 thermal cycles, the internal structure of the TIM layer becomes decreasingly uneven, and some small voids disappear. 79

Figure 4-10 Schematics of the mismatched TIM assembly using Cu foil and invar foil as the two substrates (a), and the shear stress-strain curves for the thermo-mechanical performance of the mismatched TIM pastes containing 10 μm CuMPs (b) and 3 μm CuMPs (c). Both mismatched TIM pastes can survive 10000 thermal cycles between -50 and 150 °C without failure. 80

Figure 4-11 SEM investigation on the broken TIM sample sintered at 200 °C for 20 min containing 3 μm CuMPs and AgNFs and AgNPs with a mass ratio of 6:2:2 (a) and (b), containing the same metal materials and 2 % polymer binder (c) and (d). The TIM sandwich samples were forced to separate with a strong external force. (a) and (c) are for the images of the areas without TIMs seen by naked eyes, (b) and (d) are for the images for the areas with most TIMs. The TIM assemblies fail either at the interfaces of Ag particles or between CuMPs and Ag particles. 81

Figure 5-1 Schematic illustration for the steady state thermal measurement setup The TIM is placed in a steady flow of heat established in a rod by a steady heat source and a steady heat sink (cooling system). Six temperatures were measured along the rod, and the temperature drop across the TIM can be estimated through fitting the 6 measured temperatures. The temperature gradient in the rod and the known k of the rod give the heat flow in the rod. The ratio of ΔT to heat flux Q is the unit-area thermal contact resistance R" of the TIM. 96

Figure 5-2 Theoretical plot of effective thermal resistance vs. BLT, where the reciprocal of the linear slope is the effective k of the TIM, and the y intercept is the interface thermal contact resistance. 97

Figure 5-3 Measuring principle of flash diffusivity method. An energy pulse is applied to the front face of the planar-shaped sample with a thickness of L and an initial temperature T_0. A detector measures the temperature rise at the rear face which is a function of time. Thermal diffusivity of the sample is obtained by analyzing the dynamic response of the rear face temperature rise. 98

Figure 5-4 Temperature change curves under different conditions measured on the rear side of the specimen. If there is no heat loss, the temperature on the rear face will rise to maximum and keep that value indefinitely (Curve A). However, with the heat loss involved, the temperature of the rear face decreases to varying extents after reaching a maximal value (Curves B and C). 99

المنارة للاستشارات
www.manaraa.com

Figure 5-5 Schematic of steady state method setup, where an electric power provides heat from the top of the setup, and an oil bath at the bottom functions as the cooling system, thus generating a steady temperature gradient. Four thermocouples are used to detect the temperature located at certain places of the copper rods, and an insulator box is added to reduce the heat loss during the measurements. 100

Figure 5-6 1D sectional perspectives of steady state measurement with a sandwich TIM where the possible resistances at the interfaces A and H will not be included into the calculated thermal resistance. Resistances at interfaces B, C, E and F can be offset after a series of sample measurements while the resistances at the interfaces D and E will be measured as the interface contact resistance between the substrates and the TIM layer. 101

Figure 5-7 The furnace assembly (a) of the flash diffusivity method and parts of it: the liquid nitrogen cryogenic detector (b), the specimen holder (c) and the furnace seal window (d). The specimen holder is located inside of the furnace and the seal window is placed onto the holder, with the detector on top. 102

Figure 5-8 The thermal resistance as a function of the thickness of the TIMs for 3 μm CuMPs: AgNFs = 6:4 by weight as prepared (the red triangle symbols), and of TIMs for 3 μm CuMPs: AgNFs: AgNPs= 6:2:2, with 2 % P4VP by weight (the blue dot symbols). The symbols are experimental data and both lines through the symbols are the best linear fitting. After plotting, the intercept is the contact resistance value of the two interfaces with two same substrates, while the reciprocal of the slope is the k. The result is summarized in table 5-1. 103

Figure 5-9 The volume fraction of fillers and voids with the change of packing density of TIMs. In the figure, both lines through the symbols are the best linear fitting. With the increasing packing density of the TIMs, the filler volume fraction increases as the void volume fraction decreases. 104

Figure 5-10 The k vs. void volume fraction of the TIMs. The lower the viodage, the higher the k. The k increases with increasing packing density. The line through the symbols is the best fitting of power-law with the exponent of -1.5, indicating rather complicated correlations between k and the void volume fraction. 105

Figure 5-11 Comparison of three analytical models and experimental data, where the symbols are experimental data from this study and curves are model predictions. Three models have similar prediction for low volume filling, i.e., at $v_f < 0.2$, above which their differences become prominent. BSM overestimates the k while both M-G model and BAM models underestimate the effective k of the TIMs, even assuming $\alpha = 0$ ($R_b = 0$). The cyan shadow centered at the dotted red curve is modified BSM calculation yielding an effective overall bulk k_f ~100-220 W/mK for the best match with the experimental data. 106

المنارة للاستشارات
www.manaraa.com

Chapter 1 Introduction

1.1 Current thermal interface materials (TIMs)

According to Moore's law [1, 2], the power densities in electronic devices have successfully doubled every two years in the microelectronics field, which was highlighted as early as 1965. Because of the nonuniform power distribution, the power density can reach as high as 300+ W/cm^2 at some hot spots on die [3], the temperature of which can be 10~40 ^{o}C hotter than the other parts of the chip [4]. As the trend of high degree integration and reduction in device dimensions continues, heat management has become more critical and fundamental to make the high-performance devices operate within their specifications. The TIMs has been widely used in the computing, LED lighting, photovoltaic and laser markets, and the market of TIMs had reached $1.3 billion until 2015 according to the report from IDTechEx Research [5]. TIMs with higher thermal performances are badly in need on current industrial market.

In the practical cases, only 1 to 2 % of the apparent area is in actual physical contact due to roughness of two joint solid surfaces, which is illustrated in figure 1-1 [6, 7]. This means that more than 97 % of the joint surface consists of air, which is a very poor thermal conductor (the k of air is 0.026 W/mK at room temperature) and works as a thermal barrier by preventing most heat transfer across the interface. TIMs are introduced to fill the air gap and increase the actual contact area between the central processor unit (CPU) and the heat

المنارة للاستشارات
www.manaraa.com

sink, thus minimizing the thermal resistance [7]. As shown in figure 1-2 [8], TIMs can be commonly used in the electronic packaging system, enabling effective heat removal from the chip to ensure its performance and reliability. In the image, TIM1 is the TIM to bond a chip with the heat spreader, and TIM2 is the TIM between the heat spreader and the heat sink, which indicates the widely-studied polymer-based TIMs. In order to enable efficient thermal conductance, it is necessary to use TIM1 with high *k*, which is why 100 % metal, namely solder, is usually used [9].

Currently, there have been developed various types of TIMs for different applications and demands of the markets, such as thermal greases, thermal pads, thermal gels, thermal tapes, phase change materials (PCMs) [6, 10-14], etc. Thermal grease was the first used as a TIM in spacecraft manufacture [15], which is typically a silicone or hydrocarbon oil based matrix loaded with ceramic particles to enhance *k* [16, 17]. Greases usually have high k, no curing requirement and not easy to delaminate, but because of their flow property, the thickness is difficult to control and excess greases can contaminate the other components. What's more, the thermal grease will easily dry out over time if used at higher temperatures because of the coefficient of thermal expansion mismatch between the thermal grease and the chips, resulting in low stability and poor reliability with thermal cycling. Chiu [18] reported that the thermal performance of a typical thermal grease can degrade more than 50 % after 2000 cycles because of the grease pump-out. Thus, the maket share of thermal greases has been experiencing decrease.

Thermal pads then began to merge, which are fabricated molding silicone with conductive fillers, reinforced by including woven glasses, metal foils and polymer films. Silicone provides high temperature stability while the reinforced materials provide cut-

المنارة للاستشارات
www.manaraa.com

through resistance. The thermal pads are expected to hold the largest market share by 2025 [5], for they are cleaner, easier to use and more precise. However, the thermal pads are sensitive to pressure and have lower *k* compared to thermal greases.

The thermal gels have a similar composition as thermal greases, silicone-based formulations loaded with thermally conductive fillers and cross-linked to form a low-modulus paste [12]. They are an ideal choice to fill variable gaps between multiple components and a common heat dissipating surface. The soft cross-linking binders with low modulus provide conformability at the interface at low pressure due to large tolerance. Compared to thermal greases, thermal gels don't have migration problem, but have lower *k* and need a curing process. Delamination is also a concern as to the long-term use.

Thermal tapes are acrylic or silicone based pressure sensitive adhesives loaded with conductive filler particles. They can bond a heat dissipating component to the heat sink without any additional pressure. The acrylic-based tapes are designed for metal or ceramic components, while silicone-based tapes used for plastic materials. This kind of thermal tapes require a certain degree of surface flatness. What's more, the thermal tapes have limited thermal performance and can loosen over time.

Phase change materials (PCMs) are a mixture of a base materials and suspended particles of high *k*, such as low-melting-temperature alloys (LMTAs), shape memory alloys, exfoliated clay and fusible/ non-fusible fillers, which are used in TIMs for generating very large latent heat during liquid-solid phase transaction at a certain temperature [19]. The base material, such as paraffin, polymers, or their mixture, is solid at low temperatures, but behaves much like grease after getting the "phase-change" temperature. PCMs have no migration problem due to higher viscosity, and easier to handle comparing to greases, but

المنارة للاستشارات
www.manaraa.com

still have limited k, and require pressure to maintain thermal performance. Stern's work [20] experimentally showed that the grease has superior thermal performance comparing to the PCMs at the bond line thickness of 50~100 μm.

The TIMs referred to above are all traditional polymeric TIMs, and account for more than 85 % of the current market share. Among them, the thermal greases normally have relatively better thermal performance. Arctic Silver thermal grease with suspended silver conductive fillers is the best with the k of 7.5 W/mK and thermal interface contact resistance (R_{int}) of 0.018 Kcm^2/W under a pressure of 12 psi. The next highest performing thermal grease is ShinEtsu G751, providing the k of 4.5 W/mK, and the R_{int} of 0.101 Kcm^2/W. The highest performance PCM is Thermax HF-60110-BT having the k of 20 W/mK, and the R_{int} of 0.0045 Kcm^2/W under 3~100 psi. However, the Thermax TIM significantly degraded and easily failed in the thermal cycling tests [7]. The highest performance PCMs reported are Power Strate 60 (AG) and 51 (AF), and they have been measured with similar thermal properties with the k of 3 W/mK, and the R_{int} of 0.142 Kcm^2/W under 10 psi pressure.

The cost of these commercial TIMs varies from the most expensive to the least: Arctic Silver > Thermax TIM > ShinEtsu G751, Power Strate 60 (AG) and 51 (AF) [21]. The thermal grease ShinEtsu G751 has better performance while with lower cost relatively, and it has been used in this study as the instrument TIMs during the steady state thermal measurement.

In addition to the traditional polymer-based TIMs, there are also a wide range of metallic solder TIMs developed. Lead (Pb)-free solders have been studied as a high-end TIM to replace the traditional Sn-Pb solders with a low melting point, good material

المنارة للاستشارات
www.manaraa.com

property and low cost, but toxic [22-24]. Recently, Indium Corporation has developed several types of solders, such as pure indium (In), In/Pb solder, Sn-Ag-Cu (SAC) Pb-free solder, Au/Sn solder, etc. The *k* of In-based intermetallic solders can be up to 86 W/mK [25], and that of Zn-Sn alloys exceeds 100 W/mK [26, 27]. However, lots of concerns regarding such solder TIMs lead to a fact that they have limited use for first level power-die-attach where there are no other viable substitutes [9]. In addition to conducting electricity, solder joints provide good mechanical support for electronic devices. The solder TIMs can handle stress well, wet both metallic and non-metallic surfaces, and are good to use between the chips and heat sink with mismatched coefficient of thermal expansion (CTE). The mechanical properties of solder alloys are critically important in producing reliable products. However, the high compliance of In can lead to structural collapse following the attachment of a heat sink [28, 29], or large-volume expansion [22, 26]. Many attempts has been made to improve this situation by developing liquid phase sintering (LPS) solder with addition of high melting phase (HMP), such as Sn, Cu, and Au, together with the low melting phase (LMP) [30].

Besides the above concerns and high cost of solder TIMs, there are some other challenges, e.g., wettability of materials [23], metal oxidization [7], stability during the heat reflow and metallurgical reliability upon thermal cycling [28], for the intermetallic formation and microstructure evolution brings either electromigration or creep [31-33], resulting in degradation of solder strength [24, 29]. Voids formation during manufacturing is another major concern for solder TIMs, resulting in local thermal conductance deterioration and TIM failure [34, 35]. Voids may grow upon thermal cycling and thermal

المنارة للاستشارات
www.manaraa.com

stressing, which further attenuates heat conduction and reduces the reliability of the electronic packaging [36, 37].

New advanced TIMs with nanostructures have generated an increasing interest, such as TIMs involving carbon fibers, carbon nanotubes [38-40] and graphene [41-44]. It is reported that the theoretical k of individual multiwalled carbon nanotube (MWCNT) in the axial direction can be as high as 3000 W/mK, and that of graphene can reach 5000 W/mK or higher depending on different thermal methods [42, 45]. However, the discrete distribution nature of MWCNTs in TIMs results in much lower overall k to 15 W/mK or lower [39], due to the uncontrollable distribution of the MWCNTs or the boundary resistance existence at the interface of the CNTs and a polymer matrix [46]. Although massive research work has been done, it is believed that the nanocarbon-based TIMs are still far away from real application, and the reliability and performance degradation of the carbon-based TIMs still needs more study. The other nanostructured TIMs are those involving metallic nanoparticles as fillers or nano-structuring a bulk ceramic or metal foam. Studies have shown that doping micro-to-nano sized metallic or ceramic particles in the second phase elements can improve mechanical reliability as well as refine the interfacial microstructure of the solder alloys [23, 32, 33, 47, 48].

In summary, there are various challenges for next-generation TIMs [49, 50] that is an important necessity in the industry because of the higher frequency operation and increasing powder density of electrical devices. The ideal TIM would have the following characteristics: high thermal conductivity, good mechanical properties, no leakage from the interface, long-term stability, wide operating temperature range, non-toxic, low cost and easy to apply/remove. However, there are tradeoffs among these factors in different

المنارة للاستشارات
www.manaraa.com

situations. The materials' development and the thermal measurement methods are the main technical barriers existing [51]. Modification on the materials at micro-to-nano scale appears to be the way to improve performances.

1.2 Key properties of TIMs

There are many factors governing the performance of a TIM, including the structure of the joint surfaces, the applied pressure, the thickness of the TIM, and the properties of the TIM itself. There are various properties of a TIM to be considered, such as the thermal properties (k and thermal interface contact resistance R), mechanical properties (viscosity, elastic modulus and conformability) and reliability (thermo-mechanical and performance degradation) [6, 52, 53].

1.2.1 Mechanical properties

Although low thermal impedance is an important property of a TIM, the TIM also needs to have good mechanical performance when coming to its assembling and applications. A low modulus and a low viscosity helps the TIMs with better spreadability and conformability, the ability to flow macroscopically, but also to fill microscopic valleys (even those on the nanoscale) at the joint surfaces [52]. To enhance the filling of microscopic valleys, a microscopically structured (preferably nanostructured) interface material is desirable, such as the CNT thermal paste [42, 54]. These nanostructured additives are used to improve not only the k but also the mechanical performance and the reliability of the materials [46, 55]. A higher filler volume fraction helps increase the k; on the other hand, it also increases the viscosity of the mixture, but makes it more difficult to

المنارة للاستشارات
www.manaraa.com

disperse. As for the modulus of the TIMs, greater pressure is required for the TIM with a higher modulus. However, the provided pressure is limited in practical microelectronic applications. Therefore, there is a tradeoff on the filler percentage between the modulus and the viscosity of the TIMs.

The mechanical properties can be used to classify materials and help determine the range of usefulness of a material and expected service life. Typical mechanical properties [56, 57] of a material are as follows.

- Strength: the ability to oppose deformation or breakdown upon external force.
- Ductility: the ability to become deformed under tensile stress by pulling or drawing before breaking.
- Brittleness: the ability to get fractured when subjected to an external force or load, which is opposite of ductility of materials. Both ductility and brittleness are temperature dependent.
- Creep: the tendency of materials to move slowly and deform permanently under the influence of a long-time external stress loading, which is also temperature dependent.
- Hardness: the ability to resist permanent shape change due to external force, which reflects the plastic deformation properties of materials, including scratch hardness, indentation hardness and rebound hardness.
- Resilience: the ability to absorb energy when deformed elastically by applying a force and release energy when removing the force, which is determined by stress-strain curves from zero to elastic limit.

المنارة للاستشارات
www.manaraa.com

- Toughness: the ability to absorb energy and get plastically deformed without fracturing, which is also determined by stress-strain characteristics. Materials with good toughness should have good strength and ductility.

- Fatigue: the weakening and fracture of materials resulting from the repeated loading.

These mechanical properties often change with different temperatures, rates of loading, in addition to other conditions. For example, decreasing temperatures generally lead to an increase in strength and brittleness of the materials, while ductility, creep and toughness usually decrease. Singhal [58] observed that when loading successive stress cycles on the TIM, the thermal contact conductance increased upon the first several cycles, and later came to a steady value.

One thing should be noted is that there is often significant variability in the acquired data when measuring mechanical properties. Identical tests for the samples with same material often generate considerably different results. Therefore, it is necessary to carry out multiple tests and report the average value or calculated statistical minimum value to determine mechanical properties. A range of values are sometimes reported in order to show variability.

1.2.2 Reliability properties

Reliability engineering is a popular concept used for decades in academics and industry. It has been extensively used in the title or as keywords in the general public and technical community, e.g., the web of science lists ten thousand technical articles with the keyword of reliability, and over 12 million occurrences have been accumulated on Google website from 1973 to 2006 [59]. Reliability indicates the probability of an item to perform

المنارة للاستشارات
www.manaraa.com

a required function under given conditions over a specific period of time [60, 61]. Generally, electronic devices are typically designed to last for 7-10 years, whereas avionics and telecommunication devices are expected to survive for decades [10]. The purpose of reliability study of the material is to prevent or reduce the frequency of its failures, by identifying and correcting the causes of failure.

Currently, well-established reliability engineering aims at studying the uncertainty in the failure occurrences and consequences in quantitative approaches. Through launching failure data collection and root cause analyses, the goals are to figure out why the systems fail, how to develop reliable systems, how to measure and test reliability in design, operation and management, and how to maintain reliable systems [62]. Reliability behavior of materials is usually characterized by accelerated aging tests [53, 63-65], which is to induce the failure at a much faster rate by providing harsher conditions, such as relatively high or low temperature storages, severe and long-term temperature cycling, and humidity storage. The accelerated tests can help to discover the failure mode of the system with much less time, and at the same time to predict the normal field life, which is commonly used in the laboratory.

Reliability is always one of the most important considerations in determining the value of a TIM, and is required in maintaining its thermal resistance consistently over use for an extended period of time. Low quality or inappropriate TIMs will degrade with time causing the increasing of thermal resistance at the interface, as well as the temperature at joints of the electronic device, leading to component failure [66]. There are 3 common stress test categories for TIMs, the accelerated temperature and humidity stress test (THT & HAST) [67-69], high temperature storage test (HTS) [70-72], and temperature cycling

www.manaraa.com

stress test (TC) [67, 73-75]. The thermo-gravimetric analysis (TGA) and differential scanning calorimetry (DSC) are also used during stability test of TIMs at the elevated temperatures to investigate the weight loss and the possible transition characteristics of the material. Visual observation, e.g., scanning acoustic microscopy (SAM) [76, 77] is used to detect the structural changes of the TIM layer, such as voiding, cracking and delamination, from which most TIM failures result.

To carry out the general reliability tests, samples are tested after a predetermined time under elevated temperatures or humidity, or number of cycles, under stress and simple before-and-after comparisons are made [78]. In some other cases, the samples are measured intermittently in order to trace the rate of degradation with time or cycles [53, 70, 75]. In a very few studies, the degradation trends are analyzed and corresponding statistical models are created to represent the changing performance over time [79]. The representation and modeling of the system and the quantification of the model in reliability engineering are still challenging tasks due to the complexity of systems [62]. For example, Arrhenius-type relationship was applied in the HTS testing, which is temperature activated degradation [35]. Thermo-mechanical stresses are the most commonly reliability characterizations upon temperature cycling [68, 80-82], especially when the components within the TIMs or the devices, which have different coefficients of thermal expansion (CTEs) and their stress changes at varying operation temperatures. Delamination may be generated over time or thermal cycling, affecting interface contact resistance and leading to overheating and device failure.

The general degradation mechanisms of TIMs are mainly microstructural and compositional changes (such as metal oxidation [83]), time-dependent deformation and

المنارة للاستشارات
www.manaraa.com

damage accumulation (such as delamination [83, 84]), environmental attack (such as hydrothermal effects [72]), the accelerating effects of elevated temperature [83, 85], or synergistic effects among the above [86]. Generally, strength, stiffness, and thermal properties as well as failure modes are affected by the mechanical and chemical degradation of composites of TIMs. Stiffness, strength, and coefficient of thermal expansion decrease with increasing microcrack density. Exposure to high temperatures can cause chemical degradation of composite-matrix polymers [87]. Hydrothermal effects can lead to significant residual stresses, TIM layer delamination, or blistering during rapid heating, where the absorbed moisture can increase the residual stresses leading to matrix cracking, and microcracking can accelerate moisture absorption and desorption [83].

1.2.3 Thermal properties

When purchasing a TIM, the commonly available property of the material provided by the manufacturer is the k, which is the most direct way to evaluate TIMs. During conduction of heat through a material, the heat rate is proportional to the heat flux, interface area and the temperature gradient along the heat flow path. For a one-dimensional, steady state heat flow, the heat rate can be expressed by Fourier's equation [88].

$$Q = kA\frac{\Delta T}{d} \tag{1-1}$$

Where Q is the rate of heat flow (W), k is the thermal conductivity (W/mK), A is the contact area (m^2), ΔT is the temperature difference of the material, d is the distance of heat flux (m). The thermal conductivity, k, is a natural property of a material which demonstrates the material's heat conduction ability. Another intrinsic thermal property of materials is the thermal resistance, R, which can be presented in equation 1-2.

المنارة للاستشارات
www.manaraa.com

$$R = A\frac{\Delta T}{Q} \quad (1\text{-}2)$$

The relationship between thermal conductivity k and thermal resistance R is shown in equation 1-3, which is mostly used for the homogeneous materials.

$$k = \frac{d}{R} \quad (1\text{-}3)$$

For non-homogeneous materials, the thermal resistance is not directly proportional to the thickness, which is known since Kurti [89] first discovered a temperature jump at the liquid helium and copper interface in 1936, and Kapitza [90] measured the thermal resistance at the solid-liquid helium interface in 1941. Prasher [91] was the first to propose the separation of the bulk resistance and the contact resistance, and gave the physical model of TIM as shown in figure 1-3. The interface thermal resistance is actually consist of three portions after adding TIMs at the two joints, which can be expressed as follows.

$$R_{\mathrm{TIM}} = R_{\mathrm{bulk}} + R_{\mathrm{c1}} + R_{\mathrm{c2}} = \frac{\mathrm{BLT}}{k_{\mathrm{TIM}}} + R_{\mathrm{c1}} + R_{\mathrm{c2}} \quad (1\text{-}4)$$

$$R_{\mathrm{bulk}} = \frac{\mathrm{BLT}}{k_{\mathrm{TIM}}} \quad (1\text{-}4a)$$

In the above equations, R_{c1} and R_{c2} are two thermal contact resistances at the two interfaces between the TIMs and the heat sink, and between TIMs and the heat spreader (m^2K/W), BLT is the bond line thickness (m), k_{TIM} is the thermal conductivity of the TIMs (W/mK). To achieve highly efficient heat conduction, a TIM needs to have low BLT, high k and low thermal contact resistances. The key thermal properties of TIMs are thermal conductivity and contact resistance, which have been commonly used to evaluate the thermal performance of TIMs.

المنارة للاستشارات
www.manaraa.com

A low BLT is necessary to achieve a high thermal conduction, so it is often targeted in commercial application. This is easier to realize for TIMs with low viscosity. For TIMs with high viscosity, such as thermal pads, pressure is often applied to get low BLT. However, a high BLT can provide better strain relief when there is an external clamping stress. A high BLT can also improve the reliability upon thermal cycling [92], since the high BLT can help to prevent the delamination generated by the coefficient of thermal expansion (CTE) mismatch between the heat sink and heat spreader. Therefore, the BLT is a tradeoff factor for the TIM application.

High bulk k is an intrinsic property of the TIMs, which depends on the material design and manufacture. Even for the non-homogeneous TIMs, k just depends on the composition of the materials, such as the type of materials, and the size and shape of the particles.

Low contact resistance can be brought out when the TIM has good wettability in relation to the surfaces of the heat sink and heat spreader, e.g., TIM with low viscosity has better wetting ability. Except for the material itself, there are several extrinsic factors which affect the contact resistance, such as surface flatness and roughness, surface micro-hardness, loaded pressure etc. [58, 93], which can be seen from the following expression of the solid-solid contact resistance R_c between two surfaces assuming plastic deformation of the asperities [94].

$$R_c = \frac{0.8\,\sigma}{m k_h}\left(\frac{H}{P}\right)^{0.95} \quad (1\text{-}5)$$

$$\sigma = (\sigma_1^2 + \sigma_1^2)^{0.5} \quad (1\text{-}5a)$$

$$m = (m_1^2 + m_1^2)^{0.5} \quad (1\text{-}5b)$$

www.manaraa.com

$$k_{\mathrm{h}} = \frac{2\mathrm{k_1 k_2}}{\mathrm{k_1 + k_2}} \quad (1\text{-}5c)$$

Where σ is the root mean square roughness of the two surfaces, m is the root mean square asperity slope, k_h is the harmonic mean thermal conductivity of the two surface materials, H is the micro-hardness of the softer material, P is the applied pressure. Stern [20] studied the effects of the surface characteristics on the thermal contact resistance, and Bharatham [95] studied the influence of applied pressure. Singhal [58] showed that the thermal contact conductance decreased to only 7 % as the nominal surface roughness increased from 1 μm to 15 μm at the same interface pressure. A coating premier used to bond the TIMs with the surfaces of the heat sink and the heat spreader is a good method to improve the roughness and asperity, further decrease the contact resistance, as well as enhance the wettability and adhesion of the materials [92].

1.3 Thermal conductivity measurements

There are a number of techniques to measure thermal conductivity of TIMs, and each of them has limited requirements for the materials. Generally, they can be divided into two basic categories of techniques, steady state and transient (non-steady state) method [96]. The steady state methods, such as the guarded heat flow method and the guarded comparative longitudinal heat flow method, are based on one-dimensional Fourier's equation [88], in which a constant heat flow is applied on the both sides of the TIM sample to establish thermal equilibrium, a temperature difference that does not change over time. ASTM D5470 [92, 97] is the theoretical basis for most commonly used steady state method to measure the *k*, and the *k* of the TIM can be calculated as below.

المنارة للاستشارات
www.manaraa.com

$$k = \frac{Q\,d}{A\,\Delta T} \quad (1\text{-}6)$$

$$Q = P - Q_{loss} \quad (1\text{-}7)$$

Where Q is the amount of heat flux through the sample, d is the thickness of the sample, A is the surface area of heat flux through the sample, ΔT is the temperature difference between the two surfaces of the sample, P is the applied heating power provided by the heat source, Q_{loss} is the heat loss due to radiation, conduction, and convection to the environment. One of the major challenge of the steady state method is to determine the real heat flux Q, and we usually use P instead of Q for calculation, during which we assume that the heat loss less than 2 % of the total heat power P. In this case, some methods have been done to minimize the heat loss, such as conducting the measurement under vacuum to decrease the gas reduction loss, using radiation shields that either match the temperature gradient of the sample or reflect the heat back on the sample [98] to reduce the radiation heat loss. Thermocouples with small wire diameter (0.001 inch) and low thermal conductance are used to reduce the convective heat loss [99]. What's more, some TIMs are used to avoid bare contact between the conduction rod and the measured TIM and reduce the contact resistance, such as thermal grease, thermal pads and pressurized gases [100].

Much research work has been done to correct these assumptions and improve the accuracy of the steady state method [101-103], achieving less than 5 % error on the commercial *k* measurement testers [104]. The steady state method is also used to measure the thermal contact resistance between the TIMs and the two substrates. Major disadvantages of the steady state method are that the specimen should be relatively large and have a better fit with the shape of the conduction rods, and the test requires a period of time (several hours) to realize the temperature equilibrium.

المنارة للاستشارات
www.manaraa.com

Transient methods, such as flash diffusivity method [105, 106] and 3ω method [107], have been developed to overcome the drawbacks associated with the steady state method, e.g., the parasitic heat loss and long waiting time to establish the thermal equilibrium. Flash diffusivity method [108-110] is the most popular transient tool to measure the *k* of solids. It was first described by W. J. Parker [105] in 1960s for the ideal case, during which the sample is isotropic and there is no heat loss. The advantage of this method is that it can generate values very quickly and efficiently, since the actual measurement can only take a few seconds. There are not so many requirements on the specimen of its composition, size and thickness with a wide range of experimental conditions, such as the temperature. What's more, the data obtained has good accuracy (reported uncertainty is 2~3 % for thermal diffusivity, and 5 % for *k* [111]) and repeatability. Some disadvantages of the non-steady state method are that more complicated mathematic analyses need to be involved in the transient techniques, and this method ignores the thermal contact resistances at the interface of the sandwich sample.

Parker is the first to derive the mathematical expression for thermal diffusivity calculation, beginning with the temperature distribution on the rear face of the specimen at a certain time, which is given by Carslaw and Jaeger [112].

$$T(x,t) = \frac{1}{L}\int_0^L T(x,0)\,dx + \frac{2}{L}\sum_{n=1}^{\infty} \exp\left(\frac{-n^2\pi^2}{L^2}\alpha t\right) * \cos\frac{n\pi x}{L}\int_0^L T(x,0)\cos\frac{n\pi x}{L}\,dx \qquad (1\text{-}8)$$

Where T is the temperature (K), x is the length (m), t is the time (s), L is the specimen thickness (m), α is the thermal diffusivity (m^2/s).

Assume the heat of the pulse is Q, and it is uniformly and fully absorbed by a small depth g at the front surface x= 0, the initial conditions can be given as below.

المنارة للاستشارات
www.manaraa.com

$$T(x,0) = \frac{Q}{g\rho C_p}, \text{ for } 0 < x < g \quad (1\text{-}9)$$

$$T(x,0) = 0, \text{ for } g < x < L \quad (1\text{-}10)$$

Where ρ is the density of the material (kg/m^3), C_p is the specific heat capacity (J/g K). Taking the above initial conditions into the equation 1-8, the temperature distribution becomes:

$$T(x,t) = \frac{Q}{L\rho C_p}[1 + 2\sum_{n=1}^{\infty} \cos\frac{n\pi x}{L} \frac{\sin\frac{n\pi g}{L}}{\frac{n\pi g}{L}} \exp\left(\frac{-n^2\pi^2}{L^2}\alpha t\right)] \quad (1\text{-}11)$$

Since g is very small, $\sin\frac{n\pi g}{L} \approx \frac{n\pi g}{L}$, the temperature at the rear face x= L is:

$$T(L,t) = \frac{Q}{L\rho C_p}[1 + 2\sum_{n=1}^{\infty} (-1)^n \exp\left(\frac{-n^2\pi^2}{L^2}\alpha t\right)] \quad (1\text{-}12)$$

Two dimensionless parameters are introduced, V and ω.

$$V(L,t) = \frac{T(L,t)}{T_M} \quad (1\text{-}13)$$

$$\omega = \frac{\pi^2}{L^2}\alpha t \quad (1\text{-}14)$$

Where T_M is the maximum temperature at the rear face. Combing equation 1-12, 1-13, 1-14, we get:

$$V = 1 + 2\sum_{n=1}^{\infty} (-1)^n \exp(-n^2\omega) \quad (1\text{-}15)$$

In the above equation, when V= 0.5, ω= 0.138, therefore we have:

$$\alpha = 1.38\frac{L^2}{\pi^2 t_{1/2}} = 0.1388\frac{L^2}{t_{1/2}} \quad (1\text{-}16)$$

Here $t_{1/2}$ is the time spent for the rear surface to reach half of the maximum temperature. The above ideal model was deduced based on several assumptions [108], and they are given below.

المنارة للاستشارات
www.manaraa.com

(1) The specimen material is homogeneous and isotropic, and their thermo-physical properties and density are uniform and will not change with temperature during the measurement.

(2) The pulse is instant, or its duration is infinitesimally small in comparison to the thermal response of the slab.

(3) The pulse is absorbed by the front surface uniformly, and by a very thin layer compared to the thickness of the specimen.

(4) The heat flow is one dimensional.

(5) There is no heat loss from the surfaces of the specimen.

The precision of the method mostly depends on how the experimental conditions meet the above assumptions. Upon evaluating the practical experiments, the Parker model showed obvious inadequacy, for the above conditions are all hypotheses in order to simplify the model and almost all of them are violated to some extent. Gradually, various corrections were proposed to counter the violation of the boundary conditions. However, each correction model can only focus on one or two factors based on the ideal model. Until now, no one correction has been formulated to encompass all the factors. Therefore, a most proper correction needs to be chosen under the certain experimental conditions. For example, when thin samples of high k are under testing, the finite pulse width effect becomes stronger [113-116], while the radiative heat loss is dominant at high temperature for thin samples [117, 118].

Cowan [119] was the first to incorporate radiative heat loss from the specimen surfaces into the mathematic mode, with the assumption that the pulse is much shorter than the "half-max-time" $t_{1/2}$. Under the observation of the steady decrease of the temperature

www.manaraa.com

after the peak temperature, he determined the ratio parameter between the temperature change of $t_{1/2}$ and a new temperature parameter. Clark and Taylor [117, 120, 121] also studied the radiative heat loss factor with the same assumption as Cowan made, but by different methods to get the ratio parameter. They focused on the temperature vs. time plotting for the same sample before reaching the peak temperature at the rear surface.

Heckman [122, 123] was one to propose the correction model including the effect of the pulse width for the condition that the pulse time was not much shorter than the "half-max-time". He determined a new temperature vs. time shape after analyzing a triangular wave form, and adjusted the time parameters according to the finite pulse width, which would affect the result of both Cowan and Clark and Taylor. Koski [124] improved Heckman's correction and included all the previous corrections by combining the laser pulse width with the radiative heat loss corrections built by both Cowan and Clark and Taylor.

A comparison of the measurement time and sample size of different *k* measurement methods has been carried out [21], including the steady state thermal measurement and flash diffusivity method described above. The absolute technique and comparative technique, such as the steady state method, can measure large-size samples, but needs a longer time for data acquisition, while the transient technique, including the flash diffusivity method, is capable of measuring a thinner film sample in a much quicker way. Generally, it is a challenging task to determine the *k* and interface contact resistance of a TIM with less than 5 % error, and it is also not easy to decide which is the best thermal measurement technique. However, there are some useful notes for references.

المنارة للاستشارات
www.manaraa.com

(1) knowledge of the thermo-physical properties of the specimen to be measured, including the sample size, geometry, and surface roughness.

(2) understanding of the fundamentals and procedures of the testing technique and equipment, e.g., some techniques are limited to samples with specific sizes.

(3) clarifying of the potential error sources which might affect the final results, such as the convection and radiation heat losses in steady state method, the uncertainties from density and specific heat measurement introduced into the flash diffusivity method.

1.4 Theoretical effective thermal conductivity models

As discussed earlier, eliminating the air voids between the two joint surfaces is the main pathway to improve the heat transfer, which is also the purpose for introducing TIMs. However, the voids can be also generated within the TIM system, and affect the thermal, mechanical and reliability performance of the TIMs [11, 125], for R. K. McGeary presented that the voidage in a multi-particle system for closest packing is 0.14 [126]. The *k* depending on the void volume fraction (or packing density) has been studied on many types of TIMs [6, 127-131], and numerous prediction models have been developed based on this relationship, such as Maxwell [132], Maxwell-Garnett [133], Rayleigh [134], Bruggeman [135, 136], Lewis-Nielsen [137], percolation [138, 139] models etc.

For heterogeneous materials, their effective *k* is determined by the relative amount of the components, where the "effective" is used to denote that the heterogeneous material has a single *k* as assumed to be homogeneous on a macroscopic scale. Thus, we defined

المنارة للاستشارات
www.manaraa.com

the volume fraction of the fillers and voidage [140], which are closely related to the packing density.

$$\text{Volume fraction of fillers} = \frac{\text{volume of fillers within material}}{\text{total volume of material}} \quad (1\text{-}17)$$

$$\text{Voidage} = \frac{\text{volume of void space within material}}{\text{total volume of material}} \quad (1\text{-}18)$$

$$\text{Packing density} = \frac{\text{total weight of material}}{\text{total volume of material}} \quad (1\text{-}19)$$

Fillers mean the metal particles with high k to enhance the thermal performance of the TIMs, which are also called the “dispersed phase”, corresponding to the “continuous phase” (matrix).

The Series and Parallel models are the two simplest k models. As their names suggest, the Series model supposes that the heat goes through all the components of the material in series, while the Parallel model assumes that the heat flows through the material components in parallel, which is by analogy to the total resistance calculation in an electrical circuit by Ohm’s law. Though they are simplest, they can provide the possible theoretical bounds for the effective k value of a material if the k and volume fraction of the components are given [141, 142]. Lichtenecker [143] proposed the geometric model as a simple intermediate to the Series and Parallel models, as indicated.

Series model:

$$\frac{1}{k_e} = \frac{1-\upsilon_f}{k_m} + \frac{\upsilon_f}{k_f} \quad (1\text{-}20)$$

Where k_e is the total effective thermal conductivity of the composites, k_m is the thermal conductivity of the matrix, k_f is the thermal conductivity of the fillers, v_f is the volume fraction of the fillers.

Parallel model:

www.manaraa.com

$$k_e = (1 - \upsilon_f)k_m + \upsilon_f k_f \quad (1\text{-}21)$$

Geometric model:

$$k_e = k_m{}^{(1-\upsilon_f)}\, k_f{}^{\upsilon_f} \quad (1\text{-}22)$$

Pioneering theoretical work on predicting effective k of heterogenic materials in macroscale was inspired by Maxwell [132] and Rayleigh [134]. Maxwell was the first to propose effective k analytical expressions for non-interacting homogeneous materials in his book on electricity and magnetism in 1987. The Maxwell model described the situation of dilute dispersion of spherical particles of k_f embedded in an infinite matrix of k_m, and the thermal interactions between particles were ignored. Many researchers extended Maxwell's model to other shapes of particles, such as ellipsoidal shapes by Fricke [144] and Burger [145], cylinder, disk and other shapes by Hamilton and Crosser [146], Nielsen [137, 147].

Maxwell model (for spherical fillers):

$$\frac{k_e}{k_m} = 1 + \frac{3\upsilon_f}{\left(\frac{k_f+2k_m}{k_f-k_m}\right) - \upsilon_f} = \frac{(k_f+2k_m)+2\upsilon_f(k_f-k_m)}{(k_f+2k_m)-\upsilon_f(k_f-k_m)} \quad (1\text{-}23)$$

Rayleigh [134] developed a model for system inclusions arranged periodically in a simple cubic array embedded in a continuous matrix, in which thermal interactions between the particles were taken into consideration. It gives better prediction for the materials with higher filler volume fractions than Maxwell model.

Rayleigh model (for spherical fillers) [148]:

$$\frac{k_e}{k_m} = 1 + \frac{3\upsilon_f}{\left(\frac{k_f+2k_m}{k_f-k_m}\right) - \upsilon_f + 1.569\left(\frac{k_f-k_m}{4k_f-3k_m}\right)\upsilon_f^{\frac{10}{3}} + \cdots} \quad (1\text{-}24)$$

When ignoring all the higher order components in the above equation, it reduces to the Maxwell model expression. Rayleigh also gave the analytical expression for the

المنارة للاستشارات
www.manaraa.com

effective k of another type of composite: fibers embedded in a continuous matrix besides the spherical particles.

Based on macroscopic Maxwell's model, Maxwell Garnet (M-G) developed a simple but successful homogenization theory in 1904 [133], which aimed to approximate a homogeneous effective medium for a complex medium such as a colloidal solution. M-G expression is given in equation (1-25).

$$\frac{k_e}{k_m} = \frac{[k_f(1+2\alpha)+2k_m]+2\upsilon_f[k_f(1-\alpha)-k_m]}{[k_f(1+2\alpha)+2k_m]-\upsilon_f[k_f(1-\alpha)-k_m]} \quad (1\text{-}25)$$

$$\alpha = \frac{2\alpha_k}{d} = \frac{2R_b k_m}{d} \quad (1\text{-}25a)$$

Where, α is the Biot number, a non-dimensional parameter, α_k is the effective Kapitza radius [149, 150], R_b is the thermal boundary resistance, d is the diameter of the filler particles. When the interface resistance is negligible, $\alpha = 0$, the equation 1-25 will reduce to original Maxwell model. If $\alpha = 1$, the actual size of the particles equals to the Kapitza radius, and the effective k of the fillers and that of the matrix is equivalent, which means that the particles don't help to reinforce the k. If $\alpha > 1$, the actual particle size is smaller than the Kapitza radius, and the thermal interface resistance becomes a dominant factor on the k of the composite. If $\alpha < 1$, the actual particle size is larger than the Kapitza radius, the fillers can enhance the k.

Hasselman and Johnson [151] extended the classical work of Maxwell and Rayleigh to calculate effective k of simple spherical particulate and cylindrical fiber reinforced matrix composites. Benvensite's [152] modification achieved the same result based on a micromechanics method, as shown in equation 1-25. The modified model

المنارة للاستشارات
www.manaraa.com

considered that the k depends not only on the volume fraction of the filler particles with a given shape, but also on the particle size and the interfaces.

It was proved that the Maxwell and Rayleigh models only could be valid for the effective k of materials with low v_f (< 25 %), and trended to underestimate the effective k of TIMs with higher concentration [153, 154]. As for the composite with higher filler volume fraction, Bruggeman [135, 136, 153] developed two effective media theories to predict the effective k in 1935, the symmetrical and the unsymmetrical effective medium theory.

Bruggeman symmetric model (BSM)/ effective medium theory (EMT):

$$(1-\upsilon_f)\frac{k_m-k_e}{k_m+2k_e}+\upsilon_2\frac{k_f-k_e}{k_f+2k_e}=0 \qquad (1\text{-}26)$$

The BSM theory doesn't make a distinction between the discontinuous fillers and continuous matrix and assumes that the pores and the matrix exist in a symmetric mixture, during which a composite material can be constructed by introducing infinitesimal changes upon continuous filling toward an already existing system. The BSM thus leads to differential equations, so it is also called differential effective medium theory (EMT), which was later modified by Landauer [136, 155].

Using Bruggeman's approach, Every and Tzou [149] refined the EMT, considered Kapitza resistance, and obtained an asymmetric Bruggeman expression for effective k of particulate composites by modifying Benveniste's result [152].

Bruggeman asymmetric model (BAM):

$$(1-\upsilon_f)^3=\left(\frac{k_m}{k_e}\right)^{(1+2\alpha)/(1-\alpha)} * \left[\frac{k_e-k_f(1-\alpha)}{k_m-k_f(1-\alpha)}\right]^{3/(1-\alpha)} \qquad (1\text{-}27)$$

This Bruggeman models are popular, because they cover a wide spectrum of materials, give a formula for multi-component systems in addition to the classical case of

www.manaraa.com

two components, and provide a more accurate result for composites with high volume fractions of discontinuous spherical inclusions. The BAM brings a new understanding of the influence of microstructure on the heat transport property.

If the TIMs can be divided into two types, "internal porosity" and "external porosity", the internal porosity materials are those which have bubbles suspended within a continuous matrix, while external porosity materials are those in which void spaces exist in the interstices of granular particulate materials [156]. Carson [142] proposed that the effective *k* of internal porosity materials is bounded above by the Maxwell equation and below by the EMT equation; while the effective *k* of external porosity materials is bounded above by the EMT equation, and below by the Maxwell equation.

Apart from the classical models above, there are also many other numerical methods to predict effective *k* in the case of a higher inclusion volume fraction, such as the percolation models [138, 157-159], dynamic methods [160, 161], the finite element methods (FEM), [162-166] etc. Though most of the mathematical analyses are good examples, the classical models are still used more often because of their simplicity.

1.5 Chapter flow

In this study, a novel resin-free TIM paste has been developed by introducing silver nanoparticles (AgNPs) and silve nanoflakes (AgNPs), exhibiting good thermal, mechanical and thermo-mechanical performances [167]. Figure 1-4 shows the comparison result of the thermal properties of this nanocomposite TIMs and various current TIMs, including the popular polymeric TIMs, such as thermal greases, thermal pads, phase change materials

المنارة للاستشارات
www.manaraa.com

(PCM), etc., and the high-performing solder TIM as discussed previously. The novel hybrid TIMs have demonstrated the *k* as high as the solders and their contact resistance can be lower than that of the best thermal greases.

In Chapter 2, the AgNPs two-phase synthesis is described and the morphology is characterized with SEM and TEM. The AgNPs' weight evolution upon heating is investigated using TGA, while their size transformation during the sintering process is studied using XRD and in-situ SAXS.

In Chapter 3, the preparation of TIM paste and sandwich TIM assemblies is presented. SEM and EDX studies the morphology of the sintered nanocomposite TIMs showing the continuous network bonded by fused Ag particles. The scanning acoustic microscope (SAM) images the voids in the TIM assemblies insitu, and XRD explores the possible phase transformation upon sintering.

In Chapter 4, different assembling conditions were compared according to the ultimate shear strength and relative energy density of the TIM samples using the shear and tensile tests, showing that the higher the sintering temperature and the longer the sintering duration time, the stronger and tougher the TIM assemblies produced. The thermo-mechanical performance study of hybrid TIM pastes focuses on the mismatched sample with invar and copper foils as two substrates, with a linear CTEs mismatch exceeding 15 ppm/^{o}C.

In Chapter 5, the effective *k* of the nanocomposite TIMs is measured with steady state and flash diffusivity methods, showing that the *k* of TIMs can be as high as 140 W/mK, and the contact resistance can be as low as $1.3*10^{-6}$ m^2K/W. The experimetal data is compared with several theoretical models to predict effective *k*.

المنارة للاستشارات
www.manaraa.com

In Chapter 6, conclusion and outlook is discussed, and necessary future work related to the research is proposed.

المنارة للاستشارات
www.manaraa.com

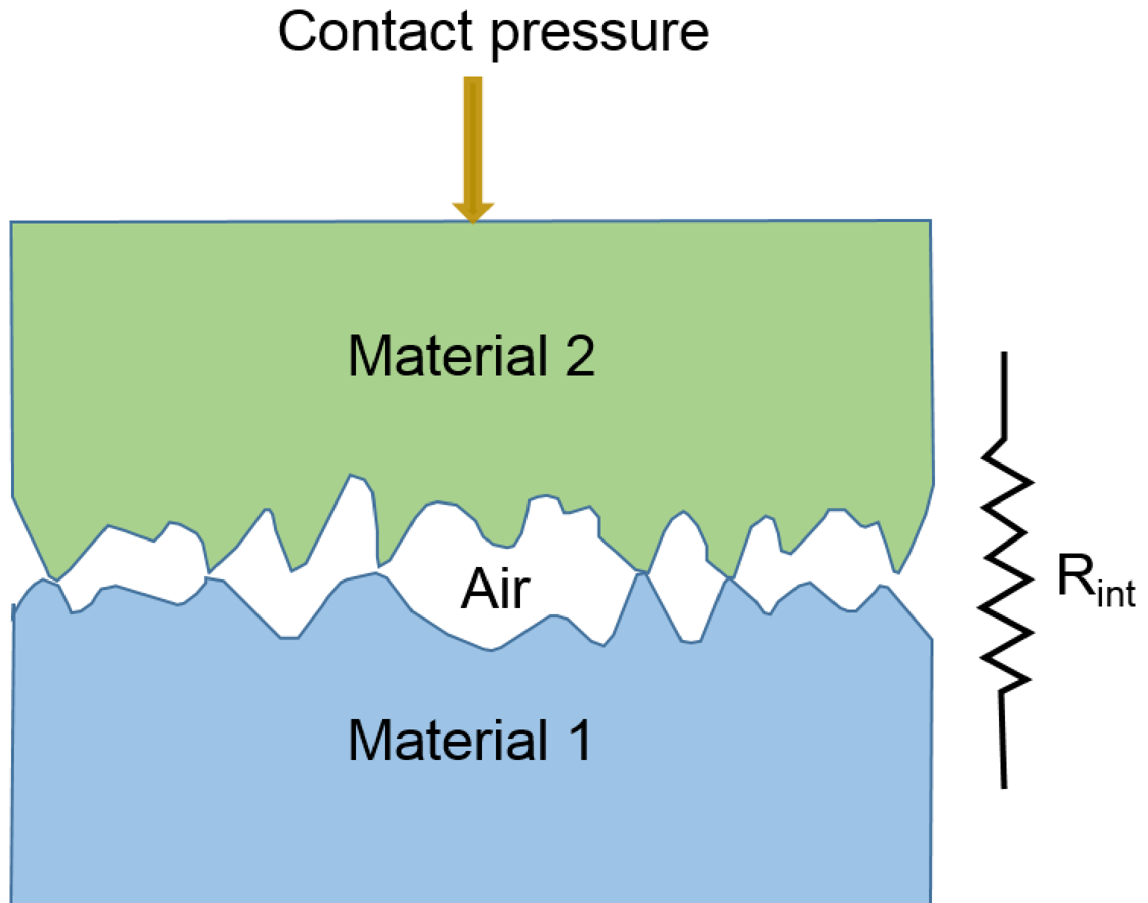

Figure 1-1 Scheme of contact interfaces at the joint of two materials without TIMs use (Note: R_{int} is the thermal contact resistance at the interface.). The micro and macro roughness of the joint of two surfaces can be seen even under the loading pressure, and most interface area is separated by air filled gaps.

المنارة للاستشارات
www.manaraa.com

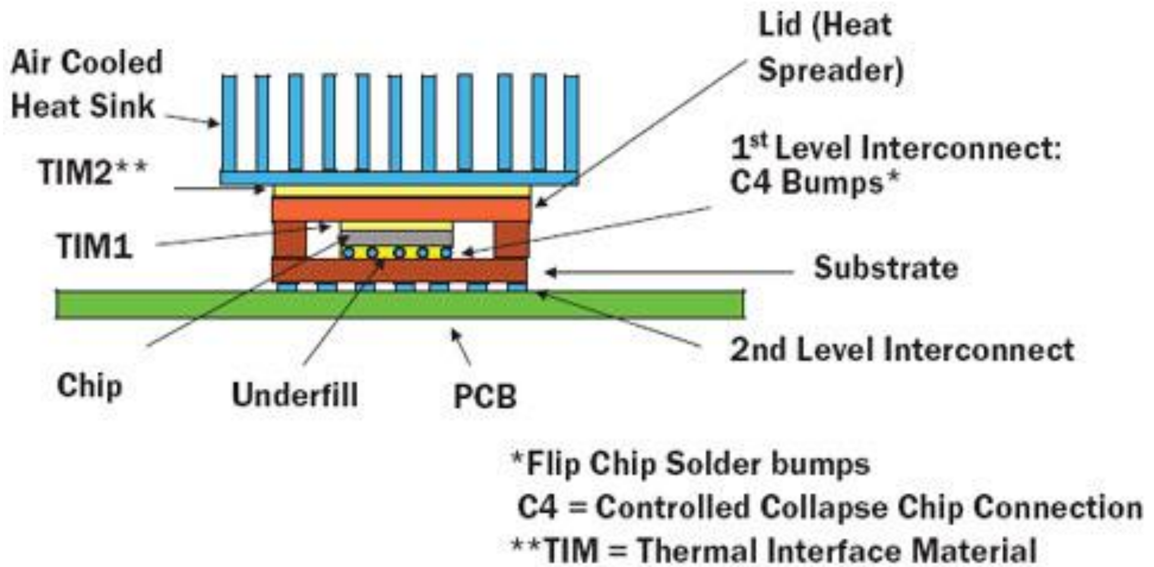

Figure 1-2 Schematic illustration for single lidded flip chip packaging [8], where a heat sink is attached to the lid of a heat spreader. In the commercial microelectronics packaging, TIM1 is the TIM to bond a chip with the heat spreader, where the expensive high-end solder is usually used. TIM2 is the TIM between the heat spreader and the heat sink, which is what most researchers have been work on.

المنارة للاستشارات
www.manaraa.com

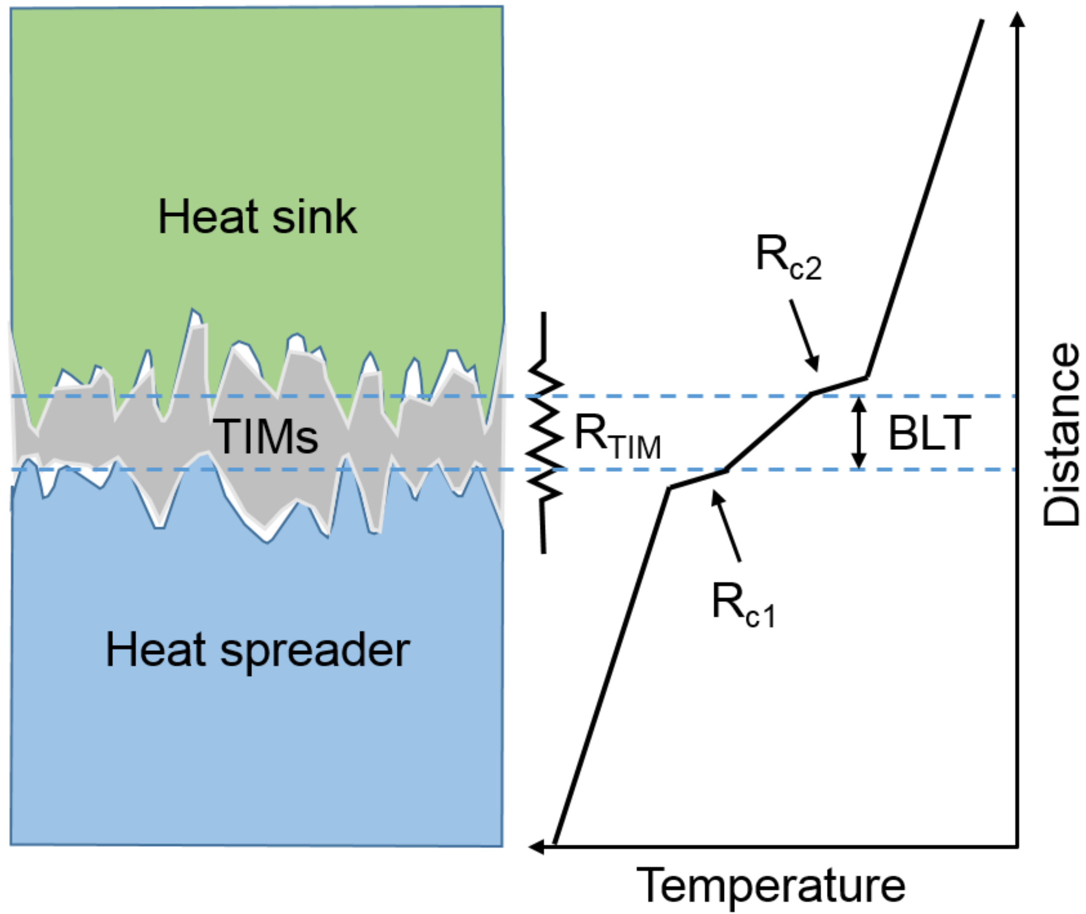

Figure 1-3 Schematic of the effective thermal resistance at the interfaces of the TIMs, R_{TIM} consists of the bulk resistance R_{bulk}, and two contact resistances at the interfaces R_{c1} and R_{c2}.

المنارة للاستشارات
www.manaraa.com

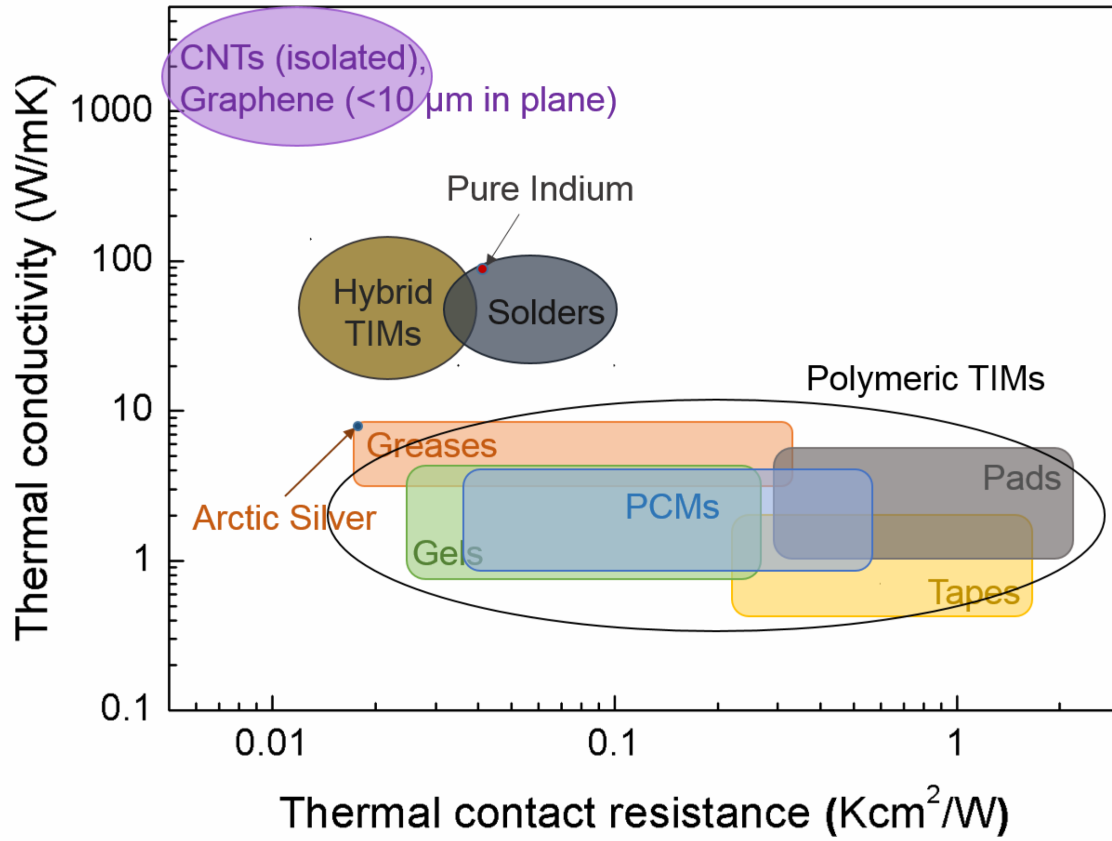

Figure 1-4 Comparisons of the novel hybrid TIMs in this study with various current TIMs on their thermal properties (k and R_c) as discussed in chapter 1. The cheaper polymeric TIMs have poorer thermal performances comparing with the expensive solders. High-performing CNTs and graphene cannot be applied to the market yet. The thermal conductivity of the hybrid TIMs in this study can compare to the high-end solder TIMs and their contact resistance achieves as low as that of the best thermal greases.

المنارة للاستشارات
www.manaraa.com

Chapter 2 AgNPs synthesis and sintering

2.1 Introduction

Metallic nanoparticles (NPs) are nano-sized clusters which consist of metal cores and organic shells, which help NPs to disperse well in the solvent and maintain their stability (prevent agglomeration) at room temperature [168-170]. Metal NPs have shown a number of quantum-size effects, for example, exhibiting an enhancement of magnetic and optical polarizability [171], Raman scattering [172, 173], reactivity of the surface atoms [174], diffusion coefficient [175, 176], etc. They have been demonstrated to have applications in many fields, such as catalysis [177], photonics [178], medicine [179], inkjet printing in electronics packaging [180-189], and here in this study, a sintered system for low cost [181, 185, 190-192]. Sintering indicates a process in which particles can weld together at temperatures below their melting point. Metallic NPs could be potential candidates for TIM. First, metals generally have a high k. Second, the melting points of metallic nanoparticles are much lower than those of bulk materials. Third, strong metal-metal bonding can be achieved by sintered metallic NPs.

There are many approaches to fabricate metal nanoparticles, and these can be classified into breakdown (top-down) and buildup (bottom-up) methods [193-195]. Relatively, bottom-up procedures can be designed to generate NPs with more uniform size, and more controllable shape and structures than top-down methods. When it comes to the

المنارة للاستشارات
www.manaraa.com

metal NPs preparation, they can be divided into two other different main categories [196]. The first is the physical method, which is based on subdivision of bulk metals, such as evaporation/condensation [197, 198]; the second is the chemical approach, which is based on the reduction of metal ions or decomposition of precursors to form atoms. Comparatively, the NPs of physical methods are usually those with larger size and wider size distribution than that of chemical methods. These two classification modes mostly overlap in the actual experiments.

Phase breakdown normally starts from bulk metals and an external powerful energy source, such as milling, during which the metal particle size from the bulk material will continuously reduce with the continuation of the process. Phase buildup can be either in q gas phase or a liquid phase, like chemical vapor deposition [197, 198] and wet chemistry method [199-205]. The wet chemistry method is the most widely used, because it is easier to control the particle size, distribution and morphology, and its mechanism is explained here [206, 207]. A metal compound precursor is first to dissolve in a solvent, and the reduction process starts as soon as a reducing agent is added, continuously producing metal atoms. However, the metal atoms are not in a stable phase and they will begin to aggregate, growing into clusters and nuclei, which are typically from 8 Å to 10 Å. Once the nuclei are formed, they will continue to grow into primary particles, which are a stable system. With more particles remaining in the solution, primary particles will then grow into larger crystalline particles by diffusion growth or into larger polycrystalline particles by rapid coagulation.

For bulk metal materials, their melting temperature is very high, e.g., the melting point of Ag is 960 ºC, and heat of fusion (ΔH_f) is 284.9 kJ/mol. However, when the particle

المنارة للاستشارات
www.manaraa.com

size of metal is reduced to nanoscale, the sintering temperature can be significantly decreased. C. P. Wong's group [208] has investigated low-temperature sintering behavior of AgNPs (~20 nm), and coalescence of AgNPs was observed starting at 150 ^{o}C. Annealing of the AgNPs led to dramatical increase of both density and electrical conductivity of the compact materials. During the sintering process, not only the particles size increases, but also the crystal grains in Ag particles grow bigger, which have higher degree of periodicity with a more ordered pattern and more stability, because of the second law of thermodynamics.

The sintering of metal NPs can be performed by using oven or furnace thermal heating [180, 209, 210], electrical field [211], microwave [183, 212], laser radiation [187, 195, 213], plasma [189] or triggered sintering by chemical agent at room temperature [214]. Upon heating, the first step is the removal of solvent and surfactant molecules surrounding the nanoparticles, resulting in direct physical contact of the particles, followed by the neck formation. The particles tend to diffuse to join adjacent particles, and continue to grow in order to reduce the overall surface energy of the system. Isolated nanoparticles merge to form a contiguous network of metallic bonding, the entire process of which is called sintering [215].

Silver nanoparticles (AgNPs) especially have received a lot of attention, because of their high electrical conductivity, high thermal conductivity, chemical inertness and excellent thermal stability properties [181, 208, 216, 217], for the high surface energy of AgNPs lowers their sintering temperature to around 150~200 ^{o}C and the high melting point (960 ^{o}C) of sintered silver makes them possible for relatively high temperature packaging

المنارة للاستشارات
www.manaraa.com

applications; In addition, the voids in the connectional silver layer after sintering throughout a network help to reduce the elastic modulus, which improves their reliability.

In this study, AgNPs were synthesized by the two-phase method with the assistance of alkane amine as the surfactant. The morphology of synthesized AgNPs were characterized by scanning electron microscope (SEM) and transmission electron microscopy (TEM), and the thermal properties were tested by thermal gravimetric analyzer (TGA). Their sintering process were carried out at 120 ^{o}C and studied by X-ray diffraction (XRD) and in-situ small angle X-ray scattering (SAXS).

2.2 Experiments

AgNPs were synthesized by the two-phase method [218], in which DI-water and toluene were used as the two immiscible solvents. Silver acetate was used as metal source and $NaBH_4$ was the reducing agent. The reduction process was confined to happen at the water-oil (toluene) interface. Alkane amine was the stabilizing agent to support AgNPs suspension, and the length of the alkane had a decisive influence on the size of the AgNPs.

The synthesis steps were: The 2 L reactor was filled with clean toluene, followed by the addition of a certain amount of dodecylamine (or octylamine), stirring to make it dissolve. Silver acetate was dissolved in toluene and appeared as a slurry. Transferred the silver slurry into the reactor with continuously stirring. The temperature was raised to enhance the mixing process, and then returned to reaction temperature when the solution appeared clear and amber. $NaBH_4$ was dissolved in DI-water, and added into the oil phase

المنارة للاستشارات
www.manaraa.com

dropwise. The oil phase turned into dark brown after the first several drops. Continuous stirring for 1 h to make the reduction reaction go to final completion.

After the reaction, the mixture was separated into two phases, the upper dark brown oil phase and the lower clear water phase. The water phase was discarded by using a separation funnel and the oil phase was collected. The oil phase was concentrated by rotary evaporation to get a dark brown paste with high viscosity. A mixture of clear methanol/ acetone was poured into the brown paste, and rotated in the rotovap for 2 min to precipitate AgNPs. The AgNPs were filtered through a fine-pore sized funnel, and washed by the methanol/acetone mixture. The final products were dried under vacuum and stored in the refrigerator for use.

The TGA test was carried out in a nitrogen atmosphere and the test mode was the stepwise isothermal method. The specific conditions set for the measurement are given as below.

(1) Abort next segment if %/min > 0.50;

(2) Ramp 20.00 °C/min to 600.00 °C;

(3) Abort next segment if %/min < 0.05;

(4) Isothermal for 1000.00 min;

(5) Repeat segment 1 until 600.00 °C.

This means the temperature ramp was set at 20 ºC/min until the sample started to lose weight at 0.5 %/min or faster. When this condition is reached, segment 2 of the program was stopped and segment 3 was begun, holding isothermal status until the weight loss rate of the sample slower than 0.05 %/min. At that point, the program would repeat and start with segment 1 again until achieving the final temperature of 600 ºC.

المنارة للاستشارات
www.manaraa.com

Among various sintering techniques of NPs, the thermal sintering method has been used due to its easy operation, low-cost setup and high efficiency. The sintering process of AgNPs has been studied first using XRD. Neat AgNP films were cast from paste solution on the kapton substrate, which is stable during the sintering temperature range while considered relatively clean in the XRD spectrum. The temperature of the heating stage was preset to 120 °C, and the AgNP films were quickly transferred to the stage and stayed for 10 s, 30 s, 1 min, 2 min, 5 min, 10 min, and 30 min, respectively. The XRD spectrum was collected for these samples after quenching to room temperature.

2.3 Results and discussions

Synthesized AgNPs are nano-scaled clusters consisting of metal cores and organic shells, which help maintain the stability of the nanoparticles at room or relatively low temperatures, and help AgNPs disperse uniformly in the solvent as well. SEM and TEM characterizations of "as synthesized" AgNPs are shown in figure 2-1. SEM micrograph shows that AgNPs are fairly uniform in size and can pack to form hexagonal orders locally. Statistics on particle sizes from TEM micrograph show AgNPs have a size centered at around 6 nm with a narrow distribution of ± 2 nm. AgNPs have reduced melting temperature comparing to the bulk silver, and can be sintered at low temperatures.

The result from figure 2-1 is for the AgNPs synthesized with long alkane amine. When using the shorter alkane amine, the AgNPs become bigger, e.g., SEM image for a batch of AgNPs in figure 2-2. The particle size can be large to 200~300 nm, and with wider size distribution.

المنارة للاستشارات
www.manaraa.com

The weight loss of the AgNPs was monitored using TGA, as shown in figure 2-3. Both the smaller size of AgNPs and the larger particles were characterized. The size characterization of these two kinds of AgNPs is displayed in figure 2-1 and 2-2. There are 3 weight loss stages for both of the samples. Both samples have little weight loss lower than 100 ^{o}C, which means there are seldom methanol and acetone left in the AgNPs. According to table 2-1, the weight loss of the first stage can come from the solvent toluene and water if there is any. For the second and the third stages, the weight loss may come from some free surfactant. After that, there still exists continuous but small weight loss, which may result from the bonded surfactant, more energy required to leave from the system upon heating.

By comparing the two weight loss curves, it can be seen that there is a greater excess of chemicals in smaller AgNPs (5 % weight loss for larger AgNPs and 15 % for smaller AgNPs), including the solvent and the surfactant, alkane amine. This is reasonable, for the smaller the particles have more surface area, and the more surfactant and more solvent will be captured by the AgNPs.

Combining with the previous TGA analysis of AgNPs, their sintering process can be illustrated in figure 2-4 [182, 219, 220]. Upon heating, solvent (toluene and a little water) is the first to evaporate, and followed by the free surfactant molecules surrounding the nanoparticles in accordance with an increasing boiling point, and then the bonded surfactant leaves as the temperature raises, resulting in surface metal atoms diffusing to join adjacent particles. As particles continue to grow in order to reduce the overall free energy of the system, isolated nanoparticles merge to form a contiguous network of metallic bonding. The connectivity via metallic bonding among fused AgNPs is the basis

المنارة للاستشارات
www.manaraa.com

for the construction of the TIM paste in this study, which is consistent with what Mylsamy [221] found that poor interfacial bonding of composites would lead to more energy dissipation than good interfacial bonding.

The XRD spectra of "as synthesized" and sintered AgNPs specimen are shown in figure 2-5. The peaks in XRD spectra are from crystalline silver, while the broad signals at angles lower than 35° come from kapton substrate. The first XRD peak at 38.1^{o} is Ag (111) reflection and is used to analyze the size evolution of AgNPs in films with the Scherrer equation, $L = K\,\lambda/\beta\,\cos\theta$ [222], where L is the mean size of the crystalline domains, K is the shape factor ($K = 0.89$), λ is the X-ray wavelength (1.54 Å), β is the line width at half of the maximum intensity, and θ is the Bragg angle. For the same Ag (111) peak in Figure 2-5, K, λ, and θ are all constants. As the peaks become sharper with increasing sintering time, the size of Ag particles grow from 10 nm as synthesized to about 22 nm after 1 min sintering and 65 nm after 5 min, according to the calculation using Scherrer equation. It is consistent with the statement that AgNPs sinter to form larger particles in order to minimize the overall free energy of the system by reducing surface areas.

Figure 2-6 shows the in-situ 1D SAXS signal of the Ag sintering process at 180 ^{o}C, which was carried out on the beamline in the Brookhaven National Laboratory (BNL). In this figure, the peak shifts to a lower Q value with longer sintering time, indicating that AgNPs grow larger upon heating at this temperature, which is accordant to the previous XRD result in figure 2-5.

المنارة للاستشارات
www.manaraa.com

2.4 Conclusion

The AgNPs synthesized form the two-phase method are uniform in size, which is demonstrated by SEM and TEM. Their size can be controlled by changing to different alkane chains of the surfactant amine, and the study shows that the longer chain of the amine surfactant, the smaller size of the AgNPs. The sintering process of AgNPs is verified by the combination of TGA, XRD and in-situ SAXS. Upon heating, the solvent and free surfactant trapped in the AgNPs is the first to evaporate, and followed by the bonded surfactant. AgNPs fuse to larger particles in accordance with the law of thermodynamics.

المنارة للاستشارات

www.manaraa.com

Table 2-1 The parameters for some possible chemicals in AgNPs

Possible chemical in AgNPs	Boiling point (°C)
Silver acetate	220
Dodecylamine	247
Octylamine	175
Toluene	110
Water	100
Methanol	65
Acetone	56

المنارة للاستشارات
www.manaraa.com

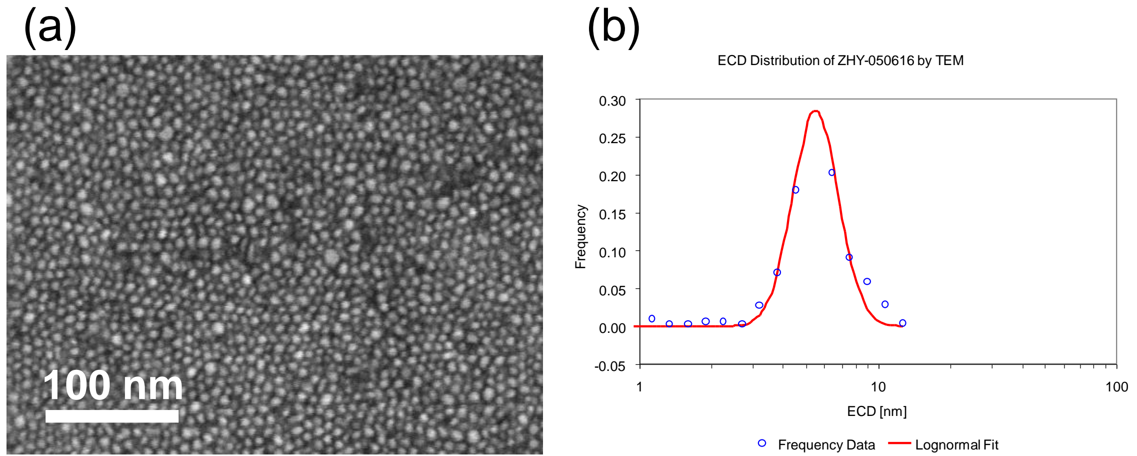

Figure 2-1 SEM image of AgNPs (a) shows that AgNPs have a uniform size, and TEM characterizations (b) show AgNPs have a size around 6 nm with a narrow distribution of ± 2 nm.

المنارة للاستشارات
www.manaraa.com

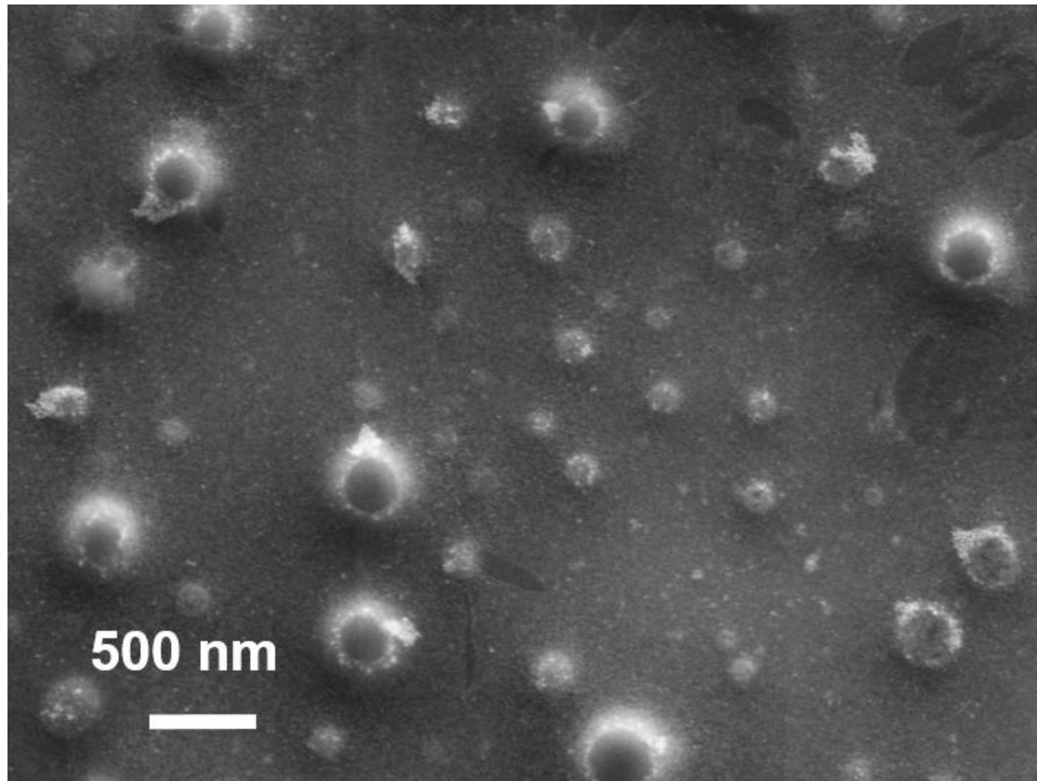

Figure 2-2 SEM characterization of AgNPs synthesized using a different amine with shorter alkane chains as surfactant, showing the size is less uniform ranging from tens to hundreds of nanometers.

المنارة للاستشارات
www.manaraa.com

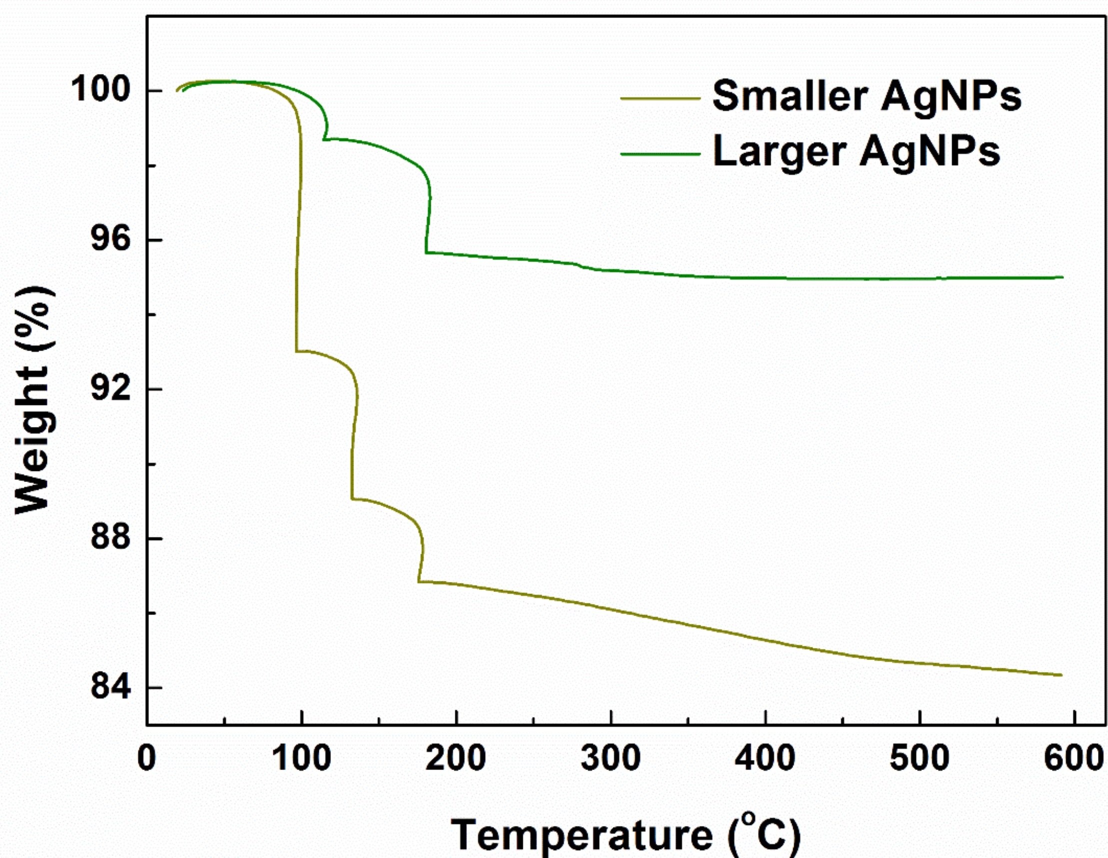

Figure 2-3 TGA analysis of smaller and larger AgNPs, showing isothermal weight loss in nitrogen upon heating. Both have three stages of weight loss, but the smaller AgNPs lose much more weight than the bigger AgNPs, which is consistent with the fact that smaller particles trap more surfactant and solvent.

المنارة للاستشارات
www.manaraa.com

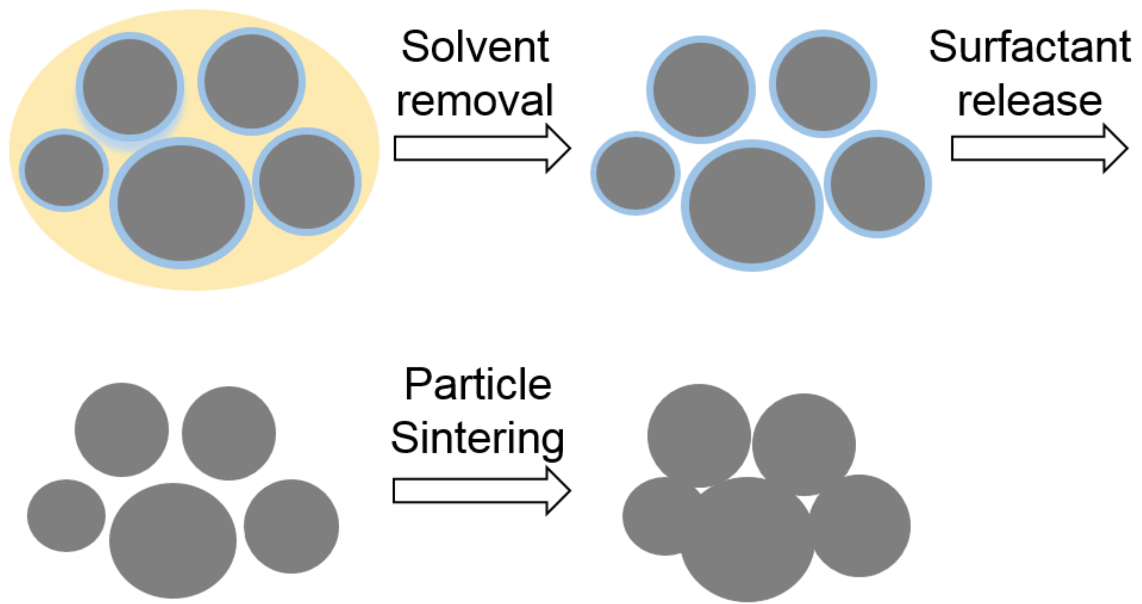

Figure 2-4 Schematic illustration of metal nanoparticle sintering upon heating. The sequence of the chemicals leaving the system with increasing temperature is solvent, free surfactant and bonded surfactant. After this, the nano-sized particles start to diffuse to form bigger ones, corresponding to the law of thermodynamics.

المنارة للاستشارات
www.manaraa.com

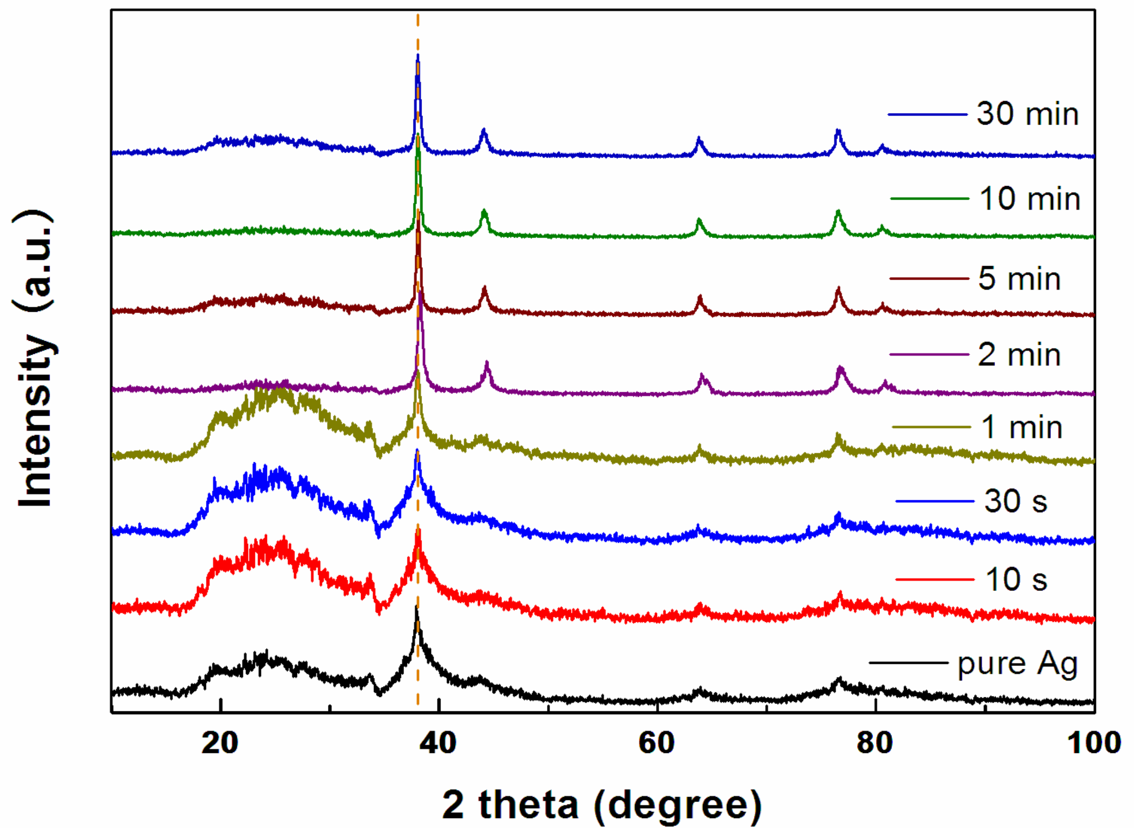

Figure 2-5 XRD spectra of neat and sintered AgNPs at 120 ºC for different durations. According to the calculation based on the Scherrer equation, the AgNPs grow to 22 nm after 1 min heating, and to 65 nm after 5min from 10 nm as synthesized.

www.manaraa.com

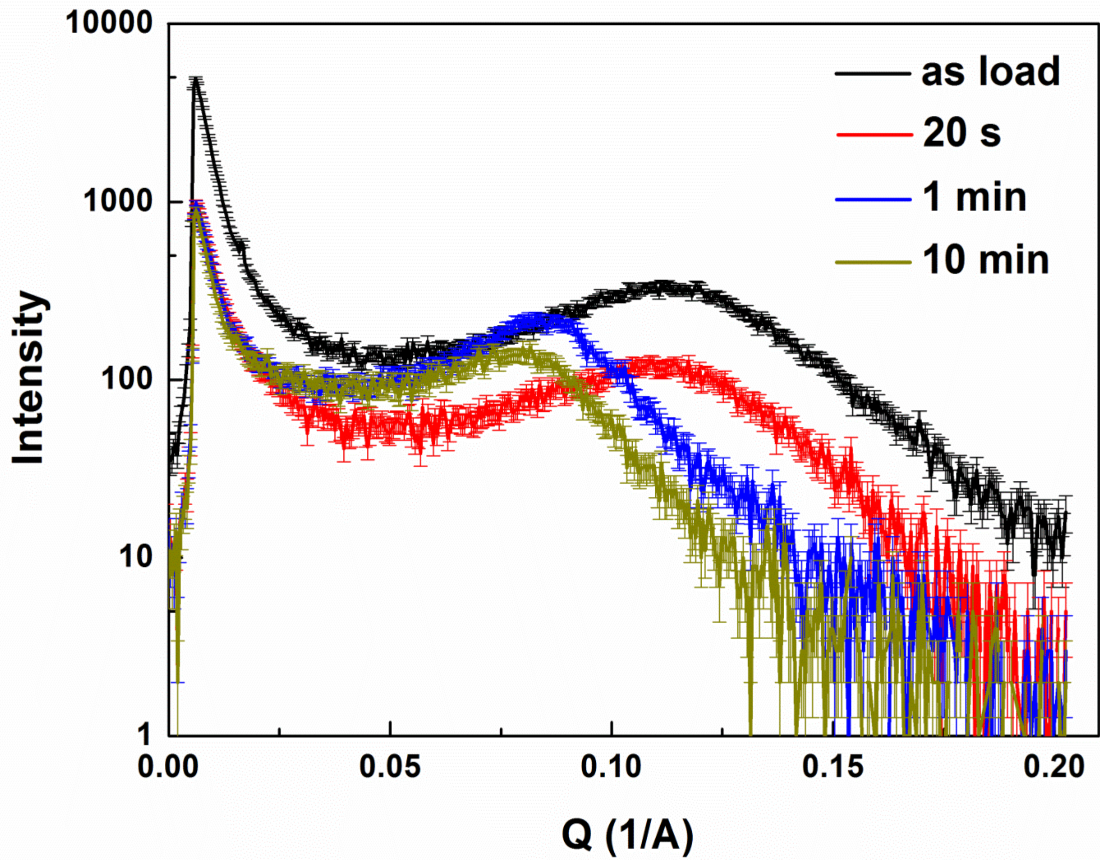

Figure 2-6 1D in-situ SAXS images for neat AgNPs at 180 ºC, showing that AgNPs grow larger with longer heating times, for the peak shifts to a lower Q value, which is accordant with the XRD result in figure 2-5.

المنارة للاستشارات
www.manaraa.com

Chapter 3 Nanocomposite TIM assembly preparation and characterizations

3.1 Introduction

Heat dissipation is a major challenge in high performance electronic devices, so the market is badly in need of high-end TIMs with economic manufacture. Thermal interface materials (TIMs) are used to fill the air gap at the interface between the heat sink and heat spreader to create more effective heat conducting. Current TIMs have either low conductivity, such as conventional thermal greases, or high costs, such as solder materials and indium metals [7, 49]. In this paper, we address a new resin-free nanocomposite TIM paste, taking the advantage of thermal paste and solder TIMs, and the details will be given in the following paragraph. The hybrid TIM paste that consists of AgNPs, commercial Ag nanoflakes (AgNFs) and commercial CuMPs offers a low cost and high performance solution.

In our previous studies, TIMs consisting of silver micron flakes ranging from 1 to 10 μm and AgNPs of 3~8 nm show *k* of 20~100 W/mK, higher than the best commercial thermal grease in the market, and comparable with high-end solder TIMs. In our current study, we use CuMPs instead of previous Ag micron flakes, and also introduce commercial AgNFs in order to reduce the cost. The resin-free pastes are expected to have good thermal

المنارة للاستشارات
www.manaraa.com

and mechanical performance, because both matrix and fillers are good thermal conductors, and they can sinter together to form a strong metallic network.

The assembling temperature could be as low as 125 °C due to the small size of AgNPs and AgNFs [192], and the assembling pressure of 7 MPa or lower. Upon heating, the organics in the TIM paste evaporate and AgNPs and AgNFs fuse to form a metallic network, resulting in good thermal and mechanical performance.

The sintered nanocomposite TIM was investigated using scanning electron microscope (SEM), energy dispersive X-ray spectroscopy (EDX), scanning acoustic microscope (SAM) and X-ray diffraction (XRD).

3.2 Experiments

AgNPs used for the TIM paste were synthesized in the lab, the characterization and sintering process of which have been reported in last chapter. Commercial AgNFs were purchased from Tokusen Kogyo Co. and used as received without further treatment. The average lateral dimension of AgNFs is about 300 nm and their thickness is about 10 nm. Commercial CuMPs with a diameter of 1~10 μm were obtained from Indium Corporation. They were soaked in dilute HOAc water solution (~1M) to remove oxide layers on the surface layer. After rinsing with DI water, CuMPs were dried in the vacuum oven and stored in the refrigerator for use. In this study, two different average particle sizes of CuMPs were used, 1~10 μm and 1~3 μm, respectively.

AgNPs, AgNFs and CuMPs with various mass ratio were mixed in an organic solvent with the addition of small amount of polymeric binder to form a homogeneous

المنارة للاستشارات
www.manaraa.com

paste. In a typical TIM composition, CuMPs account for more than 50 % by weight in the solid TIMs paste, thus reducing the materials cost of the TIM. The TIM paste was coated on both surfaces of two joining metal substrates. The assembled temperature ranged from 125 ^{o}C to 225 ^{o}C, the pressure was about 7 MPa or lower, while the duration time varied from 5 min to 20 min. Upon hot compression, most organic solvent evaporated and a sandwich of a resin-free TIM paste between was formed. The thickness of the TIM layer is about 20 to 200 μm.

The morphology of the sintered nanocomposite TIMs was investigated using scanning electron microscope (SEM), and the composition of the sintered TIM paste was explored by energy dispersive X-ray spectroscopy (SEM/EDX). The macrostructures of TIMs were examined in situ using scanning acoustic microscope (SAM) and X-ray imaging. The possible phase change of the metal alloy was measured using X-ray diffraction (XRD).

SAM was used to in-situ image the structure of TIM assemblies. SAM is an important non-destructive diagnosis technique for failure and reliability analyses of electronic components, such as plastic encapsulated IC packages, printed circuit boards, grid ball arrays, flip chip packages, bonded wafers [77, 223, 224], etc. The mechanism of SAM is based on differences in the propagation and reflection of ultrasonic sound waves through different media. In a typical test, the most contrast is obtained from the existence of voids in a condensed medium, which makes SAM particularly suitable for probing the uniformity and defects in TIM assemblies. The SAM can be used to detect defects, such as delamination, voids, cracks, and inclusions of various materials, like ceramics, metals,

المنارة للاستشارات
www.manaraa.com

glasses and plastics. Different imaging modes are possible in SAM investigation, and the amplitude mode (Amp) was used in this study.

X-ray imaging is another non-destructive testing technique to examine the internal structure and defects in a device, which has similar functions in the electronic industry, carrying out failure and reliability tests and detecting defects [225-227]. The mechanism relies on the intensity recording of the X-ray beam after it penetrates the tested sample. This technique can also be used to image ceramics, metals, glasses and plastic components.

3.3 Results and discussions

SEM was first used to study the binary TIMs containing AgNPs and CuMPs. Figure 3-1 shows the SEM images of TIMs consisting of AgNPs and CuMPs with a mass ratio of 3:7, sintered under 7 MPa compression pressure, at 125 ^{o}C (figure 3-1a), 150 ^{o}C (figure 3-1b) and 175 ^{o}C (figure 3-1c) for 20 min and at 200 ^{o}C for 5 min (figure 3-1d), 10 min (figure 3-1e) and 20 min (figure 3-1f). They all show metallic networks formed through AgNPs sintering. It assumes that higher sintering temperature and longer sintering duration times may help generate larger Ag particles and stronger bonding between AgNPs and CuMPs or the substrates [228].

Close examination of the network morphology in TIMs through higher magnification SEM micrographs is shown in figure 3-2. Sintered AgNPs can be seen at the surfaces of and between bigger CuMPs, with a size range from tens to hundreds of nanometers, consistent with the previous studies on AgNPs [33]. The continuous metallic

المنارة للاستشارات
www.manaraa.com

network formed through fused AgNPs is responsible for good thermal, mechanical and electrical performances.

Figure 3-3 shows the SEM images of TIMs consist of AgNPs, AgNFs and CuMPs sintered under 7 MPa compression pressure and at 200 ºC for 20 min. Figure 3-3a and b are TIMs containing 1~3 μm CuMPs and AgNFs with a mass ratio of 6:4, figure 3-3c and d are mixtures of CuMPs, AgNFs and AgNPs with a mass ratio of 6:2:2, and with the addition of 2 % poly(4-vinylpyridine) (P4VP) by mass as the binder. The micrographs in the left column show metallic networks formed through sintering AgNPs and AgNFs, in which the interconnected metallic contacts are responsible for good thermal, mechanical and electrical performances of the hybrid TIMs. From the corresponding higher magnification graphs in the right column of figure 3-3, sintered AgNPs can be seen on the surfaces of and among bigger CuMPs. Figure 3-3b shows that AgNFs sinter to form thin sheets of irregular shape and microns in horizontal size.

The sintering behaviors of hybrid composites of binary particles having only AgNP or AgNF as the active component clearly show that the active nano-particulates tend to aggregate and fuse, coating uniformly on CuMPs. The contacts among MPs appear to be limited, and large voids remain. The situation is greatly improved when both AgNPs and AgNFs are used and 2 % P4VP by mass is introduced. Figure 3-3c and d show that the void fraction is much reduced comparing to the other two TIMs. Presumably the coexistence of AgNPs and AgNFs disrupts the aggregation by each other, and the dispersed polymer chains further homogenize the composite, resulting in high uniformity and low voids hybrid TIM composites.

المنارة للاستشارات
www.manaraa.com

EDX is used for composition analysis of the sintered TIMs. As shown in figure 3-4, two points for elementary analysis are chosen, the upper point is for a big micron particle and the lower one is for a cluster of nanoparticles among the big particles. Data analyses show that copper is dominant at the large particle, as expected for the composition in CuMPs. The lower point is dominantly silver as expected. The EDX analyses are consistent with the understanding of the morphology as seen in figure 3-2 and 3-3 that CuMPs form the backbone of the metallic network while sintered Ag particulates remain among CuMPs forming necessary bondage within the network.

Figure 3-5 shows SAM and X-ray images of a TIM assembly containing 10 μm CuMPs and AgNPs sintered at 200 ^{o}C for 20 min. As the substrates are the flat and uniform copper foils, the defects should be from the TIM layer only. In the SAM image, we can see the main body of the sample is relatively uniform, while defects and voids appear mostly near two ends and at boundaries, which are due mostly to the manual coating processes. In the X-ray image, only some voids can be seen in the TIM layer. In this case, SAM method is chosen for the later mechanical reliability analyses.

Figure 3-6 shows XRD spectra for neat CuMPs and AgNPs, and their composite TIM pastes with the Ag-Cu mass ratio of 3:7 sintered at 200 ^{o}C for 20 min. The TIM spectrum composes of both Cu and Ag peaks in their neat form, and there is no appearance of new peaks, implying no formation of other significant phases. An interaction is expected between AgNPs and CuMPs at or near their corresponding particle boundaries. The existence of Ag-Cu interphases, if they do exist upon sintering of AgNPs, is beyond the XRD detection limit in this study.

المنارة للاستشارات
www.manaraa.com

3.4 Conclusion

We have investigated a new nanocomposite TIM paste, which contains commercial CuMPs with particle sizes of 1~10 μm, commercial AgNFs of about 300 nm in lateral dimension and 10 nm thick, and synthesized AgNPs of 6 ± 2 nm. Under an assembling temperature of 125~225 ºC, and a pressure of ~7 MPa, a continuous network is formed within the resin-free TIM between two substrates. SEM micrographs of TIMs with different compositions reveal percolated network structures that are responsible for extraordinary thermal performance. EDX characterization examines the distribution of the metal particles within the TIM paste. SAM and X-ray images show the general picture of the TIM layer structure, and voids can be observed better by SAM. XRD studies indicate the possible phase change of the composite of TIMs, implying no other significant phase formation.

المنارة للاستشارات
www.manaraa.com

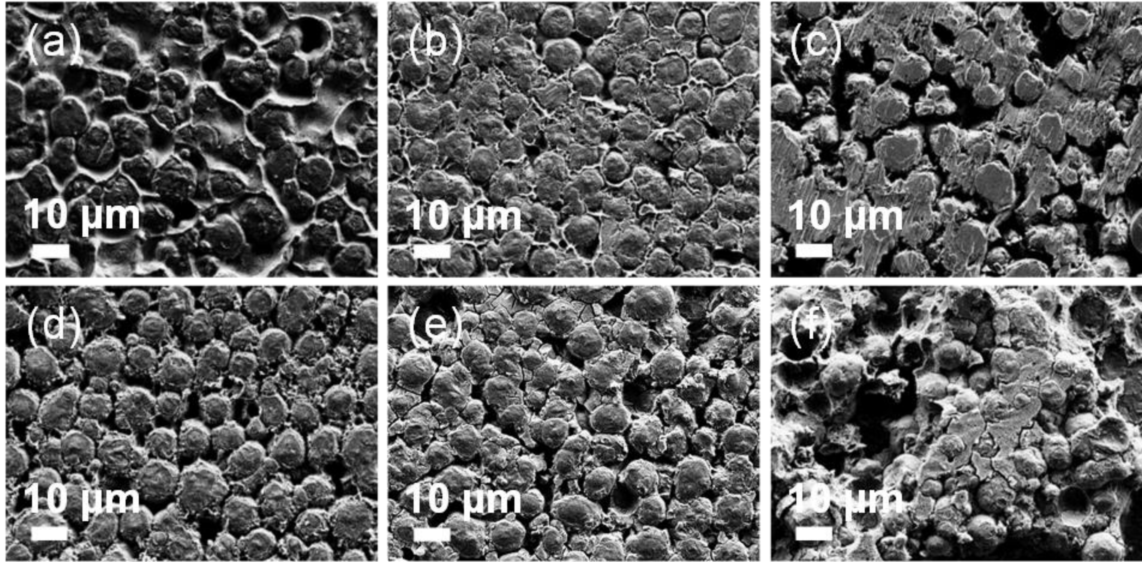

Figure 3-1 SEM images of hybrid TIM pastes of 10 μm CuMPs and AgNPs with a mass ratio of 7:3 sintered at 125 ºC (a), 150 ºC (b), 175 ºC (c) for 20 min; and at 200 ºC for 5 min (d), 10 min (e), and 20 min (f), showing the contiguous networks connected through fused AgNPs.

المنارة للاستشارات
www.manaraa.com

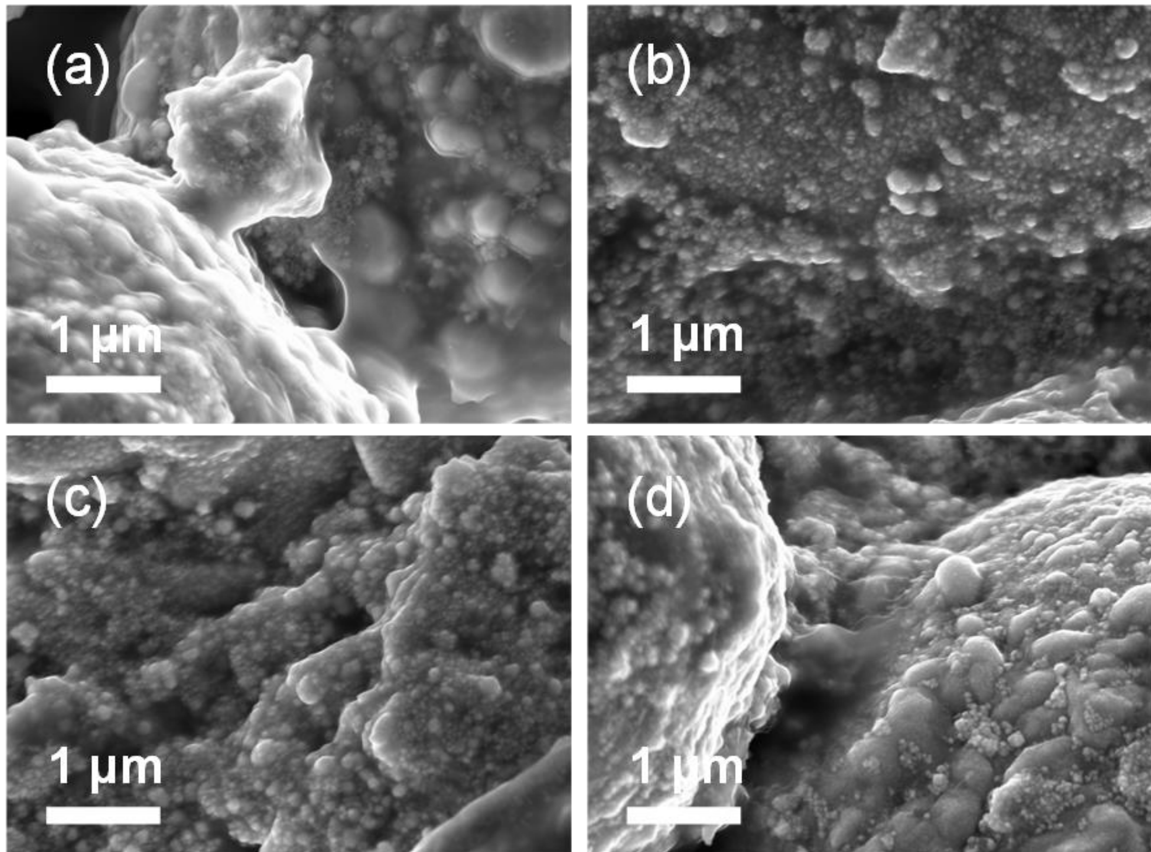

Figure 3-2 SEM images in higher magnification of hybrid TIM pastes of 10 µm CuMPs and AgNPs with a mass ratio of 7:3 sintered at 125 ºC (a), 150 ºC (b), 175 ºC (c), and 200 ºC (d) for 20 min, showing AgNPs grow larger and are distributed on the surfaces of and in between CuMPs. The higher the sintering temperature with the same sintering duration time, the more the large Ag particles grow.

المنارة للاستشارات
www.manaraa.com

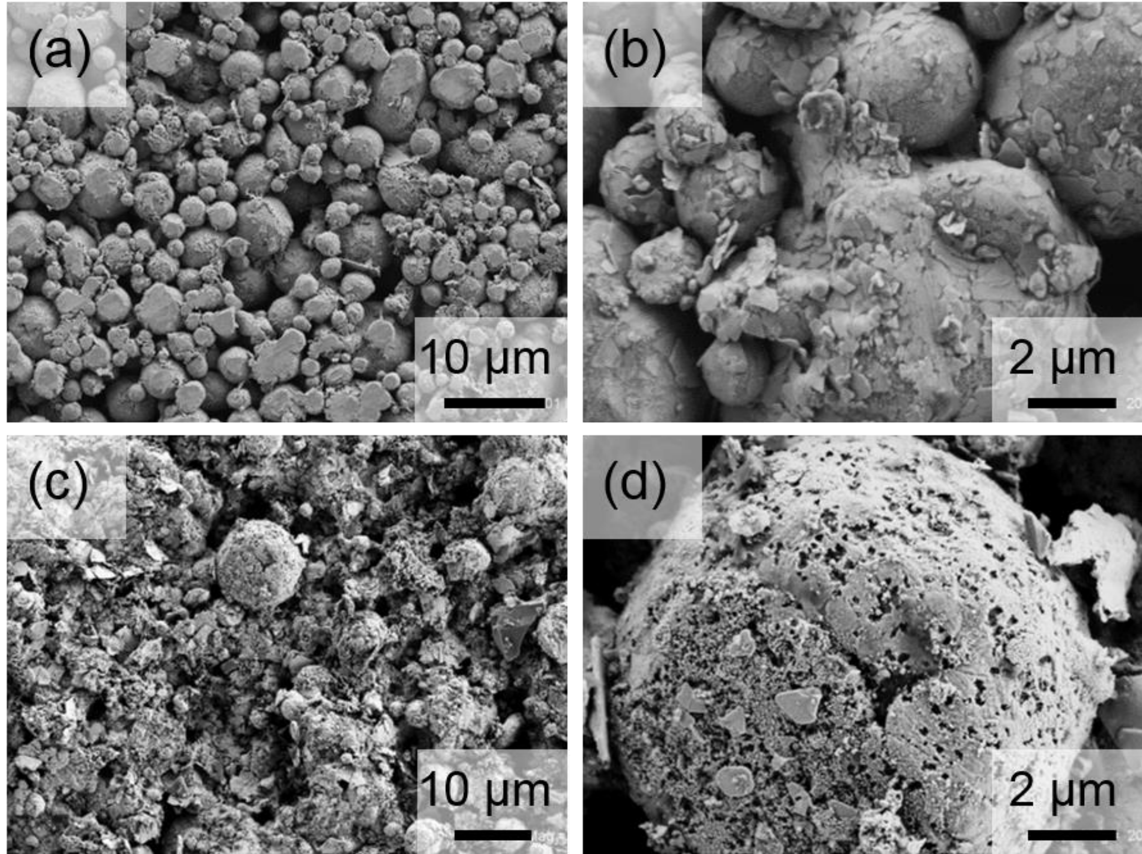

Figure 3-3 SEM images of hybrid TIM pastes sintered at 200 °C for 20 min of CuMPs and AgNFs with a mass ratio of 6:4 (a) and (b), of CuMPs, AgNFs, and AgNPs with a mass ratio of 6:2:2 + 2 % P4VP by weight (c) and (d). Fig. (b) and (d) are the magnified images corresponding to (a) and (c), showing the contiguous networks connected through fused AgNFs and AgNPs.

المنارة للاستشارات
www.manaraa.com

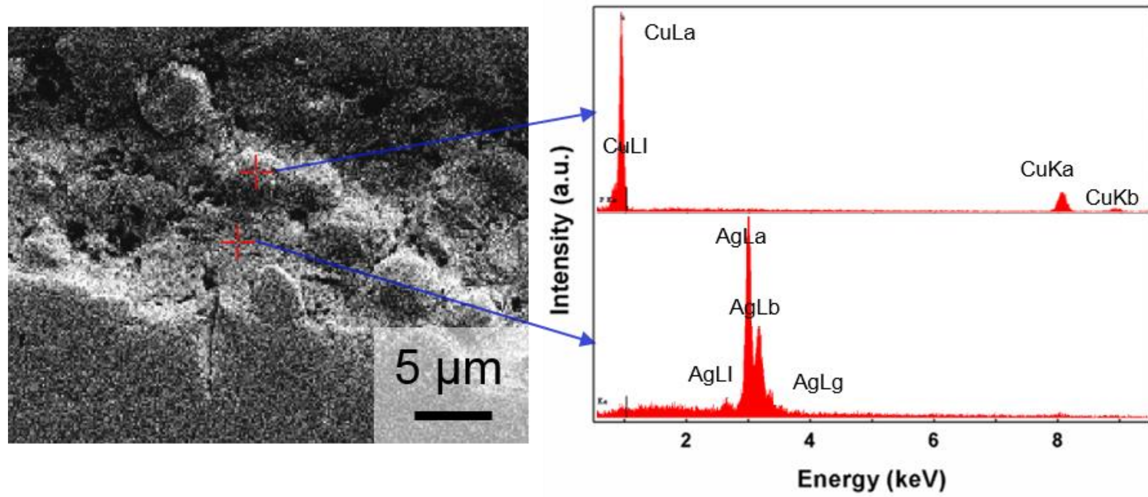

Figure 3-4 SEM and EDX analysis of sintered TIMs consist of CuMPs, AgNFs and AgNPs with a mass ratio of 6:2:2. The EDX data shows that copper is dominant at the large particles, and silver is dominant at the interval of large particles, which helps confirm the distribution of metal particles within paste.

المنارة للاستشارات
www.manaraa.com

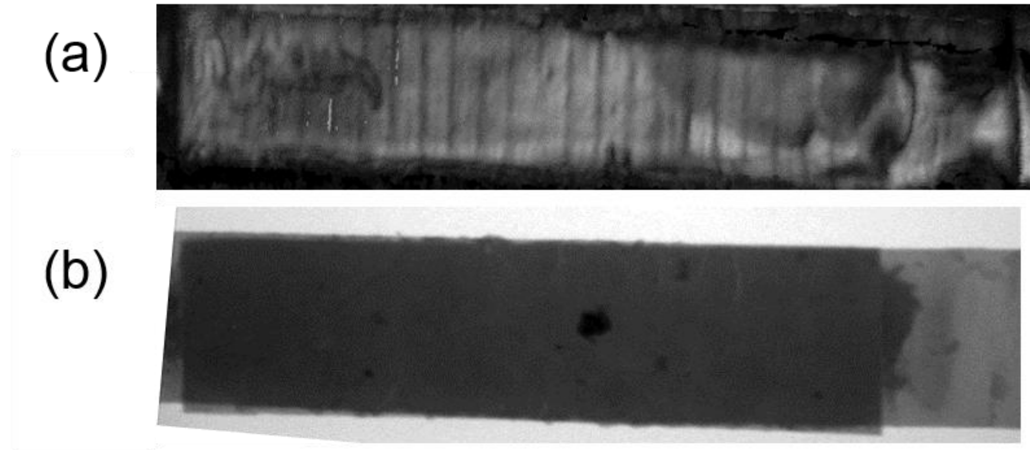

Figure 3-5 The SAM image (a) and the X-ray imaging (b) of the TIM layer in between two copper foils as the substrates. The TIM paste contains 10 μm CuMPs and AgNPs and was sintered at 200 ºC for 20 min. Both images show the uniform and non-uniform parts of the sintered TIM layer, and voids can be seen in the assembly.

المنارة للاستشارات
www.manaraa.com

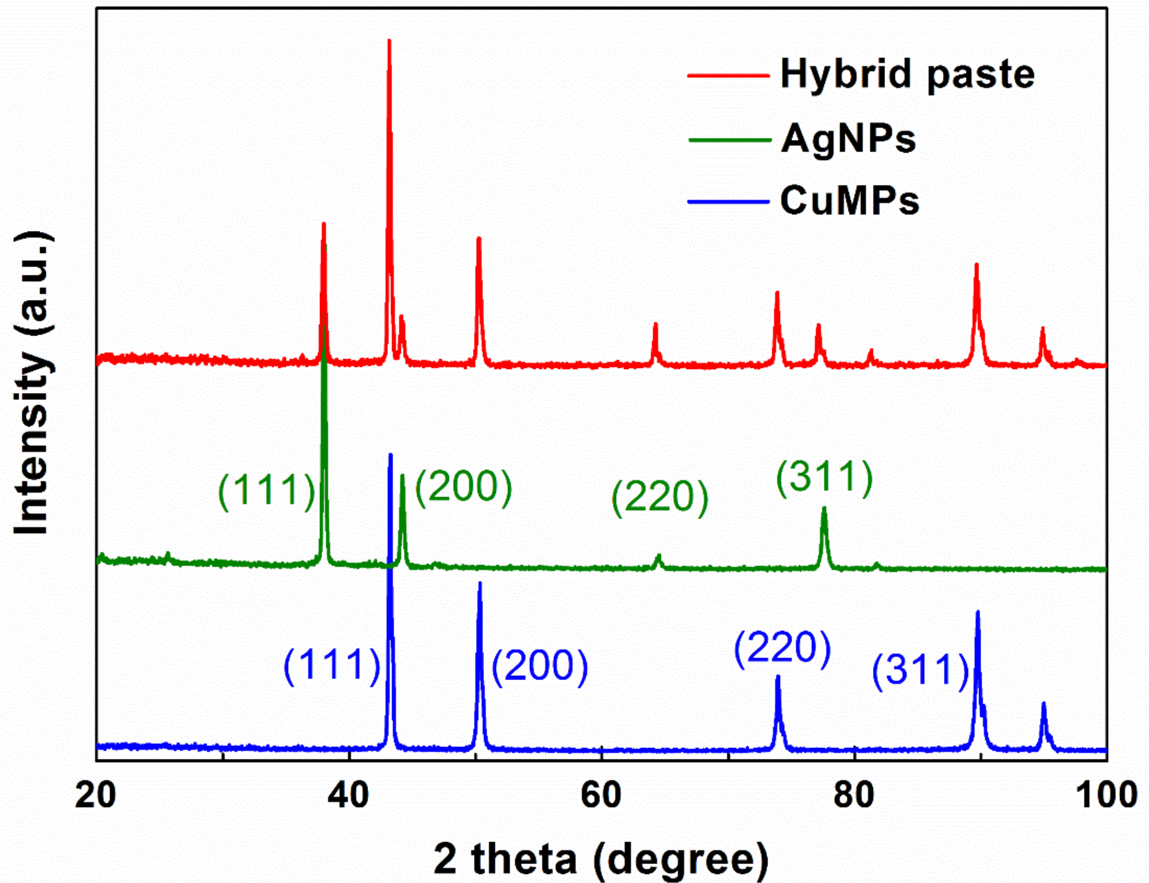

Figure 3-6 XRD patterns for a sintered TIM paste consisting of CuMPs and AgNPs with a mass ratio of 7:3, and sintered at 200 ºC for 20 min. The TIM spectrum is composed of both neat Cu and Ag peaks, and there is no appearance of new peaks, implying no formation of other significant phases.

المنارة للاستشارات
www.manaraa.com

Chapter 4 Mechanical and thermo-mechanical properties of the hybrid TIM assemblies

4.1 Introduction

It is important and necessary to study the mechanical properties of the TIMs as well as the thermo-mechanical properties, which mean their changes under the short and long term exposure in different environments, since the environment changes are the keys to potential failure of the system. As for the mechanical properties of the TIMs, 5 fundamental force loadings need to be mentioned here [57, 229]. They are tension, compression, bending, shear and torsion, the schematic of which is shown in figure 4-1. Tension involves the type of loading on either or both ends of a material plane to make it elongate or pull apart. Compression is the opposite of tensile loading which involves pressing the material together. Bending is applying a load to make a material curve, resulting in compressing the material on one side and stretching it on the other side. Shear involves a load parallel to the cross section to cause the material to want to slide across on the other side of the plane. Torsion is the application of a force to bring about twisting of a material.

In this study, tensile and shear tests were used to characterize the mechanical properties of the hybrid TIMs, obtaining the stress-strain curves, which help to evaluate the ability of a material to withstand mechanical damage. In the obtained tensile and shear stress-strain curves, the engineering stress and engineering strain are defined below [56]:

المنارة للاستشارات
www.manaraa.com

$$\sigma = \frac{P}{A_0} \tag{4-1}$$

$$\varepsilon = \frac{l_f - l_0}{l_0} \tag{4-2}$$

P is the loading force, A_0 is the initial cross-section area of the material (for tensile test it is perpendicular to the force, but for shear test it is parallel to the force), l_f is the final length of the measured material, l_0 is its initial length. The ultimate tensile stress is the maximum stress level that the material can withstand before failure.

The tensile and shear tests were carried out on the sandwich hybrid TIM samples prepared under hot compression with the bond tester, and their thermo-mechanical properties were studied by comparing the tensile curves after different thermal cycles in the shock chamber. Scanning acoustic microscope (SAM) was used to image the structure of TIMs in situ without breaking the assembly in order to gain better insights in the extraordinary thermo-mechanical performance of hybrid composite TIMs. SAM is a non-destructive diagnostic technique that is based on differences in the propagation and reflection of ultrasonic sound waves through different media [76, 230]. In a typical test, most contrast is obtained from the existence of voids in a condensed medium, which makes SAM particularly suitable for probing the uniformity and defects in TIM assemblies [231]. Different imaging modes are possible in SAM investigation. The most commonly used amplitude mode (Amp) images to indicate the macrostructure changes in TIM assembly upon thermal cycling are shown.

المنارة للاستشارات
www.manaraa.com

4.2 Experiments

Both tensile and shear tests of the TIMs were carried out on the Dage series 4000 and 4000+ bond tester. As shown in figure 4-2, Dage 4000 is the most advanced bond tester available. The multipurpose bond tester sets the industry standard in bond testing, offering unsurpassed accuracy and repeatability of data. It can perform die shear tests up to 100kg, ball shear tests up to a 5 kg cartridge, clod bump pull tests up to a 5 kg tweezer cartridge, and push tests up to 50 kg. This system also includes a microscope, and the field of view can be adjusted from wide to close up and is ideally suited for the testing on micro feature applications [232].

Figure 4-3a shows the schematic model designed for the shear tests, which is the sandwich assembly with a nanocomposite TIM layer in between. A small and thicker square Cu foil was mounted on a larger Cu foil. The larger Cu foil is about 100 μm thick, while the smaller Cu foil piece is about 1 mm thick and with an area of about 3 mm by 3 mm. The setting for shear test is ball shear mode with a cartridge of 50 kg, the shear test speed is 200 μm/s, and the shear height is 10 μm. The test type is the destructive test, which means the loading force will increase until the sample fails or the maximum range is reached during the test. Figure 4-3b shows an example of the shear stress-strain curve, where the ultimate shear strength is the highest strength at which the sandwich TIM assemblies fail.

Figure 4-4a illustrates a TIM assembly with two identical 100 μm Cu foils as the substrates, and the area of a TIM paste in between is about 3 mm by 10 mm. The setting for tensile test is the wire pull mode with a cartridge of 5 kg, and the test speed is 200 μm/s.

المنارة للاستشارات
www.manaraa.com

The tensile test would stop until the sandwich sample was pulled apart or the tester reached the highest loading force. A required typical tensile stress-strain curve of TIM layers is shown in figure 4-4b in which the TIM sample was not broken when getting the highest loading with the composition of AgNPs and 10 μm CuMPs with a mass ratio of 3:7, and sintered at 200 °C for 20 min.

Both the shear and tensile tests were carried out in air at room temperature. For a TIM with determined composition, the comparison was made with different sintering temperatures, such as 125 °C, 150 °C, 175 °C, 200 °C and 250 °C, and varying sintering duration times, such as 2 min, 5 min, 10 min, 20 min and 30 min. All the TIM assemblies were prepared by the hot compression process under a pressure of about 7 MPa. At least 3 samples were made under one given preparation condition and the mechanical tests were applied.

The thermo-mechanical properties of the hybrid TIMs were tested by recording their tensile stress-strain curves after different numbers of thermal cycles in the Espec TSE-11-A thermal shock chamber. Figure 4-5 shows a typical profile of 50 thermal cycles between -50 to 150 °C, and the duration of each cycle is 20 min. After each 10 min at -50 °C, the chamber would automatically shift to 150 °C and continue at this temperature for another 10 min. After a certain number of thermal cycles, TIM assemblies were tested with the same tensile test on the Dage machine. The change of the mechanical behavior with increasing thermal cycles indicates the thermo-mechanical reliability of the TIMs. Besides the samples with identical Cu foils as the two substrates, the sandwich samples with two different substrates, one copper foil and one invar foil with much different coefficients of thermal expansion, were also prepared for the thermo-mechanical properties study.

المنارة للاستشارات
www.manaraa.com

4.3 Results and discussions

Figure 4-6 shows the result of ultimate shear strength from the shear tests for the samples with various sintering conditions, at different temperatures (125 ºC, 150 ºC, 175 ºC, 200 ºC and 225 ºC) for the same sintering time, and different sintering times (2 min, 5 min, 10 min, 20 min and 30 min) at the same temperature. There are two compositions of the TIM, one is AgNPs and 3 μm CuMPs, and the other is AgNPs and 10 μm CuMPs. Both compositions have the same Ag and Cu mass ratio of 3:7. It can be observed that with the same sintering time duration, the higher heating temperature, the greater ultimate strength of the specimen. While at the same sintering temperature, the longer sintering duration, the larger ultimate shear strength of the TIM samples. The ultimate strength of the TIM sandwich samples ranges from 2 MPa to as high as 20 MPa. By comparing the two compositions of the TIMs, there is not much difference between the yield strength of TIMs with larger or smaller size of CuMPs.

For the tensile test, most of the sandwich samples were intact at the maximum load of 5 kg, which are non-destructive tests. To assess the quality of the TIM assemblies, we use the integral area under the entire stress-strain curve, i.e., the energy density of the TIM assemblies, to indicate the sample characteristics and compare the effects of sintering conditions and cyclic thermal shocks in a semi-quantitative method. However, the energy density not only includes the energy density absorbing by the TIM layer, also involves that of the two substrates, which are easily ductile thin Cu foils and will contribute to the total integral energy density. In this case, it can be assumed that the mechanical behaviors of the Cu foils are the same during the tensile test and their energy density change are also the same, for all the TIM samples were made in the same size. Therefore, the total integral

المنارة للاستشارات
www.manaraa.com

energy of the TIM assemblies can still represent the relative energy density of the TIM layers. During the data analyses, we can compare the mechanical performance using the changing trend of the relative energy density of the TIM assemblies, and the specific values are meaningless.

Figure 4-7 shows the effects of sintering temperature and time on the relative energy density of the TIM assemblies. There is only one composite used in the test, AgNPs and 10 μm CuMPs with a mass ratio of 3:7. The assembling temperatures are 125 ^{o}C, 150 ^{o}C, 175 ^{o}C and 200 ^{o}C, and sintering times are 5 min, 10 min and 20 min. Data shows that the total relative energy density increases with both incremental sintering temperatures and times. The effect of temperature is more prominent in this study, while sintering time from 5 min to 20 min does not appear to alter the relative energy density result much. There is not so much difference found on the relative energy density of TIMs with bigger and smaller CuMPs, which is similar to the previous shear test results.

The thermo-mechanical performance of TIMs was investigated which is critical for reliable TIM applications. Considering the constraints of process temperature and duration, we chose the assemblies sintering condition at the temperature of 200 ^{o}C for 10 min. Figure 4-8 shows the comparisons of integral energy density from the related tensile stress-strain curves upon the thermal cycling. Figure 4-8a is the result for the TIM containing AgNPs and 10 μm with a mass ratio of 3:7, and 4-8b for the TIM with the same mass ratio containing 3 μm CuMPs. Both TIM assemblies were prepared with two same Cu foils as the substrates, and survived 5 kg loading after 2000 thermal shock cycles between -50 to 150 ^{o}C. Similar mechanical and thermo-mechanical behaviors were observed for the TIM with different sizes of CuMPs. The relative integral energy density of TIM assemblies

المنارة للاستشارات
www.manaraa.com

value reduces with the ever-increasing number of thermal cycles which may demonstrate the TIMs stiffening over the thermal cycling. Close analysis in figure 4-8a with the most beginning result indicates the relative integral energy density decreases more quickly with the first few thermal cycles.

SAM images in figure 4-9 show the inner morphology of a TIM assembly containing 10 μm CuMPs sintered at 200 ºC for 20 min without breaking it, as prepared (a) and after 50 thermal shock cycles (b). The main body of the sample is uniform, while defects and voids appear mostly near the two ends and at boundaries, which are due mostly to the manual coating processes. Just after 50 thermal cycles, big changes have generated on structure of the TIM layer, which may correspond to the more rapid change of the relative energy density at the first few cycles in the thermo-mechanical result. The surface texture features of the TIM layer appear to be smoothened, large voids became smaller and some small voids disappear, indicating that initial thermal cycling are beneficial for the morphology and mechanical properties of the TIM paste.

As for the thermo-mechanical reliability of electronic devices, the differences in coefficients of thermal expansion (CTEs) between bonding solids play a critical role [71]. Most of previous studies focus on TIMs bonding two identical Cu foils as substratesnwhich have no CTE mismatch. To confirm the good thermo-mechanical performance of the composite TIMs, the invar foil was used as the other substrate bonding the Cu foil. The linear CTE of invar is 1.2 ppm/ºC, which is similar to that of silicon, while the linear CTE of the Cu foil is 17 ppm/ºC. The schematics of a TIM assembly with mismatched substrates is shown in figure 4-10a. Figure 4-10b shows the stress-strain curves from the elongation test upon thermal cycling of the TIM with AgNPs and 10 μm CuMPs, and figure 4-10c is

المنارة للاستشارات
www.manaraa.com

the elongation result for the TIM with 3 μm CuMPs. Both TIM assemblies were sintered at 200 °C for 20 min in between the invar and Cu substrates.

A comparison of the stress-strain curves in figure 4-10b and c indicates the stiffening of TIM assembly upon thermal cycles, which is similar to TIMs bonding two identical Cu substrates. Both TIM assembles have gone through more than 10000 thermal cycles without failure, and survived further pulling tests up to 5 kg of load without breaking. Their relative integral energy density changing trend is also consistent with the previous data in figure 4-8. We have demonstrated high thermo-mechanical reliability of the resin-free hybrid nanocomposite TIMs even between the invar and Cu foils with much different CTEs.

The fracture mechanism is further investigated on the sandwich TIM samples using SEM to get micron-to-nano-view of the failure parts. Figure 4-11 shows the SEM images of the internal structures of the nanocomposite TIM, where the TIM samples were assembled still through hot compression process at 200 °C for 20 min, and separated by strong external force. Figure 4-11a and b are for the TIM containing 3 μm CuMPs, AgNFs and AgNPs with a mass ratio of 6:2:2, while figure 4-11c and d for the same metal materials and with the addition of 2 % polymer binder. In order to figure out where the failure was taking place within the composite upon fracture, particulate fields were chosen for SEM. Figure 4-11 a and c are for the areas with least TIMs after assemblies broken, and there are still particles covering on the substrates and no bare surface is observed. Thus, it is assured that the failure doesn't happen on interfaces between the substrates and the TIMs, which is totally the cohesive failure, not adhesive failure. In images b and d for the areas with most TIMs, it can be seen that the failure exists mostly at the interfaces of Ag particles, and some

المنارة للاستشارات
www.manaraa.com

also happens at the interfaces between CuMPs and Ag particles. Therefore, the possible enhancement work lies on the bonding connection between the metal particles.

4.4 Conclusion

The study of various sintering conditions with both shear and tensile tests shows higher sintering temperature and longer sintering time can make stronger and tougher TIM assemblies. Further demonstration of the excellent thermo-mechanical performance of hybrid TIM pastes is achieved in sandwich assemblies using two substrates, invar and copper foils, with a linear CTEs mismatch exceeding 15 ppm/^{o}C, which have gone through more than 10000 cycles of thermal shocks between -50 and 150 ^{o}C without failure. SAM images show the existence of voids in TIM assemblies and the evolution of void structures during the thermal cycling, which may be partially responsible for stiffening of the TIM assemblies. SEM on the fracturing structures shows that the TIM assemblies fail at the interfaces of the metal particles, either among Ag particles themselves or between Ag particles and CuMPs.

المنارة للاستشارات
www.manaraa.com

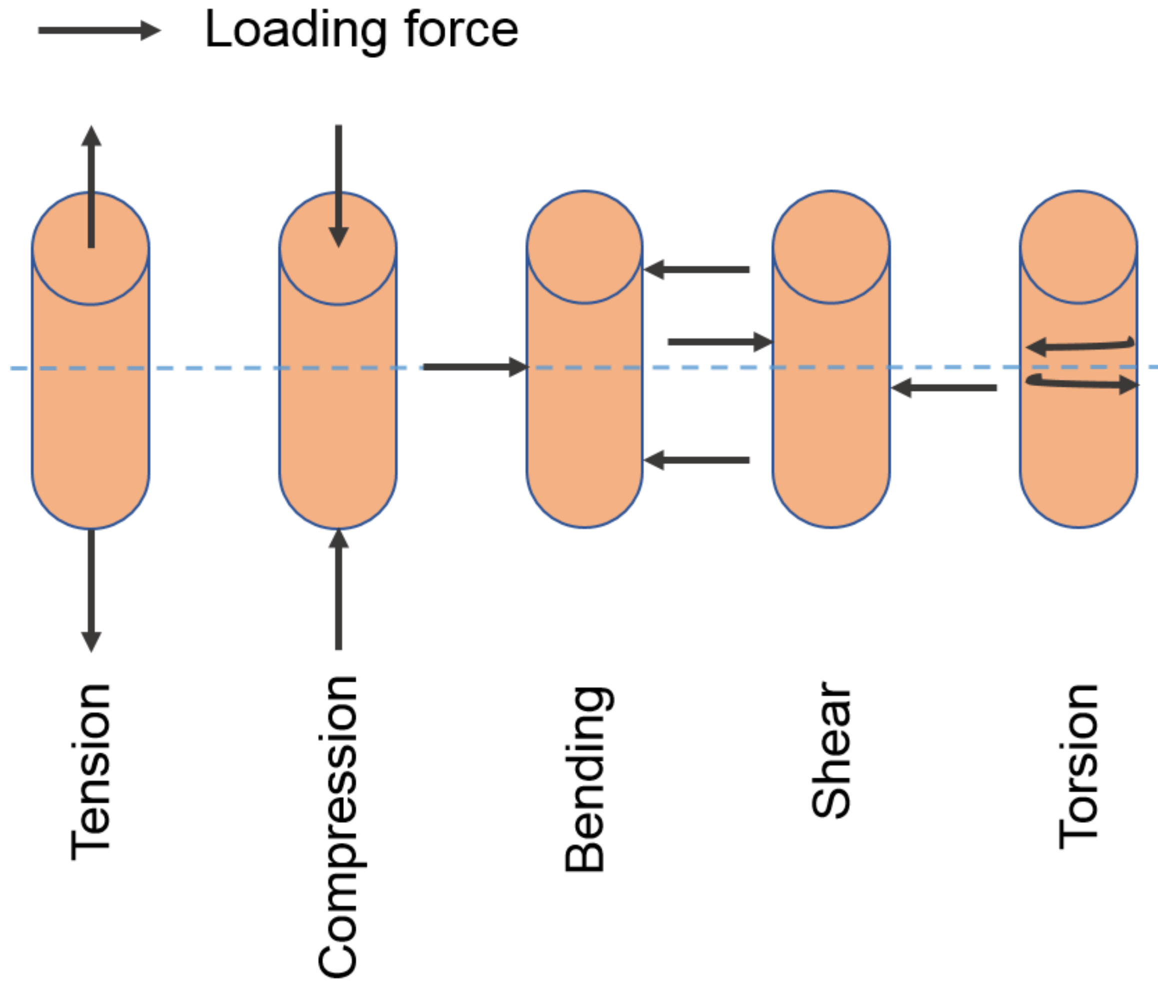

Figure 4-1 Schematic of five typical loading categories on the materials: tension, compression, bending, shear and torsion, which are classified by where the force loaded on the materials and the directions of the force.

المنارة للاستشارات
www.manaraa.com

Figure 4-2 Schematic of the Dage series 4000 and 4000+ bond tester, which can perform shear, pull and push testing, covering all test applications. With the assistance of the microscope, it is ideally suited for macro positioning.

المنارة للاستشارات
www.manaraa.com

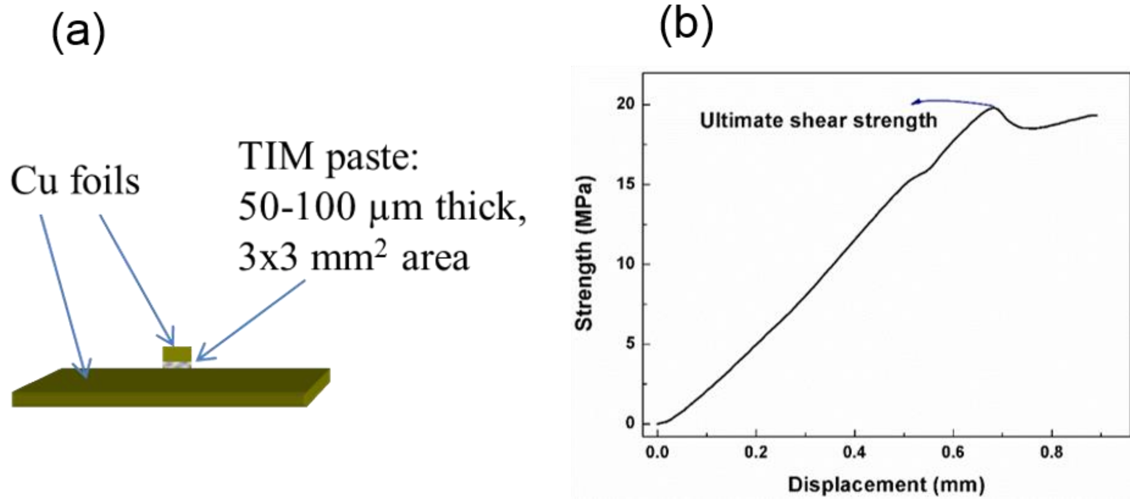

Figure 4-3 Schematic illustration of the TIM sample design for shear test (a) and an example of the shear stress-strain result (b). In the sandwich sample for shear test, the larger Cu foil is about 100 μm thick, while the smaller Cu foil piece is about 1 mm thick and with an area of about 3 mm x 3 mm. The TIM layer in between is about 50~100 μm thick.

المنارة للاستشارات
www.manaraa.com

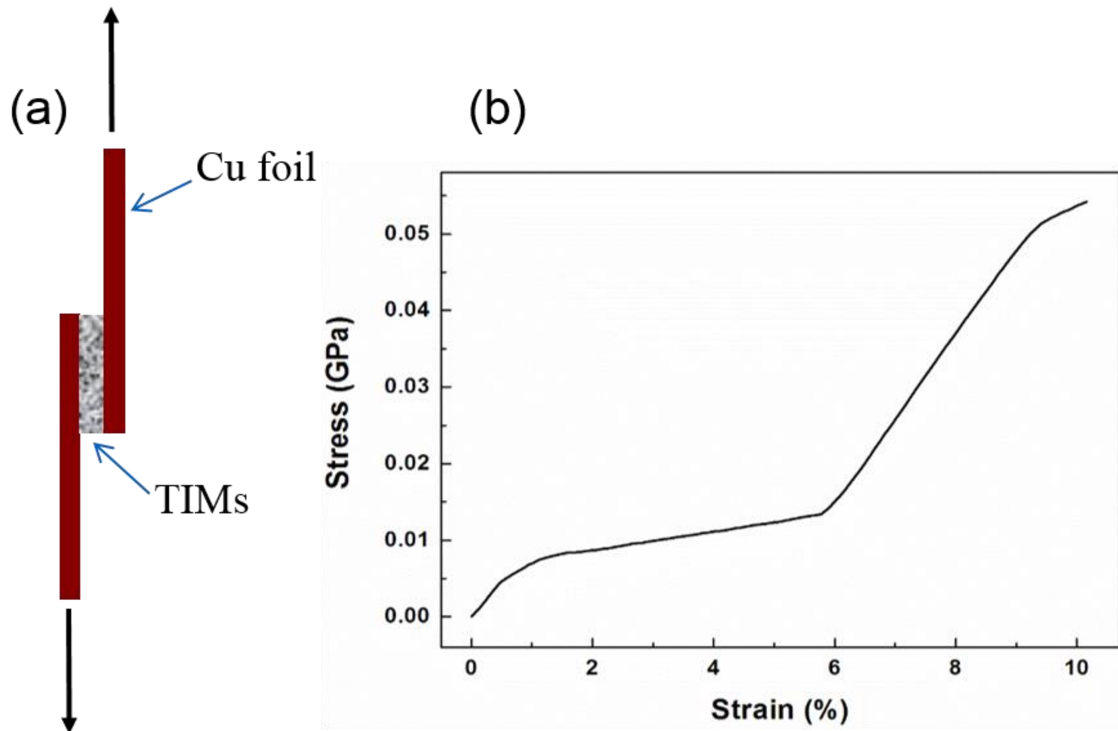

Figure 4-4 Schematic illustration of the TIM sample design for tensile test (a) and an example of tensile stress-strain result from the wire pull mode (b). The TIM assembly for tensile test is prepared with two identical 100 µm Cu foils as the substrates, and the size of the TIM paste is about 3 mm x 10 mm. The TIM layer between the two cooper foils is also about 50~100 µm thick.

المنارة للاستشارات
www.manaraa.com

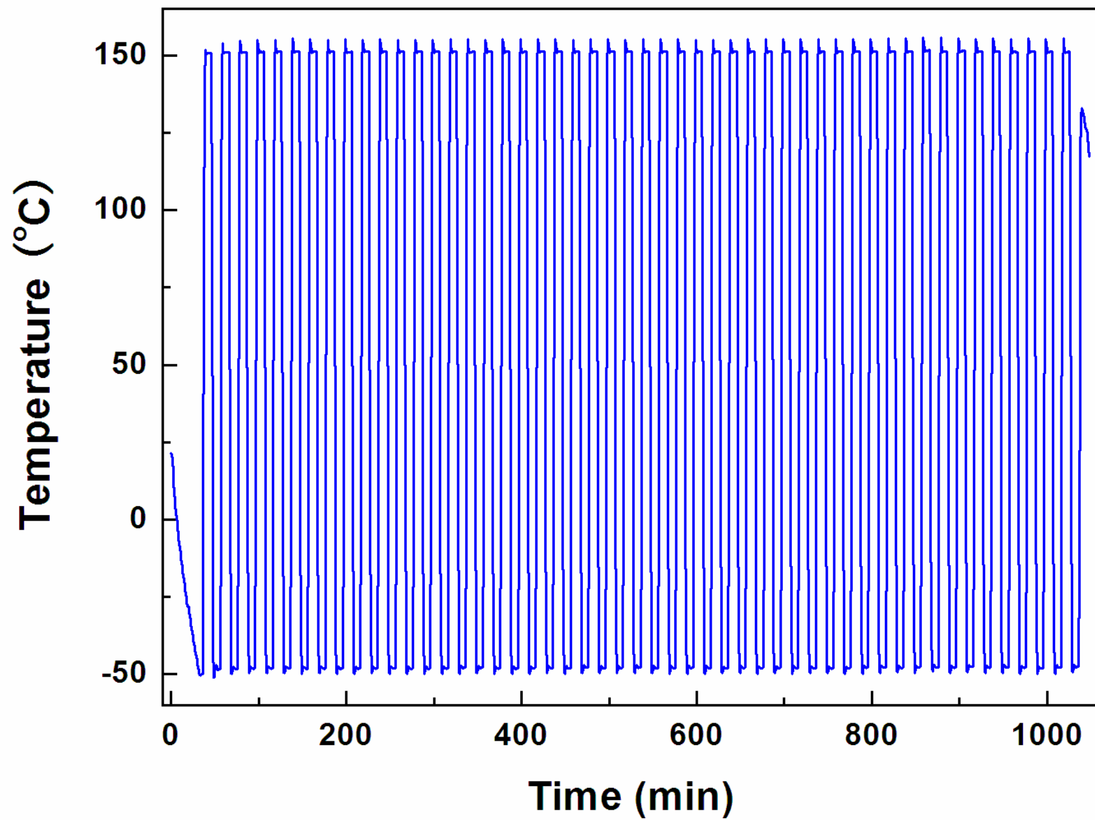

Figure 4-5 Thermal profiles of 50 thermal cycles from -50 to 150 ºC in the Espec TSE-11-A thermal shock chamber. The duration of each cycle is set for 20 min with the sample 10 min at the cold compartment and then 10 min in the hot compartment.

www.manaraa.com

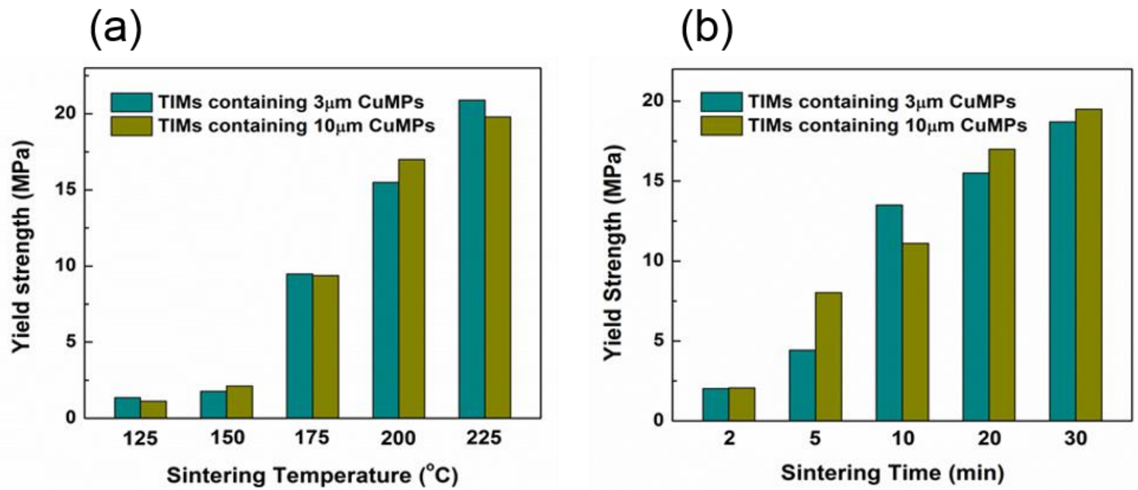

Figure 4-6 Ultimate strength comparisons of the TIM samples at different sintering temperatures for 20 min (a), and of the TIM samples at 200 ºC for different sintering times (b). The two compositions are AgNPs with 3 or 10 μm CuMPs with a mass ratio of 3:7. The higher the sintering temperature and the longer the sintering time, the higher the strength needed to take the samples to failure.

المنارة للاستشارات
www.manaraa.com

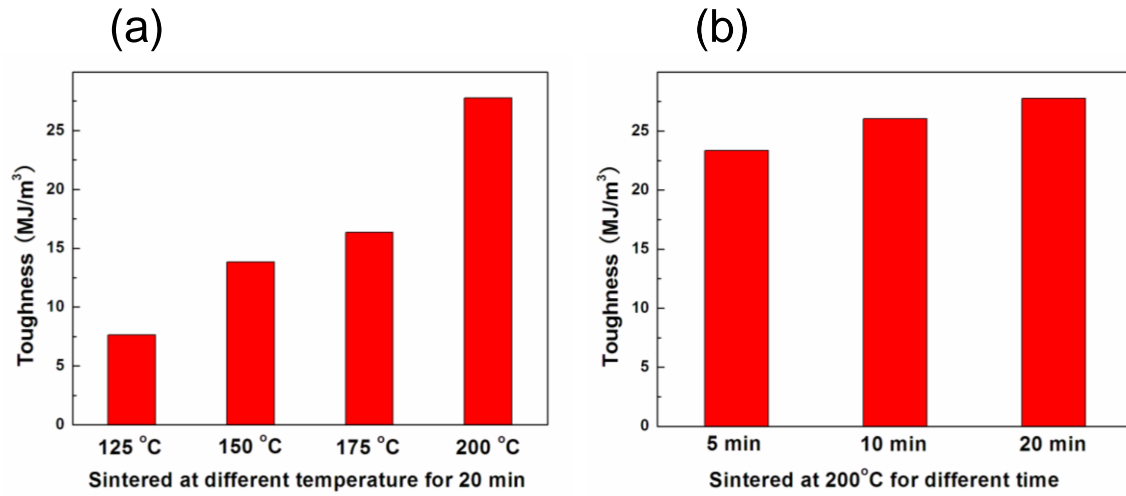

Figure 4-7 Comparison of the relative energy density of the TIM assemblies containing AgNPs and 10 μm CuMPs with a mass ratio of 3:7, sintered at different temperatures for 20 min (a), and at 200 ºC for different times (b). The higher sintering temperature and the longer sintering time makes the TIM assemblies tougher.

المنارة للاستشارات
www.manaraa.com

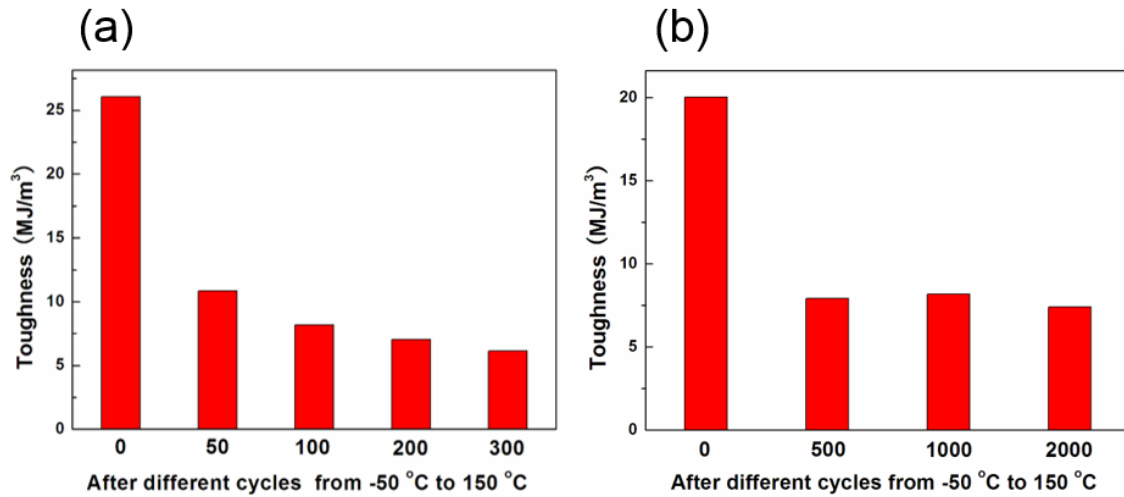

Figure 4-8 Comparison of the relative integral energy density of the TIM assemblies after different numbers of thermal cycles of -50 and 150 ºC. The TIM contains AgNPs and 10μm CuMPs (a) 3 μm CuMPs (b) with a mass ratio of 3:7, and both TIM samples were sintered at 200 ºC for 10 min. The relative integral energy density of the TIM sample decreases with the thermal cycling, and decreases more quickly at the first few thermal cycles.

المنارة للاستشارات
www.manaraa.com

(a)

(b)

Figure 4-9 SAM images for the TIM paste containing 10 μm CuMPs sintered at 200 ^oC for 20 min as prepared (a), and after 50 thermal cycles (b). After 50 thermal cycles, the internal structure of the TIM layer becomes decreasingly uneven, and some small voids disappear.

المنارة للاستشارات
www.manaraa.com

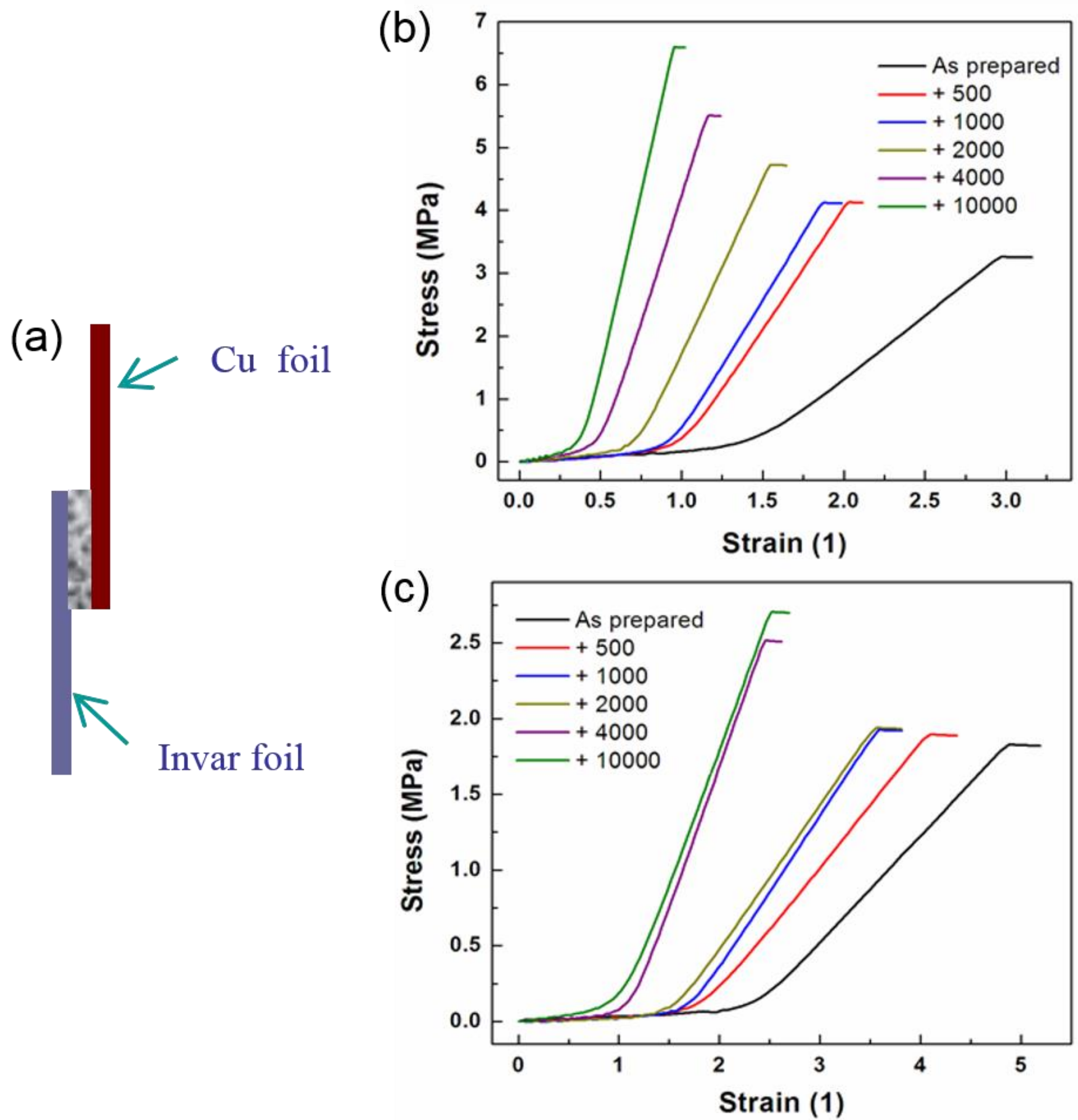

Figure 4-10 Schematics of the mismatched TIM assembly using Cu foil and invar foil as the two substrates (a), and the shear stress-strain curves for the thermo-mechanical performance of the mismatched TIM pastes containing 10 µm CuMPs (b) and 3 µm CuMPs (c). Both mismatched TIM pastes can survive 10000 thermal cycles between -50 and 150 ºC without failure.

المنارة للاستشارات
www.manaraa.com

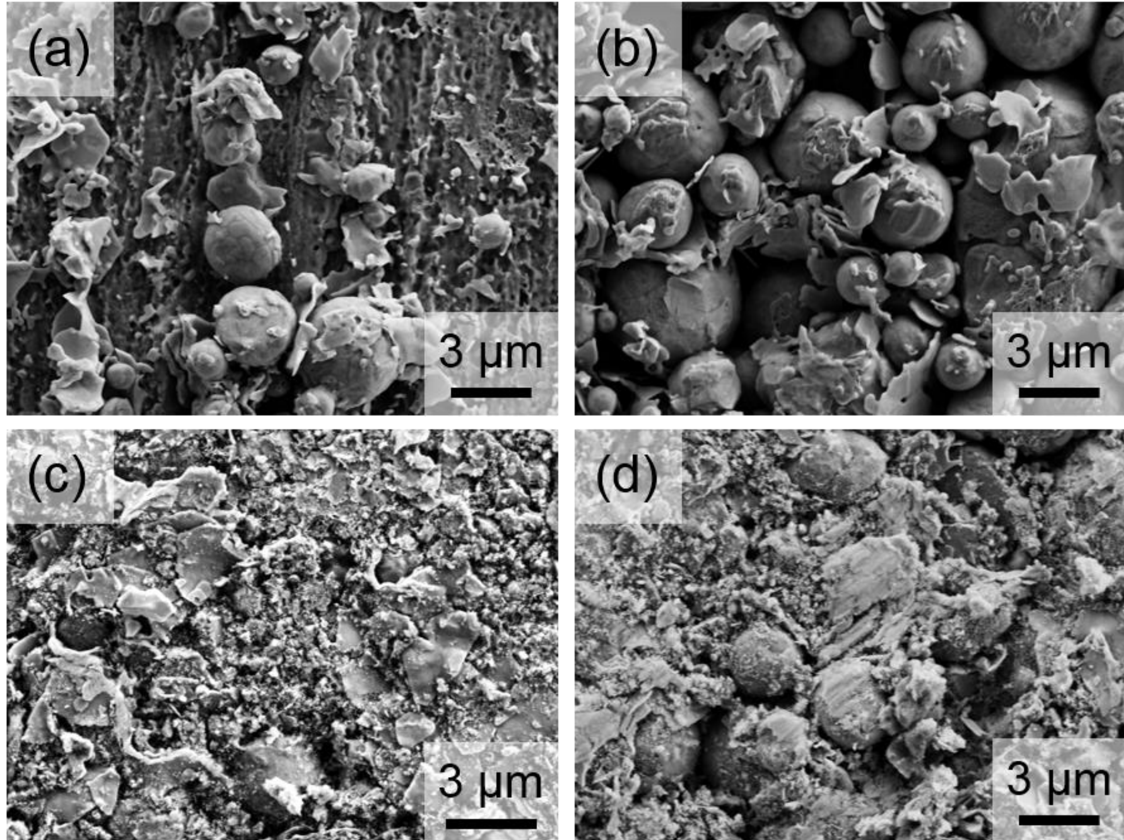

Figure 4-11 SEM investigation on the broken TIM sample sintered at 200 ºC for 20 min containing 3 μm CuMPs and AgNFs and AgNPs with a mass ratio of 6:2:2 (a) and (b), containing the same metal materials and 2 % polymer binder (c) and (d). The TIM sandwich samples were forced to separate with a strong external force. (a) and (c) are for the images of the areas without TIMs seen by naked eyes, (b) and (d) are for the images for the areas with most TIMs. The TIM assemblies fail either at the interfaces of Ag particles or between CuMPs and Ag particles.

المنارة للاستشارات
www.manaraa.com

Chapter 5 Thermal conductivity of the hybrid TIMs

5.1 Introduction

There have been developed various thermal conductivity (*k*) measurement techniques and different methods have their specific advantages and disadvantages as well as some particular requirements, such as the size and geometry of the specimen. Based on the properties of our TIM paste, steady state thermal measurement (ASTM D-5470) and flash diffusivity method (ASTM E1461) are chosen to determine the *k* of the materials.

The schematic of the measurement setup in figure 5-1 is an easy example to measure the *k* of the TIMs [233]. The apparatus basically consists of two meter-blocks, across which heat is transferred. The TIM is designed to be placed at the interface between the two blocks. Electric power supplies heat from the top of the setup, and an oil bath at the bottom is used as the cooling system to maintain the temperature gradient, thus generating the heat flux Q. Six thermal couples are fixed at the two copper rods to detect the temperatures at various locations. Through extrapolating from linear fit, T_T and T_B can be conducted, with a difference in the temperature drop of the two surfaces of TIMs. The *k* of the TIM can be calculated as below.

$$k = \frac{Q\, d}{A\, \Delta T} \qquad (5\text{-}1)$$

As the total resistance is directly recorded during the measurement, the *k* is actually determined according to the following equation.

المنارة للاستشارات
www.manaraa.com

$$R_{\text{TIM}} = \frac{\text{BLT}}{k_{\text{TIM}}} + R_{c1} + R_{c2} \quad (5\text{-}2)$$

R_{c1} and R_{c2} are two thermal contact resistances at the two interfaces between the TIMs and heat sink, TIMs and heat spreader (m^2K/W), BLT is the bond line thickness (m), k_{TIM} is the k of the TIMs (W/mK), as shown in figure 1-3.

Theoretically, the thickness versus thermal resistance linear fitting can be plotted as figure 5-2, where the slope is the bulk resistance (the reciprocal of the slope is the bulk *k*) and the intercept is the contact resistance [21, 234]. Here are some basic assumptions for the linear fitting plot.

(1) Heat conduction in one dimension (along Z direction) and no heat loss existing;

(2) The bulk TIM is uniform and liner fit to the thickness;

(3) Contact resistance is a constant.

The work mechanism of the flash diffusivity method is shown in figure 5-3. After the loading process, let the sample (a small, thin disc specimen) stable at a certain temperature T_0 at first. Then a pulse of a very short burst of energy (usually laser or other discharge source) is applied to the front face of the sample, leading to a temperature increase on the rear face, where a detector is used to record the temperature change as a function of time.

Figure 5-4 [108, 235] shows the ideal situation of the temperature curve (curve A) on the rear face where there is no heat loss, as well as the practical conditions (curves B and C) where involve heat loss. Curve A has no temperature decrease after reaching the maximum value at the rear face, while the temperature of curves B and C reduces gradually by different levels due to the heat loss. The typical commercial flash method is usually used to measure samples with a thickness of ~100 μm and above depending on the thermal

المنارة للاستشارات
www.manaraa.com

diffusivity of the sample. The thermal diffusivity is then determined from the specimen thickness, L, and the time required for the rear face temperature rise to a certain percentage of its maximum value.

For some transparent or translucent materials, the energy may pass through, during which gold or platinum [110] with high reflectivity and low emissivity can be employed to coat on the faces of the sample. However, a highly absorbant coating, such as graphite, must be used on the specimen to help increase the absorption and penetration of the laser beam to the sample. The two surfaces should be fully covered, but no thicker than 1 μm to avoid much contribution of the transmission time through the coating layer.

With reference to Chapter 1, Parker gave the calculation result of thermal diffusivity at the ideal case, as shown in equation 5-3, assuming the sample is isotropic and adiabatic, the flash pulse is instantaneous, and there is no heat loss during the measurement.

$$\alpha = 0.1388 \frac{L^2}{t_{1/2}} \quad (5\text{-}3)$$

α is thermal diffusivity, L is the thickness of the sample, $t_{1/2}$ is the time spent for the rear surface to reach half of the maximum temperature. Then k can be calculated according to the equation: $k = \alpha \rho C_p$, where ρ is density of the sample, which can be calculated from the weight and volume measuring of the bulk sandwich TIM samples; C_p is specific heat, which can be determined by the DSC (differential scanning calorimetry) method. DSC is a thermo-analytical technique in which the difference in the amount of heat required to increase the temperature of a sample and reference is measured as a function of temperature.

www.manaraa.com

5.2 Experiments

The steady state measurement equipment is shown in figure 5-5. The heat conduction rod is copper, having very good thermal conductance. An electric power provides heat source to the top of the copper block. The heat is conducted vertically downward through the TIM to the lower copper block, and then removed by an oil-cooled heat sink. The two copper rods are each 4-inch long, 1 inch by 1 inch square in cross section. The surfaces are kept parallel and aligned by two perpendicular mica plates attached to the sides of the copper rod. Four thermocouples are inserted into the certain places of the copper rods and two for each rod. The temperature gradient, obtained from 4 thermocouples, is linearly extrapolated to get the temperature at the two surfaces of the inserted TIM. An insulator box as guard heater is used to prevent the heat loss to the surrounding air from the input heater, by matching the temperature of the two "Guard heater reference thermocouples".

The air cylinder applies desired force controlled by the computer program in response to load cell signal with force upper limit of 200 lb. The best commercial thermal grease Shin-Etsu G751 is used as the instrument TIM measurements to fill the gap between the specimen and the two copper columns, and it is squeezed to different thicknesses (x-axis), depending on the squeezing force. The temperature range of this setup is 22 ^{o}C (room temperature) to 70 ^{o}C, and the loading force is usually set for 100 N during the measurement.

Figure 5-6 shows the cross sectional view of the measuring system with a sandwich sample [236]. There are many possible thermal contact resistances generated by the interfaces A-H. Since the interfaces A and H are far from the sample range, they are not

المنارة للاستشارات
www.manaraa.com

included into the calculated thermal resistance. Resistances at interfaces B, C, E and F can be offset from each other if a series of sample measurements are carried out using the same measurement conditions. The resistances at the interfaces D and E are measurable and they can be determined to be the thermal contact resistance between the substrates and the TIM layer after the linear fitting.

All the samples were prepared as 1' × 1' squares with two copper bulks as the substrates, and the total thickness of the sandwich samples was about 6.2 mm. The samples were assembled under the same compression conditions, with sintering temperature of 200 ^{o}C and pressure of about 7 MPa. For each composite of TIMs, four sandwich samples were chosen for the test with different TIM layer thicknesses ranging from 20 to 300 μm. One copper bulk with the same thickness of about 6.2 mm was carried out with the thermal test under the same conditions, which is treated as the blank contrast reference during the result analyses. More than five measurements were carried out for each sample. Those data acquisition and thermal resistance analysis was processed by Labview and Matlab.

The flash diffusivity setup in this study is the Flashline 2000 [237] from the Anter Corporation, which is consisted of 3 main parts: the electronic enclosure comprised of the electronic module and the high-speed xenon flash module, the computer fully configured and housing all necessary software for the instrument, including a high-speed data acquisition board, and the furnace assembly mounted on top of the electronic enclosure, which is shown in figure 5-6. The furnace assembly consists of a resistance-heated block which is the silver bottom part, the specimen holder located inside the furnace assembly, and the liquid nitrogen cryogenic detector assembly which is the red top part.

المنارة للاستشارات
www.manaraa.com

The specimen holder is a round shape with a diameter of 35 mm ($\sqrt{2}$ inch) and the thickness of 6 mm. The shape of specimen can be a round disk, a square or a rectangle plate, but cannot be larger than the maximum size of the holder. If the size of the specimen is smaller, adapter ring(s) are used to make it easy to insert into or remove from the holder, and are placed inside the counter-bore of the holder. The furnace seal window assembly is placed onto the furnace shell, and then the cryogenic detector assembly is rotated counter clockwise on top of this seal window. The instant energy source is the high-speed xenon pulse, generated from a high voltage (400~600 V) power supply. The measurement is carried out in air and the operating temperatures range from room temperature to 330 ^{o}C. The accuracy of the diffusivity measurement is 4 %, and the repeatability is 2 %.

In flash measurements, the substrates of the sandwich sample were still copper bulks in 1' × 1' squares, which is the same with those in the steady state method, as well under the same hot compression conditions. The difference is that the total thickness of the sandwich assemblies is about 4 mm, which is required by the flash diffusivity equipment. An attempt was made during the preparation of TIM assemblies is to keep all TIM layers with the same thickness to make the packing density as the only variance in the measurement. A graphite film was fully coated on the surfaces of the specimen to increase the absorption and penetration of the laser beam [108]. During the flash measurement, the voltage set for the flash pulse was 600 V, and 5 shots were set to collect data at room temperature during each test. For each sample, at least two tests were carried out to guarantee of the repeatability and accuracy of the collected data. Although it has been shown that the TIM layer thermal resistance has nothing to do with which side faces the

المنارة للاستشارات
www.manaraa.com

laser, all flash measurements are performed with the thinner copper side facing the laser beam in order to avoid variation.

The heat capacity of TIMs needed to calculate *k* was measured using differential scanning calorimetry (DSC, TA Instruments Q200) [238]. The alumina pan was used and sapphire was the standard reference due to its stability. Modulated mode and conventional MDSC test method was chosen for the measurement. The experiment was carried out in nitrogen atmosphere and the temperature was set from 10 ^{o}C to 70 ^{o}C by the ramp rate of 5 ^{o}C/min to get the specific heat of the TIMs at room temperature. The heat flow is continuously converted to heat capacity as shown in equation 5-4 and the reversing heat capacity is measured in the same experiment as described in equation 5-5.

$$C_p = \frac{\text{Heat flow}}{\text{Heating rate}} \times K \tag{5-4}$$

$$\text{Reversing } C_p = \frac{\text{Amplitude of modulated heat flow}}{\text{Amplitude of modulated heating rate}} \times K_{Cp} \tag{5-5}$$

where C_p is the specific heat capacity with the unit of J/g^{o}C, the unit for the heat flow is W/g, the heating rate is ^{o}C/min, and K and K_{Cp} are the dimensionless calibration constant. As MDSC separates the total heat flow into two parts, one part responding to heat rate and the other responding to the absolute temperature. What's more, it provides a check of the heat capacity as measured in the faster DSC signal-run, so the reversing C_p is more accurate and reproducible. Therefore, reversing C_p is used as the specific heat capacity of the measured TIMs during *k* calculation.

المنارة للاستشارات
www.manaraa.com

5.3 Results and discussions

The thermal resistance results collected from the steady state measurement of two kinds of TIMs are plotted in figure 5-8. For each kind of TIM, a series of samples were prepared and at least 5 measurements were processed for each sample to get the error bar in the plotting. Lines in the plot are least-square linear fitting yielding the bulk *k* from the slop and the contact resistance from intersects with the vertical coordinate axis. The final calculated results for the plotting in figure 5-8 from the steady state thermal measurement are shown in table 5-1. The all-metal binary TIMs (3 μm CuMPs: AgNFs = 6:4 by weight) have larger bulk *k* for being free of low conductivity polymers, whereas the ternary TIMs with polymer binders (3 μm CuMPs: AgNFs: AgNPs= 6:2:2, with 2 % P4VP by weight) have smaller interfacial contact resistance because of being more conformable to the interfacial roughness.

The *k* of the binary TIMs is 46 ± 6 W/mK, which remains the same after 100 cycles of -50 and 150 ^{o}C. The *k* of the ternary TIMs is 15 ± 1 W/mK, while their contact resistance reduces to 1.3×10^{-6} m^2K/W, which is much smaller than that of the binary composites, 3.6×10^{-6} m^2K/W. Data implys that addition of polymeric binders can reduce the contact resistance at the TIM/substrate interface [157]. Those thermal results change little after 100 thermal cycles between -50 and 150 ^{o}C. Both the *k* and contact resistance of the TIMs are much better than the best commercial thermal grease [17] and are comparable with the high-end solder TIMs [25, 27].

In the flash method, the 208 μm thick TIM layer contains metal component CuMPs, AgNFs and AgNPs of a mass ratio of 6:2:2 as well as 2 % polyvinylpyrrolidone (PVP) as

المنارة للاستشارات
www.manaraa.com

binder, while the other 3 TIM samples have the same composition of CuMPs and AgNFs at a mass ratio of 6:4 with addition of 2 % PVP by

weight. Table 5-2 lists the parameters and calculated results of the TIMs, including packing density, volume fractions of fillers and voids, specific heat, average half time from 10 shots of at least 2 independent measurements. The k is calculated using $k = \alpha \rho C_p$, where α is thermal diffusivity calculated by the Flashline Analysis software; C_p is specific heat capacity determined by the DSC; ρ is density calculated from the composition of the ingredients in the TIM during the preparation. The small variation of the specific heat capacity C_p due to different packing densities has minimal effect, and a common C_p value is used in the calculation of all samples with different packing densities. Some parameters of pure copper and silver materials possibly usable for calculations and comparisons are listed in table 5-3.

Table 5-2 shows that the increase of packing density of the TIMs is correlated with the increase of the filler volume fraction or reduction of the void volume fraction. Figure 5-9 shows the mass density ρ of TIMs as a function of the volume fraction of solid particles and the voids. The symbols are experimental data and lines through symbols are the best linear fitting, showing ρ increases linearly with the particle volume fraction, while inversely dependent on the void volume fraction. The higher the volume fraction of the filler particles, the lower the volume of the voids account for, which is reasonable with the physical truth.

However, the relationship of the k with the packing density is less trivial. Figure 5-10 shows k as a function of the volume fraction of the voids. It has high conductivity of

المنارة للاستشارات
www.manaraa.com

140 ± 8 W/mK at about 10 % voids by volume then drops to 86 ± 8 W/mK with 18 % voids, 64 ± 6 W/mK with 27 % voids, significantly to 44 ± 4 W/mK as voids fraction increases to more than 30 %. As shown in figure 5-10, the best fitting curve through the data symbols follows the law of power with a law exponent of -1.5, indicating the inverse correlation between thermal conductivity and the void volume fraction. The dependence of the *k* on the void volume fraction of the TIM is more complicated than expected [36, 125, 239, 240].

The dependence of *k* on the void volume fraction has been studied on many types of TIMs [6, 127, 128, 154], and numerous prediction models have been developed based on this relationship. Based on the literature review in Chapter 1, three simple models, the Maxwell Garnet (M-G) model (equation 5-6), the Bruggeman symmetric model (BSM, equation 5-7) and the Bruggeman asymmetric model (BAM, equation 5-8), have been chosen to plot with the matlab software, and compare to the experimental result from flash diffusivity. The expression of these models are given here again as follows.

$$\frac{k_e}{k_m} = \frac{[k_f(1+2\alpha)+2k_m]+2\upsilon_f[k_f(1-\alpha)-k_m]}{[k_f(1+2\alpha)+2k_m]-\upsilon_f[k_f(1-\alpha)-k_m]} \quad (5\text{-}6)$$

$$\alpha = \frac{2R_b k_m}{d} \quad (5\text{-}6a)$$

$$(1-\upsilon_f)\frac{k_m-k_e}{k_m+2k_e} + \upsilon_f\frac{k_f-k_e}{k_f+2k_e} = 0 \quad (5\text{-}7)$$

$$(1-\upsilon_f)^3 = (\frac{k_m}{k_e})^{(1+2\alpha)/(1-\alpha)} * [\frac{k_e-k_f(1-\alpha)}{k_m-k_f(1-\alpha)}]^{3/(1-\alpha)} \quad (5\text{-}8)$$

where k_e is the effective *k* of composites, k_m is the *k* of matrix, k_f is the *k* of particle filers and v_f is the volume fraction of the filers. α is the Biot number, which is a dimensionless parameter depending on the boundary interfacial thermal resistance between

المنارة للاستشارات
www.manaraa.com

particles and the matrix, R_b. During the models' plotting, v_f is regarded as the independent variable for k_e, and we assume that $k_m = 0.2$ W/mK, $k_f = k$ (Ag) = 406 W/mK (a little higher than k (Cu) = 385 W/mK), and $\alpha = 0$, which means neglecting the interface resistance between the matrix and the particles. Therefore, these 3 models are plotted in the semi-logarithm scale in figure 5-11 together with the experimental result from table 5-2.

As shown in figure 5-11, 3 models almost give the same predicting value when $v_f \leq 0.2$, after which, whereas their differences become more prominent with increasing v_f. At the $v_f = 0.5$, BSM predicts k_e ~100 W/mK, about two orders of magnitude higher than those of BAM and M-G models. Combining the above experimental data shown in the figure, both M-G model and BAM models underestimate the effective k of the TIMs, even though assuming $R_b = 0$ ($\alpha = 0$). As M-G model is typically applied to TIMs of $v_f < 0.25$, it is reasonable that it predicts k far lower than the experimental data. BAM is widely used to simulate the effective k of polymeric TIMs and takes the interface resistance into consideration. However, it is not applicable to the situation in this study. BSM overestimates the effective thermal conductivity of the nanocomposite TIMs due partially to omitting the interface resistance R_b. It is consistent with the theory that that the effective thermal conductivity of porous materials is bounded between the Maxwell and the BSM equation [155].

Combining with the previous SEM images of the nanostructured networks in the sintered TIM system, we can assume that two effective symmetric components exist. The metallic network with higher thermal conductivity can be regarded as the fillers, while the network of voids together with the polymer binders, if any, can be treated as the matrix. In this case, BSM is used to predict the effective thermal conductivity of the nanocomposite

المنارة للاستشارات
www.manaraa.com

TIMs. If taking the effects of interfacial resistance between metal particles as well as the geometric effect into account toward an effective overall k_f, the best fitting to the experimental data, shown as the cyan shadow centered with the dotted red curve, yields an effective k_f = 100 to 220 W/mK. Further data analyses indicate that the effective k_f increases much faster than the filler volume fraction. This apparently stronger dependence of k_f on filler volume fraction implies the improvement of network structure quality in the denser packed TIM system. The structure of the hybrid composites in this study is more complex than that presented in the ideal two-phase model. Further investigations are needed to gain a better understanding of the resin-free nanocomposite TIM system.

5.4 Conclusion

Both steady state thermal and flash diffusivity methods were carried out for the k measurement of the nanocomposite TIM. The results show that the k of TIMs has been improved to a range of 15~140 W/mK, and the interface contact resistance can be as low as $1.3*10^{-6}$ m^2K/W, which is better than the current best commercial grease and can be a competitive product of the high-end solder TIMs. The comparison of several theoretical models and the experimental data indicates that the unique nanostructure of TIM system matches the symmetric model, and the apparently stronger dependence of k_f on v_f implies the improvement of network structure quality in denser packing. The nanocomposite TIM system in this study is more complex than the ideal two phases.

المنارة للاستشارات
www.manaraa.com

Table 5-1 Thermal results from steady state measurement in figure 5-8

TIM composite	k (W/mK)	Contact resistance (m^2K/W)
60M 40F	46 ± 6	$3.6 \pm 1.0*10^{-6}$
59M 19.5F 19.5N 2P	15 ± 1	$1.3 \pm 0.2*10^{-6}$

Notation for table 5-1 & 5-2: in order to simplify some expressions in the table, each composite of TIMs can be abbreviated to one letter, such as M = CuMPs, F = AgNFs, N = AgNPs, P = Polymer binder.

المنارة للاستشارات
www.manaraa.com

Table 5-2 Parameters and *k* result from diffusivity method

Sample label	59M 19.5F 19.5N 2P	59M 39F 2P		
Sample No.	1	2	3	4
Thickness (μm)	208	150	156	146
Density (g/cm^3)	5.70±0.28	6.13±0.31	6.85±0.34	7.19±0.36
Filler volume fraction (%)	58.8±3.5	63.1±3.8	70.5±4.2	77.2±4.6
Void volume fraction (%)	32.3±1.9	26.6±1.6	17.9±1.1	10.2±0.6
C_p (J/g K)	0.432±0.004			
Ave. $t_{1/2}$ (s)	0.0285±0.0006	0.0238±0.0005	0.0233±0.0007	0.0217±0.0007
Diffusivity (cm^2/s)	0.177±0.012	0.240±0.016	0.289±0.021	0.452±0.025
k (W/mK)	44±4	64±6	86±8	140±8

Table 5-3 Parameters for thermal diffusivity calculation

	Copper	Silver
α (cm^2/s)	1.11	1.65
Density (g/cm3)	8.96	10.49
Cp (J/g K)	0.385	0.223

المنارة للاستشارات
www.manaraa.com

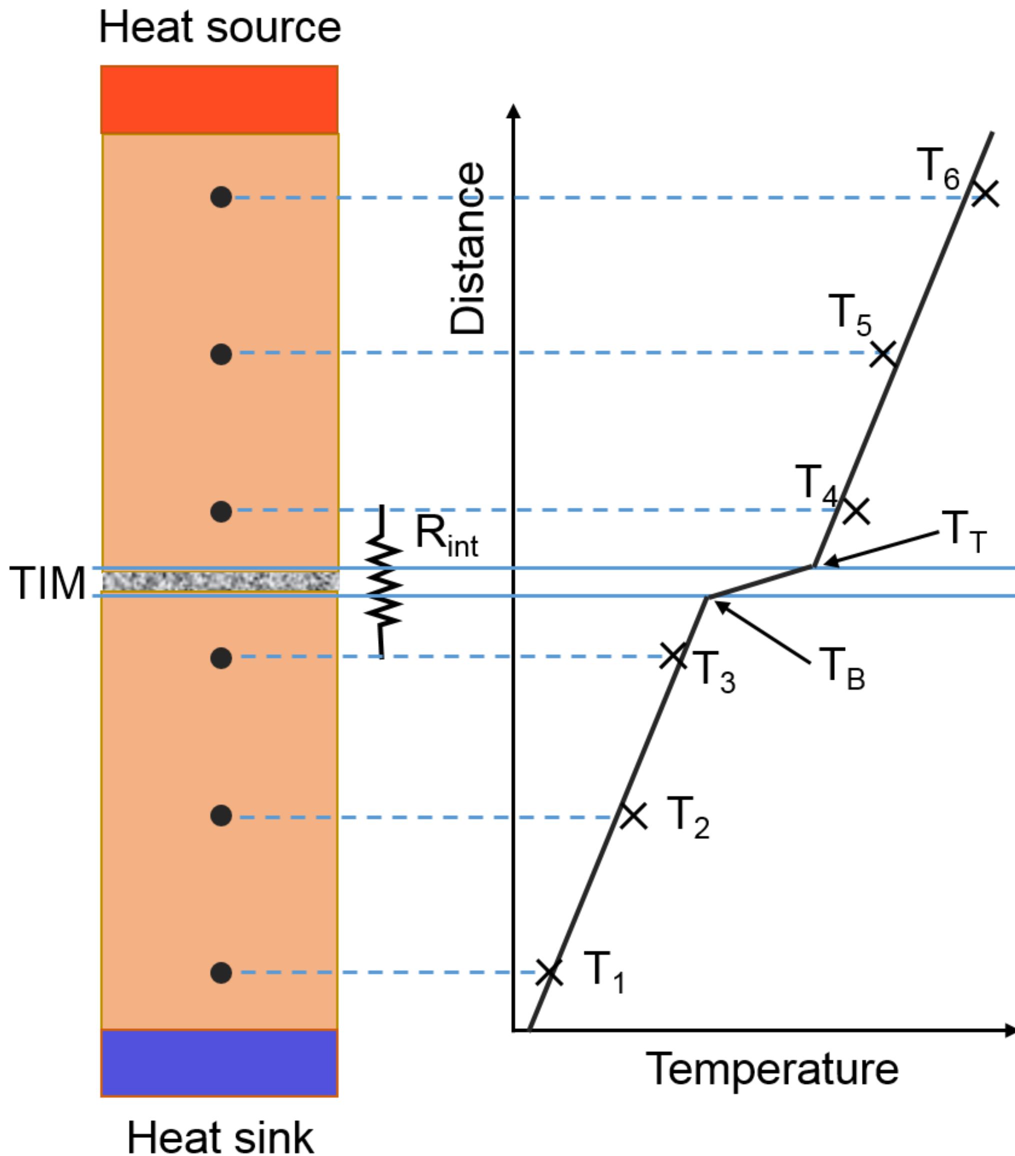

Figure 5-1 Schematic illustration for the steady state thermal measurement setup The TIM is placed in a steady flow of heat established in a rod by a steady heat source and a steady heat sink (cooling system). Six temperatures were measured along the rod, and the temperature drop across the TIM can be estimated through fitting the 6 measured temperatures. The temperature gradient in the rod and the known *k* of the rod give the heat flow in the rod. The ratio of ΔT to heat flux Q is the unit-area thermal contact resistance R" of the TIM.

المنارة للاستشارات
www.manaraa.com

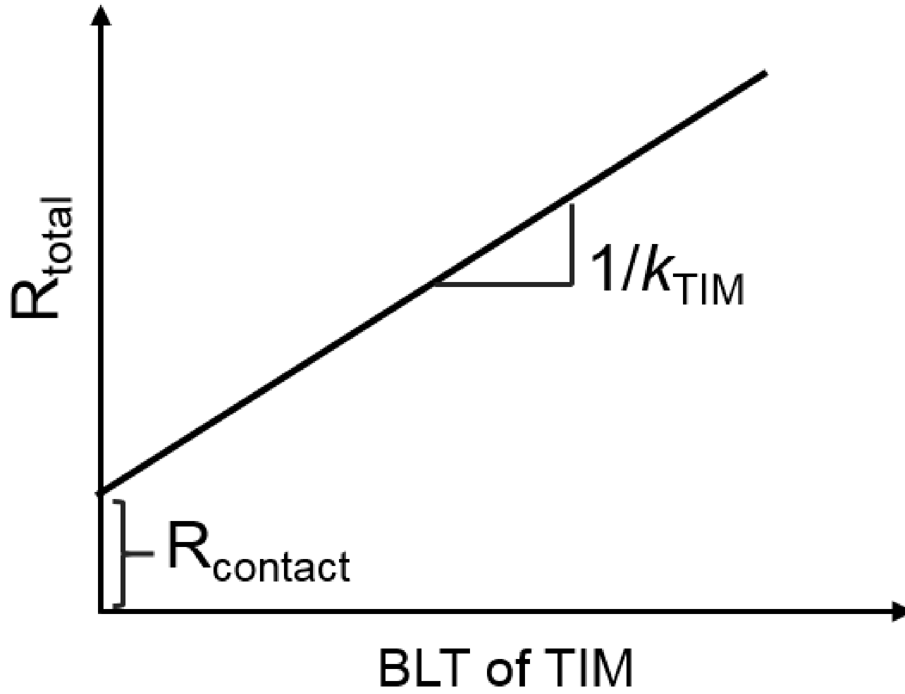

Figure 5-2 Theoretical plot of effective thermal resistance vs. BLT, where the reciprocal of the linear slope is the effective *k* of the TIM, and the y intercept is the interface thermal contact resistance.

المنارة للاستشارات
www.manaraa.com

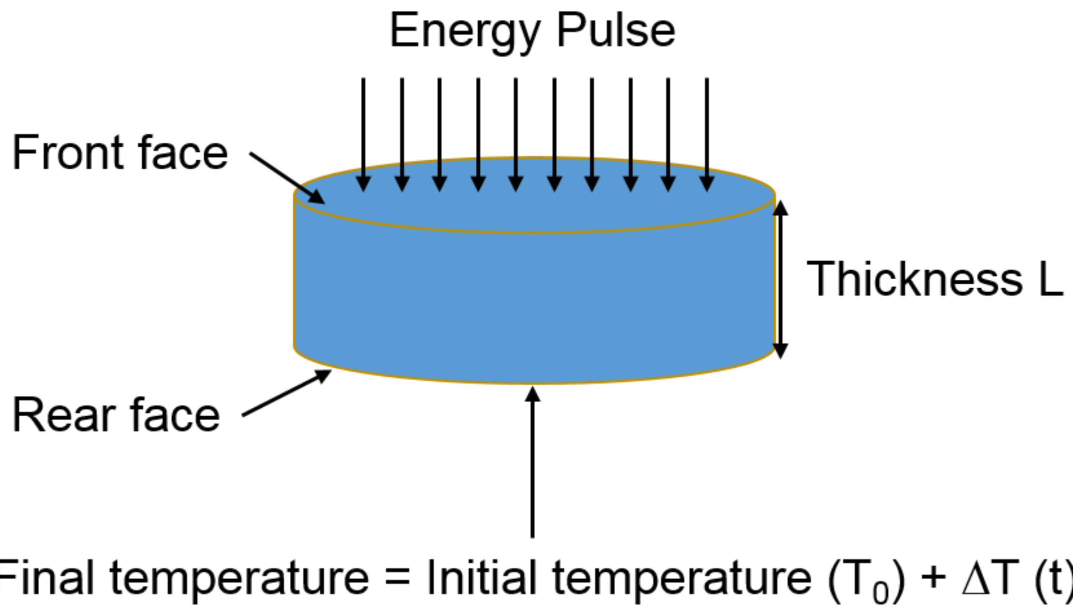

Figure 5-3 Measuring principle of flash diffusivity method. An energy pulse is applied to the front face of the planar-shaped sample with a thickness of L and an initial temperature T_0. A detector measures the temperature rise at the rear face which is a function of time. Thermal diffusivity of the sample is obtained by analyzing the dynamic response of the rear face temperature rise.

المنارة للاستشارات
www.manaraa.com

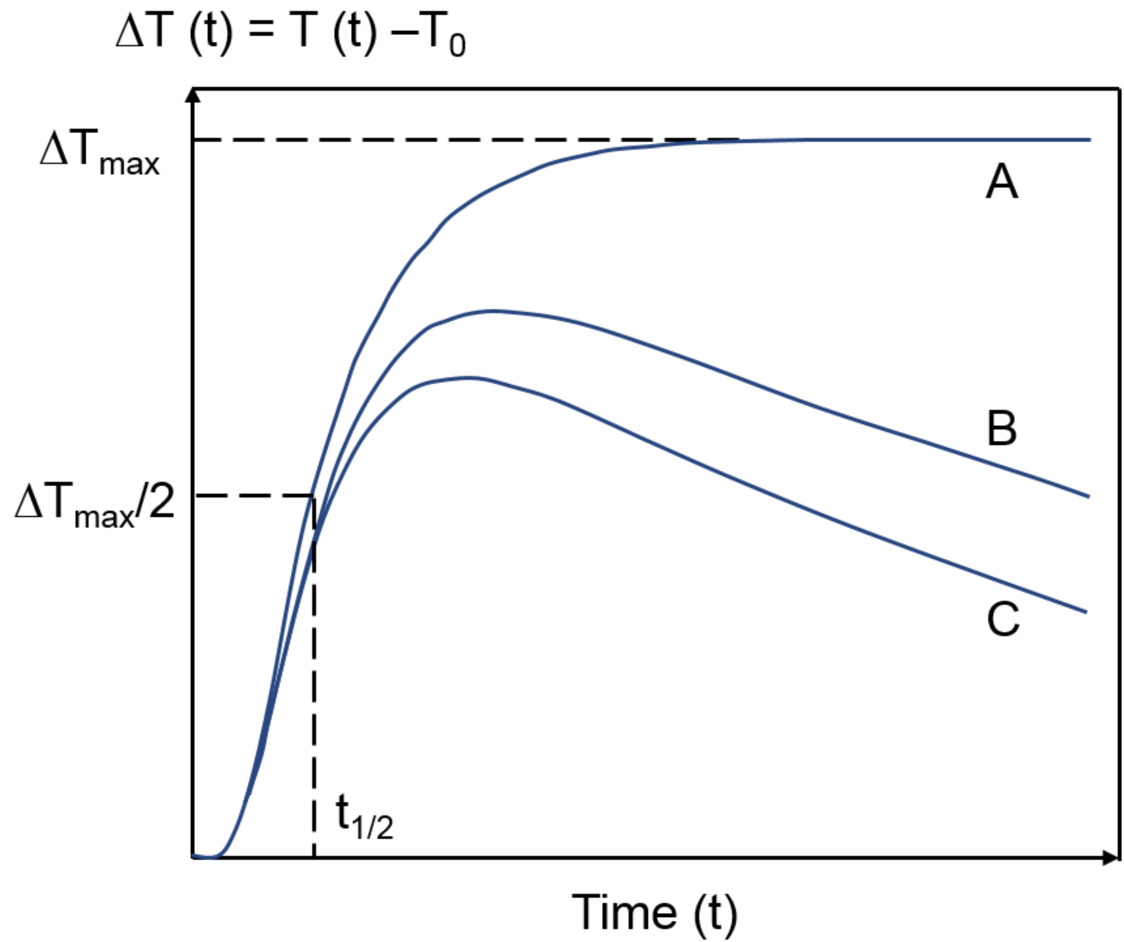

Figure 5-4 Temperature change curves under different conditions measured on the rear side of the specimen. If there is no heat loss, the temperature on the rear face will rise to maximum and keep that value indefinitely (Curve A). However, with the heat loss involved, the temperature of the rear face decreases to varying extents after reaching a maximal value (Curves B and C).

للاستشارات المنارة
www.manaraa.com

Figure 5-5 Schematic of steady state method setup, where an electric power provides heat from the top of the setup, and an oil bath at the bottom functions as the cooling system, thus generating a steady temperature gradient. Four thermocouples are used to detect the temperature located at certain places of the copper rods, and an insulator box is added to reduce the heat loss during the measurements.

المنارة للاستشارات
www.manaraa.com

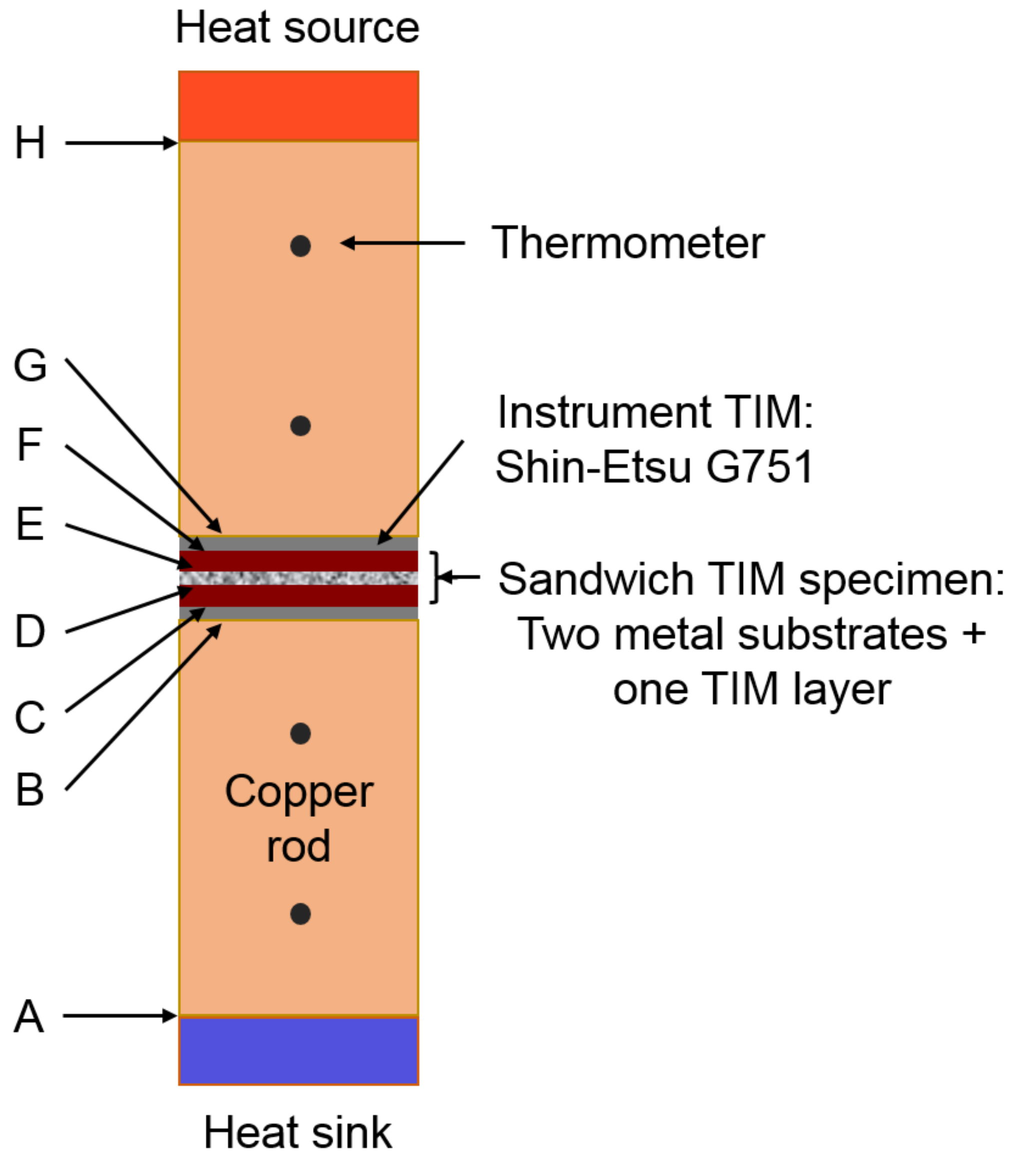

Figure 5-6 1D sectional perspectives of steady state measurement with a sandwich TIM where the possible resistances at the interfaces A and H will not be included into the calculated thermal resistance. Resistances at interfaces B, C, E and F can be offset after a series of sample measurements while the resistances at the interfaces D and E will be measured as the interface contact resistance between the substrates and the TIM layer.

للاستشارات المنارة
www.manaraa.com

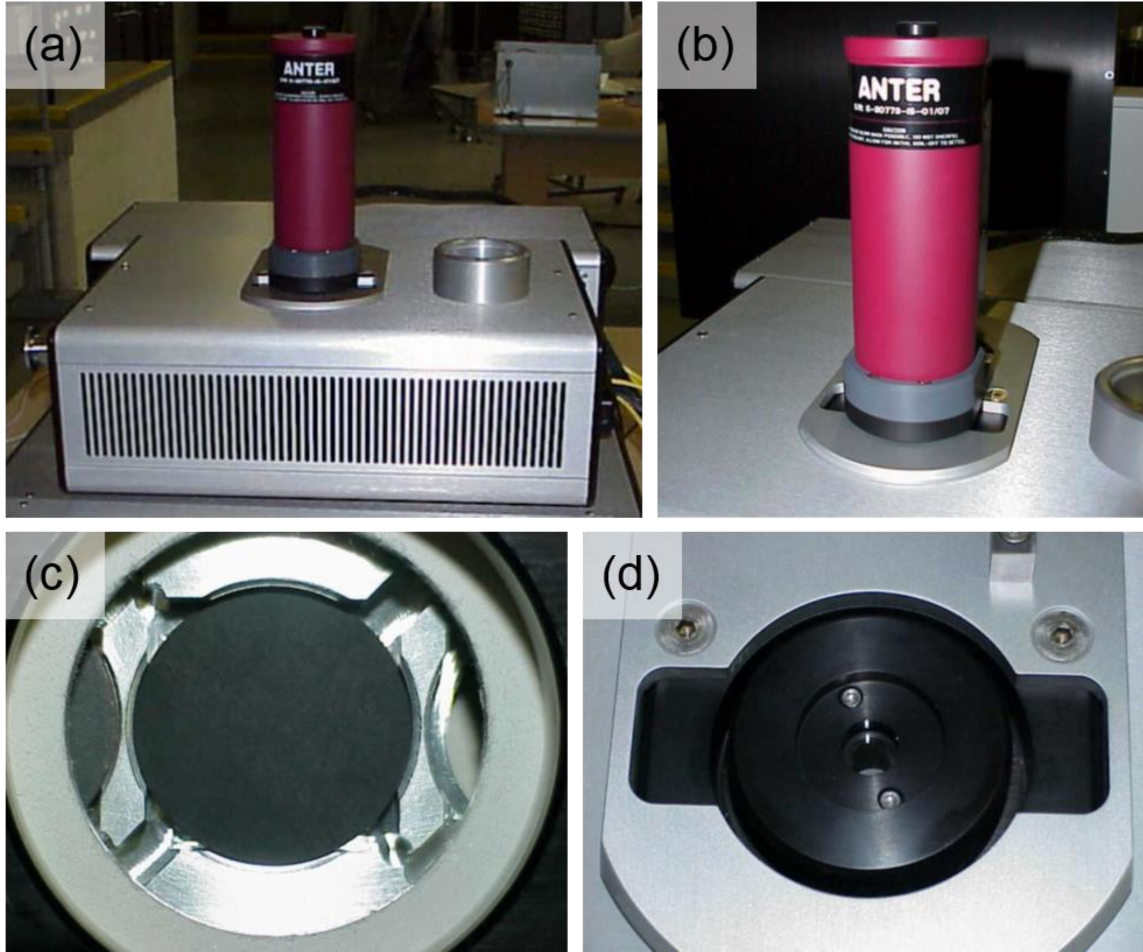

Figure 5-7 The furnace assembly (a) of the flash diffusivity method and parts of it: the liquid nitrogen cryogenic detector (b), the specimen holder (c) and the furnace seal window (d). The specimen holder is located inside of the furnace and the seal window is placed onto the holder, with the detector on top.

المنارة للاستشارات
www.manaraa.com

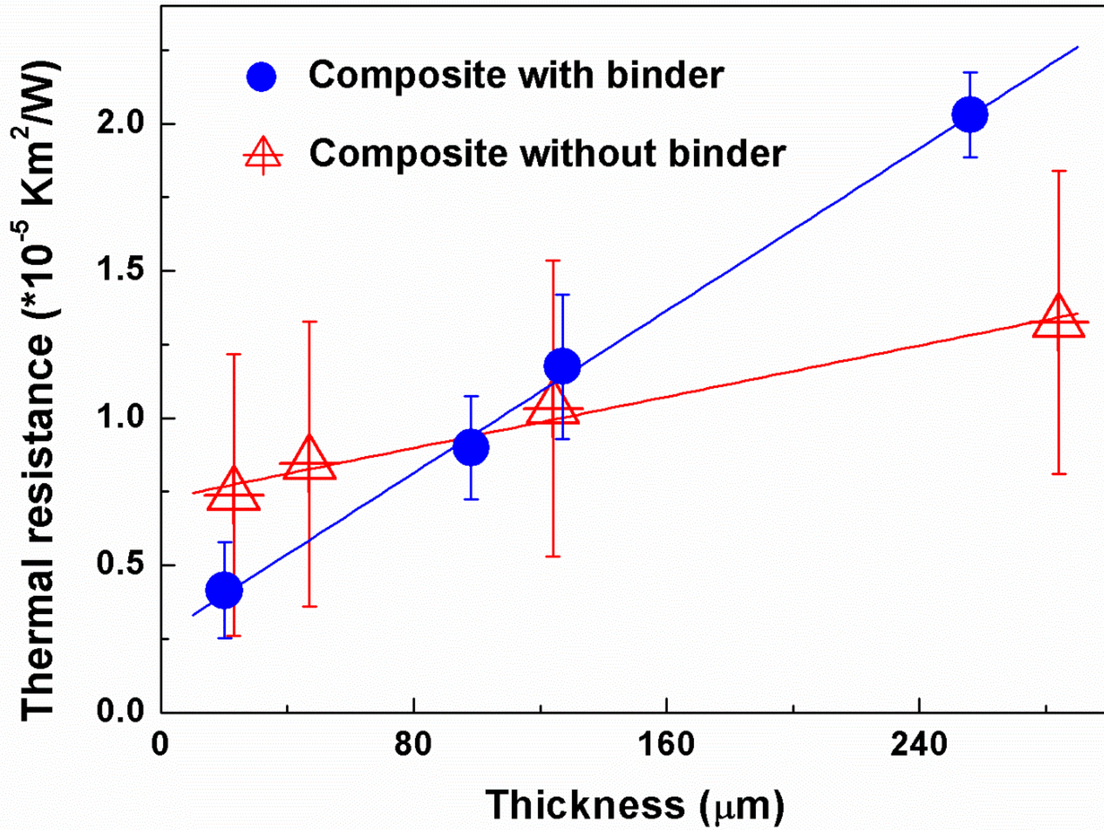

Figure 5-8 The thermal resistance as a function of the thickness of the TIMs for 3 μm CuMPs: AgNFs = 6:4 by weight as prepared (the red triangle symbols), and of TIMs for 3 μm CuMPs: AgNFs: AgNPs= 6:2:2, with 2 % P4VP by weight (the blue dot symbols). The symbols are experimental data and both lines through the symbols are the best linear fitting. After plotting, the intercept is the contact resistance value of the two interfaces with two same substrates, while the reciprocal of the slope is the *k*. The result is summarized in table 5-1.

المنارة للاستشارات
www.manaraa.com

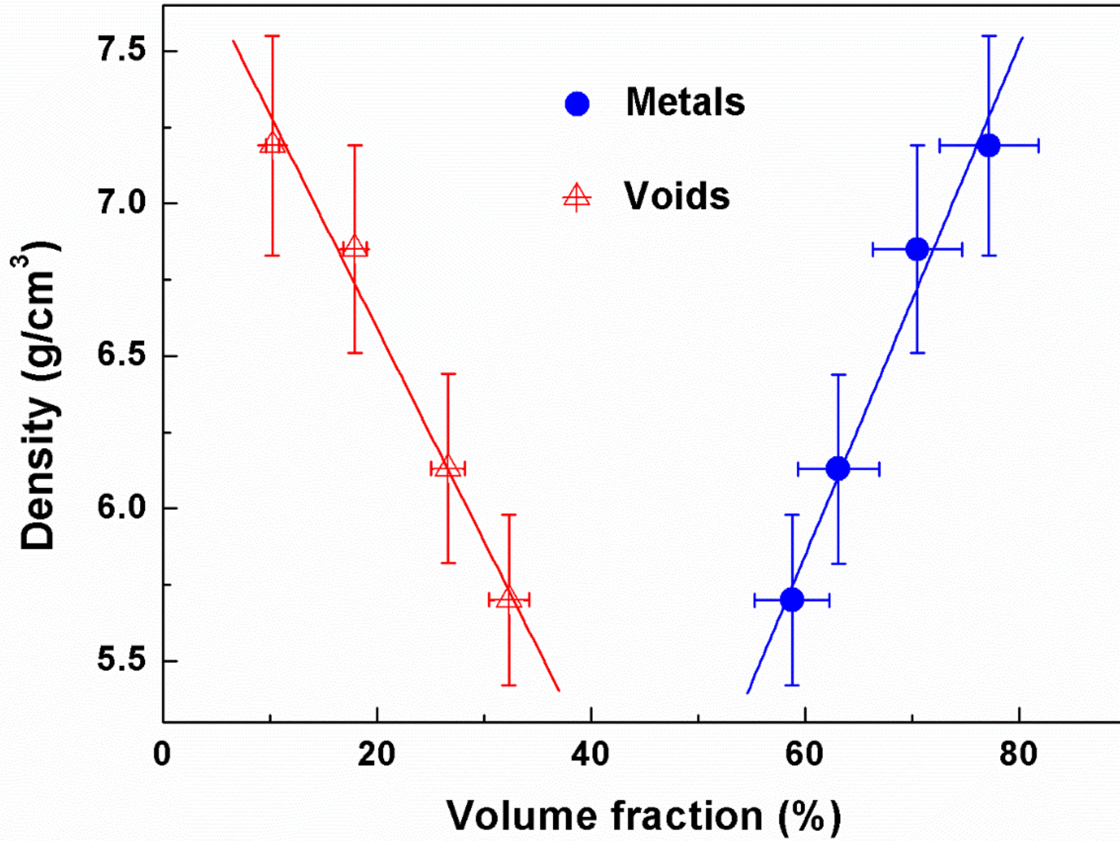

Figure 5-9 The volume fraction of fillers and voids with the change of packing density of TIMs. In the figure, both lines through the symbols are the best linear fitting. With the increasing packing density of the TIMs, the filler volume fraction increases as the void volume fraction decreases.

المنارة للاستشارات
www.manaraa.com

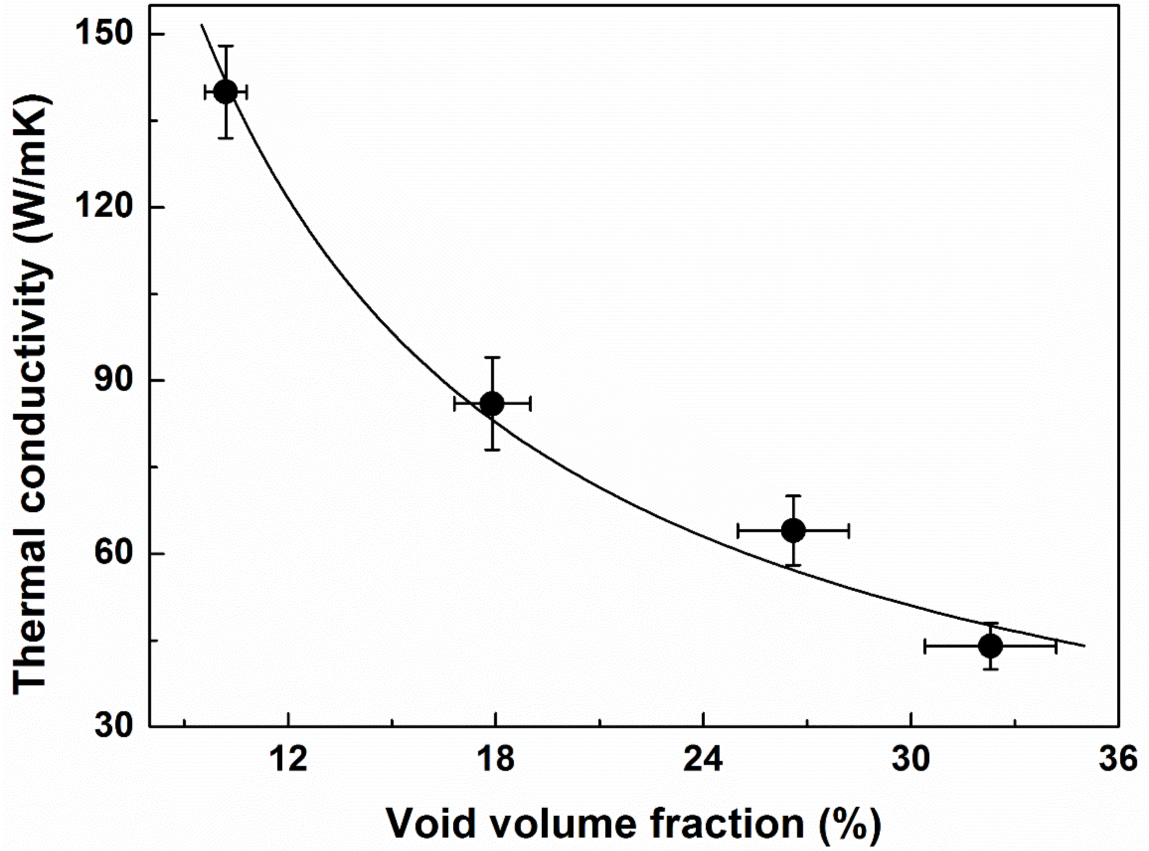

Figure 5-10 The *k* vs. void volume fraction of the TIMs. The lower the viodage, the higher the k. The *k* increases with increasing packing density. The line through the symbols is the best fitting of power-law with the exponent of -1.5, indicating rather complicated correlations between *k* and the void volume fraction.

المنارة للاستشارات
www.manaraa.com

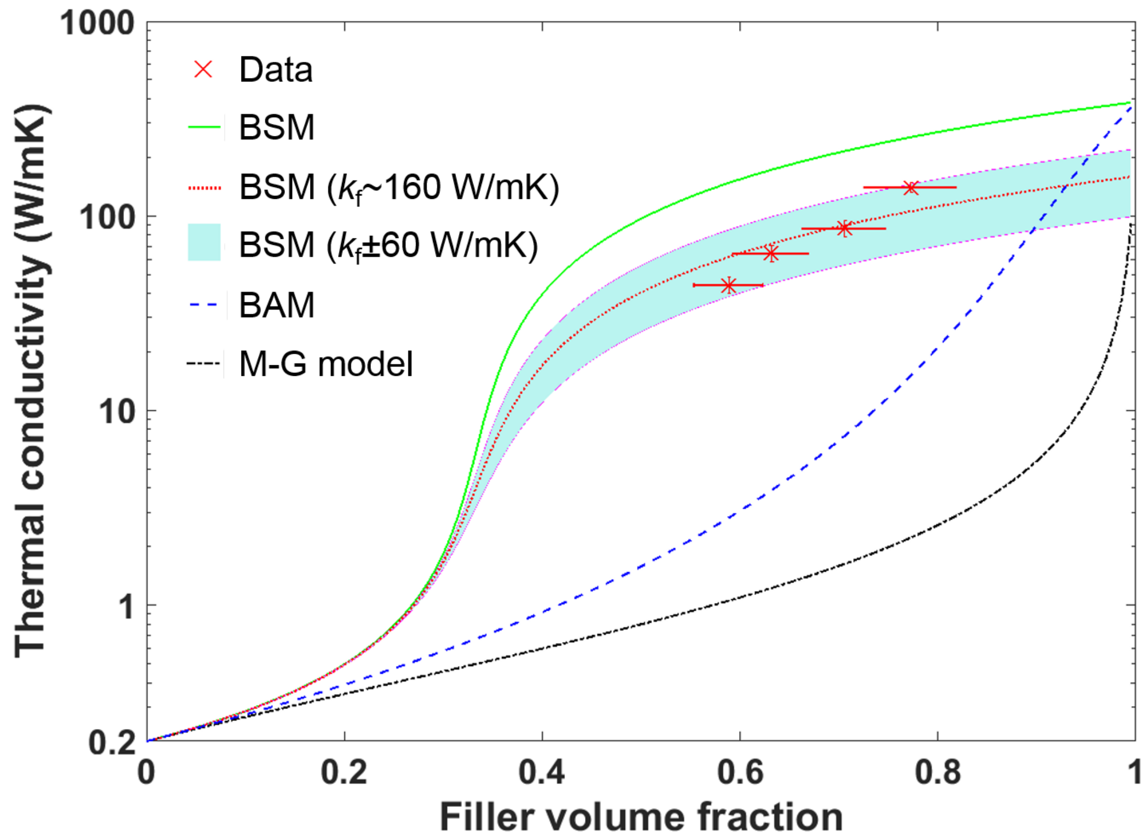

Figure 5-11 Comparison of three analytical models and experimental data, where the symbols are experimental data from this study and curves are model predictions. Three models have similar prediction for low volume filling, i.e., at $v_f < 0.2$, above which their differences become prominent. BSM overestimates the k while both M-G model and BAM models underestimate the effective k of the TIMs, even assuming $\alpha = 0$ ($R_b = 0$). The cyan shadow centered at the dotted red curve is modified BSM calculation yielding an effective overall bulk k_f ~100-220 W/mK for the best match with the experimental data.

المنارة للاستشارات
www.manaraa.com

Chapter 6 Conclusion and future work

6.1 Conclusion

There is a great demand for TIMs with high *k*, low thermal interface contact resistance and low cost in the current electronic packaging market. In this dissertation, a new resin-free nanocomposite TIM integrating silver nanoparticles (AgNPs), Ag nanoflakes (AgNFs) and copper micro-particles (CuMPs) has been developed. The nanocomposite TIMs optimize both the bulk and interfacial thermal performances; CuMPs with a particle size of 1~10 μm provide the backbone of the metallic network upon sintering and offer the assurance of high bulk thermal conductivity (*k*), while AgNPs with a diameter of 3~8 nm and 10 nm thick AgNFs provide the flexibility and the bondage in interfacial engineering. The TIM assemblies have been prepared through hot compression at temperatures of 125~225 ^{o}C for 5~20 min under a pressure of ~7 MPa. Morphological and compositional analyses have shown percolated network structures formed through strong metallic bonds of fused AgNPs and AgNFs with CuMPs and the substrates in TIMs, resulting in good mechanical and thermal performance and excellent thermo-mechanical reliability.

Flash diffusivity and steady state thermal measurements have shown *k* of nanocomposite TIMs in the range of 15~140 W/mK, and the contact resistance as low as 1.3×10^{-6} m^2K/W, comparable to high-end TIMs. Using analytical models, the role of void

المنارة للاستشارات
www.manaraa.com

volume fractions and interfacial resistance in the hybrid composites on thermal conductivity has been assessed. Data shows the network structure quality is greatly improved with denser particle filling and the network structure of the novel nanocomposite TIM system favors the symmetric model. Shear and tensile tests have shown that both bond strength and relative energy density of TIMs increases with higher sintering temperature and longer sintering duration time. The failure analyses show that the fracture mechanism of the TIM assemblies is totally cohesive failure. The thermo-mechanical reliability of hybrid TIMs bonding solid substrates with their CTE differences exceeding 15 ppm/^{o}C has been tested. The mismatched TIM assemblies have gone through more than 10^4 cycles of thermal shocks between -50 and 150 ^{o}C without failure. This study has shown the promises of the nanocomposite TIMs for broader applications of thermal, mechanical and thermomechanical performance in electronics packaging.

6.2 Future work

Exciting opportunities and challenges coexist in taking the nanocomposite TIMs developed in this study to become a commercially viable technology.

(1) The fundamental and in-depth understanding of thermal and mechanical properties of hybrid TIMs remains to be gained. This study has shown the critical importance of continuous network structure in high thermal and mechanical performances, yet a detailed relationship with processing conditions and microstructures is still lacking. Systematic fundamental studies can be carried out to fully understand the effect of the topological structure of the continuous network on the thermal transport as well as

المنارة للاستشارات
www.manaraa.com

mechanical deformation. Furthermore, the metallic network is not uniform in composition, but rather joined together with multiple components with interfaces and interphases. Both the topological structure and composition distribution are strongly dependent on the starting ingredients and processing conditions. The comprehensive knowledge of the materials, processing, structure, property and performance relationship will form the foundation of utilizing full potential of novel hybrid nanocomposite TIMs.

(2) On the basis of fundamental understandings and theoretical predictions, much work is needed to explore the practical routine of realizing technologically viable TIMs. Broader ranges of materials selection with various elemental compositions and thermal, mechanical and chemical natures will need to be investigated to address the applications of various needs. In addition, the effect of the dimensionality of the starting materials in continuous forms, i.e., from 0 to 2D (nanoparticles, nanowires and nanoflakes) with fractal dimensions, and accordingly the size, size distribution, shape, shape dispersion and their combinations, will need to be explored. Furthermore, the important role of surface modification and the organic binder needs to be optimized to meet the processing requirements. Various processing conditions compatible with the application requirements will be studied.

(3) There exist many tradeoffs in the complex nanocomposite TIM systems, such as between processibility and properties, performance and reliability, bulk and interfaces, thermal and mechanical, etc. Parametric mapping and database building is demanded for addressing specific technology needs.

المنارة للاستشارات
www.manaraa.com

References

[1] G. E. Moore, "Cramming more components onto integrated circuits," *Electronics,* vol. 38, no. 8, 19 April, 1965.

[2] G. E. Moore, "Cramming more components onto integrated circuits," *Proceedings of the IEEE,* vol. 86, no. 1, pp. 82-85, January, 1998.

[3] R. Mahajan, C. P. Chiu, and G. Chrysler, "Cooling a microprocessor chip," *Proceedings of the IEEE,* vol. 94, no. 8, pp. 1476-1486, August, 2006.

[4] A. Shakouri, "Nanoscale thermal transport and microrefrigerators on a chip," *Proceedings of the IEEE,* vol. 94, no. 8, pp. 1613-1638, August, 2006.

[5] R. Gordon, *Thermal interface mateirals 2016-2026: Status, opportunities, market forecast*, 2015.

[6] R. Prasher, "Thermal interface materials: Historical perspective, status, and future directions," *Proceedings of the IEEE,* vol. 94, no. 8, pp. 1571-1586, August, 2006.

[7] J. P. Gwinn, and R. L. Webb, "Performance and testing of thermal interface materials," *Microelectronics Journal,* vol. 34, no. 3, pp. 215-222, 2003.

[8] B. Guenin, "Packaging challenges for high heat flux devices," *Electronics Cooling,* vol. 12, 1 August, 2006.

[9] D. Blazej, "Thermal interface materials," *Electronics Cooling,* vol. 9, no. 4, 1 November, 2003.

[10] R. Mahajan, C. P. Chiu, and R. Prasher, "Thermal interface materials: A brief review of design characteristics and materials," *Electronics Cooling,* vol. 10, no. 1, February, 2004.

[11] F. Sarvar, D. C. Whalley, and P. P. Conway, "Thermal interface materials - A review of the state of the art," in 1st Electronics System Integration Technology Conference, Dresden, Germany, 2006, pp. 1292-1302.

[12] *Thermal interface materials for electronics cooling*, Parker Hannifin Corporation, Woburn, MA, 2014.

المنارة للاستشارات
www.manaraa.com

[13] D. D. L. Chung, “Thermal interface materials,” *Journal of Materials Engineering and Performance,* vol. 10, no. 1, pp. 56-59, February, 2001.

[14] K. C. Otiaba, N. N. Ekere, R. S. Bhatti, S. Mallik, M. O. Alam, and E. H. Amalu, “Thermal interface materials for automotive electronic control unit: Trends, technology and R&D challenges,” *Microelectronics Reliability,* vol. 51, no. 12, pp. 2031-2043, 2011.

[15] R. C. Getty, and R. E. Tatro, “Spacecraft thermal joint conduction,” in 2nd Thermophysics Specialist Conference, San Diego, CA, 1967, pp. 67-316.

[16] M. Y. Razzaq, M. Anhalt, L. Frormann, and B. Weidenfeller, “Thermal, electrical and magnetic studies of magnetite filled polyurethane shape memory polymers,” *Materials Science and Engineering: A,* vol. 444, no. 1-2, pp. 227-235, 2007.

[17] *Silicone grease solutions for your thermal interface needs*, Dow Corning, Midland, MI, 2011.

[18] C. P. Chiu, B. Chandran, M. Mello, and K. Kelley, “An accelerated reliability test method to predict thermal grease pump-out in flip-chip applications,” in 51st Electronic Components and Technology Conference, Orlando, FL, 2001.

[19] A. Sharma, V. V. Tyagi, C. R. Chen, and D. Buddhi, “Review on thermal energy storage with phase change materials and applications,” *Renewable and Sustainable Energy Reviews,* vol. 13, no. 2, pp. 318-345, 2009.

[20] M. B. Stern, G. Jhoty, D. Kearns, and B. Ong, “Measurements of mechanical coupling of non-curing high performance thermal interface materials,” in 22nd IEEE Semiconductor Thermal Measurement and Management Symposium, Dallas, TX, 2006, pp. 37.

[21] S. Narumanchi, M. Mihalic, K. Kelly, and G. Eesley, “Thermal interface materials for power electronics applications,” in 11th Intersociety Conference on Thermal and Thermomechanical Phenomena in Electronic Systems, ITHERM 2008, Orlando, FL, 2008, pp. 1-10.

[22] K. N. Tu, A. M. Gusak, and M. Li, “Physics and materials challenges for lead-free solders,” *Journal of Applied Physics,* vol. 93, no. 3, pp. 1335-1353, 1 February, 2003.

[23] A. K. Gain, and L. C. Zhang, “Interfacial microstructure, wettability and material properties of nickel (Ni) nanoparticle doped tin-bismuth-silver (Sn-Bi-Ag) solder on copper (Cu) substrate,” *Journal of Materials Science: Materials in Electronics,* vol. 27, no. 4, pp. 3982-3994, April, 2016.

المنارة للاستشارات
www.manaraa.com

[24] H. T. Ma, and J. C. Suhling, “A review of mechanical properties of lead-free solders for electronic packaging,” *Journal of Materials Science,* vol. 44, no. 5, pp. 1141-1158, 2009.

[25] *Metal thermal interface materials*, Indium Corporation.

[26] K. Suganuma, S. J. Kim, and K. S. Kim, “High-temperature lead-free solders: Properties and possibilities,” *The Journal of the Minerals, Metals & Materials Society,* vol. 61, no. 1, pp. 64-71, January, 2009.

[27] T. Siewert, S. Liu, D. R. Smith, and J. C. Madeni, "Database for solder properties with emphasis on new lead-free solders, Release 4.0," National Institute of Standards and Technology & Colorado School of Mines, 2002.

[28] C. Deppisch, T. Fitzgerald, A. Raman, F. Hua, C. Zhang, P. Liu, and M. Miller, “The material optimization and reliability characterization of an indium-solder thermal interface material for CPU packaging,” *The Journal of the Minerals, Metals & Materials Society,* vol. 58, no. 6, pp. 67-74, June, 2006.

[29] I. Dutta, R. Raj, P. Kumar, T. Chen, C. M. Nagaraj, J. Liu, M. Renavikar, and V. Wakharkar, “Liquid phase sintered solders with indium as minority phase for next generation thermal interface material applications,” *Journal of Electronic Materials,* vol. 38, no. 12, pp. 2735-2745, 2009.

[30] R. M. German, P. Suri, and S. J. Park, “Review: Liquid phase sintering,” *Journal of Materials Science,* vol. 44, no. 1, pp. 1-39, 2009.

[31] M. Pharr, K. J. Zhao, Z. G. Suo, F. Y. Ouyang, and P. L. Liu, “Concurrent electromigration and creep in lead-free solder,” *Journal of Applied Physics,* vol. 110, no. 8, pp. 083716, 2011.

[32] Y. W. Shi, J. P. Liu, Y. F. Yan, Z. D. Xia, Y. P. Lei, F. Guo, and X. Y. Li, “Creep properties of composite solders reinforced with nano- and microsized particles,” *Journal of Electronic Materials,* vol. 37, no. 4, pp. 507-514, April, 2008.

[33] J. P. Liu, F. Guo, Y. F. Yan, W. B. Wang, and Y. W. Shi, “Development of creep-resistant, nanosized Ag particle-reinforced Sn-Pb composite solders,” *Journal of Electronic Materials,* vol. 33, no. 9, pp. 958-963, September, 2004.

[34] X. J. Hu, L. N. Jiang, and K. E. Goodson, “Thermal characterization of eutectic alloy thermal interface materials with void-like inclusions,” in 20th IEEE Semiconductor Thermal Measurement and Management Symposium, San Jose, CA, 2004.

[35] J. Due, and A. J. Robinson, “Reliability of thermal interface materials: A review,” *Applied Thermal Engineering,* vol. 50, no. 1, pp. 455-463, 2013.

المنارة للاستشارات

www.manaraa.com

[36] A. S. Fleischer, L. Chang, and B. C. Johnson, “The effect of die attach voiding on the thermal resistance of chip level packages,” *Microelectronics Reliability,* vol. 46, no. 5-6, pp. 794-804, 2006.

[37] A. Gowda, D. Esler, S. Tonapi, A. Zhong, K. Srihari, and F. Schattenmann, “Micron and sub-micron scale characterization of interfaces in thermal interface material systems,” *ASME Journal of Electronic Packaging,* vol. 128, no. 2, pp. 130-136, 2006.

[38] J. Xu, and T. S. Fisher, “Enhancement of thermal interface materials with carbon nanotube arrays,” *International Journal of Heat and Mass Transfer,* vol. 49, no. 9-10, pp. 1658-1666, 2006.

[39] D. J. Yang, Q. Zhang, G. Chen, S. F. Yoon, J. Ahn, S. G. Wang, Q. Zhou, Q. Wang, and J. Q. Li, “Thermal conductivity of multiwalled carbon nanotubes,” *Physical Review B,* vol. 66, no. 16, pp. 165440, 31 October, 2002.

[40] Q. Li, C. Liu, X. Wang, and S. Fan, “Measuring the thermal conductivity of individual carbon nanotubes by the Raman shift method,” *Nanotechnology,* vol. 20, no. 14, pp. 145702, 8 April, 2009.

[41] K. M. Shahil, and A. A. Balandin, “Graphene-multilayer graphene nanocomposites as highly efficient thermal interface materials,” *Nano Letters,* vol. 12, no. 2, pp. 861-867, 8 February 2012.

[42] A. A. Balandin, “Thermal properties of graphene and nanostructured carbon materials,” *Nature Materials,* vol. 10, no. 8, pp. 569-581, 22 July, 2011.

[43] Y. Hong, J. Zhang, and X. C. Zeng, “Thermal contact resistance across a linear heterojunction within a hybrid graphene/hexagonal boron nitride sheet,” *Physical Chemistry Chemical Physics,* vol. 18, no. 35, pp. 24164-24170, 21 September, 2016.

[44] E. Pop, V. Varshney, and A. K. Roy, “Thermal properties of graphene: Fundamentals and applications,” *MRS Bulletin,* vol. 37, no. 12, pp. 1273-1281, December, 2012.

[45] P. Kim, L. Shi, A. Majumdar, and P. L. McEuen, “Thermal transport measurements of individual multiwalled nanotubes,” *Physical Review Letters,* vol. 87, no. 21, pp. 215502, 19 November, 2001.

[46] A. J. McNamara, Y. Joshi, and Z. M. Zhang, “Characterization of nanostructured thermal interface materials - A review,” *International Journal of Thermal Sciences,* vol. 62, pp. 2-11, 2012.

[47] D. C. Lin, S. Liu, T. M. Guo, G. X. Wang, T. S. Srivatsan, and M. Petraroli, “An investigation of nanoparticles addition on solidification kinetics and microstructure

المنارة للاستشارات
www.manaraa.com

development of tin-lead solder," *Materials Science and Engineering: A,* vol. 360, no. 1-2, pp. 285-292, 2003.

[48] L. Zhang, and K. N. Tu, "Structure and properties of lead-free solders bearing micro and nano particles," *Materials Science and Engineering: R: Reports,* vol. 82, pp. 1-32, August, 2014.

[49] R. L. Webb, and J. P. Gwinn, "Low melting point thermal interface material," in 8th Intersociety Conference on Thermal and Thermomechanical Phenomena in Electronic Systems, ITHERM 2002, San Diego, CA, 2002, pp. 671-676.

[50] S. V. Garimella, A. S. Fleischer, J. Y. Murthy, A. Keshavarzi, R. Prasher, C. Patel, S. H. Bhavnani, R. Venkatasubramanian, R. Mahajan, Y. Joshi, B. Sammakia, B. A. Myers, L. Chorosinski, M. Baelmans, P. Sathyamurthy, and P. E. Raad, "Thermal challenges in next-generation electronic systems," *IEEE Transactions on Components and Packaging Technologies,* vol. 31, no. 4, pp. 801-815, December, 2008.

[51] J. Liu, B. Michel, M. Rencz, C. Tantolin, C. Sarno, R. Miessner, K. V. Schuett, X. Tang, S. Demoustier, and A. Ziaei, "Recent progress of thermal interface material research - An overview," in 14th International Workshop on Thermal Inveatigation of ICs and Systems, Rome, Italy, 2008, pp. 156-162.

[52] P. P. S. S. Abadi, C. K. Leong, and D. D. L. Chung, "Factors that govern the performance of thermal interface materials," *Journal of Electronic Materials,* vol. 38, no. 1, pp. 175-192, 2009.

[53] C. P. Chiu, B. Chandran, K. Mello, and K. Kelly, "An accelerated reliability test method to predict thermal grease pump-out in flip-chip applications," in 51st Electronic Components and Technology Conference, Orlando, FL, 2001.

[54] S. Lijima, "Helical microtubules of graphitic carbon," *Nature,* vol. 354, pp. 56-58, November, 1991.

[55] P. C. Irwin, Y. Cao, A. Bansal, and L. S. Schadler, "Thermal and mechanical properties of polyimide nanocomposites," in Annual Report Conference on Electrical Insulation and Dielectric Phenomena, Albuquerque, NM, 2003, pp. 120-123.

[56] W. D. Callister, and D. G. Rethwisch, *Materials Science and Engineering: An introduction 7th Edition*, New York: Wiley, 2007.

[57] D. Roylance, *Mechanical Properties of Materials*, 2008.

[58] V. Singhal, P. J. Litke, A. F. Black, and S. V. Garimella, "An experimentally validated thermo-mechanical model for the prediction of thermal contact

المنارة للاستشارات

www.manaraa.com

conductance," *International Journal of Heat and Mass Transfer,* vol. 48, no. 25-26, pp. 5446-5459, 2005.

[59] J. H. Saleh, and K. Marais, "Highlights from the early (and pre-) history of reliability engineering," *Reliability Engineering & System Safety,* vol. 91, no. 2, pp. 249-256, 2006.

[60] M. Ohring, *Reliability and Failure of Electronic Materials and Devices*: Academic Press, 1998.

[61] K. C. Kapur, and M. Pecht, *Reliability Engineering*: John Wiley & Sons, 2014.

[62] E. Zio, "Reliability engineering: Old problems and new challenges," *Reliability Engineering & System Safety,* vol. 94, no. 2, pp. 125-141, 2009.

[63] D. DeVoto, P. Paret, M. Mihalic, A. Bar-Cohen, and K. Matin, "Thermal performance and reliability characterization of bonded interface materials (BIMs)," in IEEE Intersociety Conference on Thermal and Thermomechanical Phenomena in Electronic Systems (ITherm), Orlando, FL, 2014.

[64] Y. Li, and C. P. Wong, "Recent advances of conductive adhesives as a lead-free alternative in electronic packaging: Materials, processing, reliability and applications," *Materials Science and Engineering R,* vol. 51, no. 1-3, pp. 1-35, 2006.

[65] M. AboRas, R. Haug, R. Schacht, C. Monory-Plantier, D. May, B. Wunderle, T. Winkler, and B. Michel, "Combined and accelerated in-situ measuerment method for reliability and aging analyses of thermal interface materials," in 17th International Workshop on Thermal Investigations of ICs and Systems (THERMINIC), Paris, France, 2011.

[66] O. Tabata, and T. Tsuchiya, *Reliability of MEMS: Testing of Materials and Devices*: John Wiley & Sons, 2013.

[67] V. Khuu, M. Osterman, A. Bar-Cohen, and M. Pecht, "Effects of temperature cycling and elevated temperature/humidity on the thermal performance of thermal interface materials," *IEEE Transactions on Device and Materials Reliability,* vol. 9, no. 3, pp. 379-391, September, 2009.

[68] N. Goel, T. K. Anoop, A. Bhattacharya, J. A. Cervantes, R. K. Mongia, S. V. Machiroutu, H. L. Lin, Y. C. Huang, K. C. Fan, B. L. Denq, C. H. Liu, C. H. Lin, C. W. Tien, and J. H. Pan, "Technical review of characterization methods for thermal interface Materials (TIM)," in 11th Intersociety Conference on Thermal and Thermomechanical Phenomena in Electronic Systems, Orlando, FL, 2008, pp. 248-258.

[69] N. Islam, S. W. Lee, M. Jimarez, J. Y. Lee, and J. Galloway, "TIM degradation in flip chip packages," in 11th Intersociety Conference on Thermal and

المنارة للاستشارات
www.manaraa.com

Thermomechanical Phenomena in Electronic Systems, Orlando, FL, 2008, pp. 259-265.

[70] C. I. Chen, C. Y. Ni, H. Y. Pan, C. M. Chang, and D. S. Liu, “Practical evaluation for longterm stability of TIM,” *Experimental Techniques,* vol. 33, no. 1, pp. 28-32, 2009.

[71] S. N. Paisner, M. Touzelbaev, G. Refai-Ahmed, and Y. Z. Yang, “New developments for a no-pump-out high-performance thermal grease,” in 12th IEEE Intersociety Conference on Thermal and Thermomechanical Phenomena in Electronic Systems, Las Vegas, NV, 2010.

[72] S. L. B. Dal, “Degradation mechanisms of siloxane-based thermal interface materials under reliability stress conditions,” in 42nd Annual. 2004 IEEE International Reliability Physics Symposium Proceedings, Phoenix, AZ, 2004, pp. 537-542.

[73] T. H. Wang, H. Y. Chen, C. C. Lee, and Y. S. Lai, “High-power-used thermal gel degradation Evaluation on board-level HFCBGA subjected to reliability tests,” in 4th International Microsystems, Packaging, Assembly and Circuits Technology Conference, Taipei, Taiwan, 2009, pp. 465-468.

[74] C. Ramaswamy, S. Shinde, F. Pompeo, W. Sablinski, and S. Bradley, “Phase change materials as a viable thermal interface material for high-power electronic applications,” in 9th Intersociety Conference on Thermal and Thermomechanical Phenomena in Electronic Systems, Las Vegas, NV, 2004, pp. 687-691.

[75] A. Gowda, D. Esler, S. N. Paisner, S. Tonapi, K. Nagarkar, and K. Srihari, “Reliability testing of silicone-based thermal greases,” in 21st IEEE Semiconductor Thermal Measurement and Management Symposium, San Jose, CA, 2005, pp. 64-71.

[76] L. L. Ma, S. X. Bao, D. C. Lv, Z. B. Du, and S. L. Li, “Application of C-mode scanning acoustic microscopy in packaging,” in 8th International Conference on Electronic Packaging Technology, 2007.

[77] S. Oberhoff, K. Goetz, K. Trojan, M. Zoeller, and J. Glueck, “Application of high frequency scanning acoustic microscopy for the failure analysis and reliability assessment of MEMS sensors,” *Microelectronics Reliability,* vol. 64, pp. 656-659, 2016.

[78] A. Gupta, Y. M. Liu, T. Zamora, and T. Paddock, “Thermal imaging for detecting thermal interface issues in assembly and reliability stressing,” in 10th Intersociety Conference on Thermal and Thermomechanical Phenomena in Electronics Systems, San Diego, CA, 2006, pp. 945.

المنارة للاستشارات

www.manaraa.com

[79] L. Bharatham, W. S. Fong, J. Torresola, and C. C. Koang, “Qualification of phase change thermal interface material for wave solder heat sink on FCBGA package,” in Proceedings of 7th Electronic Packaging Technology Conference, Shenzhen, China, 2005.

[80] Y. J. Lee, “Thermo-mechanical properties of high performance thermal interface gap filler pads,” in 12th IEEE Intersociety Conference on Thermal and Thermomechanical Phenomena in Electronic Systems, Las Vegas, NV, 2010.

[81] A. Mir, R. Zitoune, F. Collombet, and B. Bezzazi, “Study of mechanical and thermomechanical properties of jute/epoxy composite laminate,” *Journal of Reinforced Plastics and Composites,* vol. 29, no. 11, pp. 1669-1680, 2010.

[82] Z. Q. Gong, and K. Komvopoulos, “Mechanical and thermomechanical elastic-plastic contact analysis of layered media with patterned surfaces,” *Journal of Tribology,* vol. 126, pp. 9-17, January, 2004.

[83] R. Skuriat, J. F. Li, P. A. Agyakwa, N. Mattey, P. Evans, and C. M. Johnson, “Degradation of thermal interface materials for high-temperature power electronics applications,” *Microelectronics Reliability,* vol. 53, no. 12, pp. 1933-1942, December, 2013.

[84] R. T. Wu, X. Wang, and A. Atkinson, “On the interfacial degradation mechanisms of thermal barrier coating systems: Effects of bond coat composition,” *Acta Materialia,* vol. 58, no. 17, pp. 5578-5585, October, 2010.

[85] J. A. Jeong, H. K. Kim, H. W. Koo, and T. W. Kim, “Transmission electron microscopy study of degradation in transparent indium tin oxide/Ag/indium tin oxide multilayer films,” *Applied Physics Letters,* vol. 103, no. 1, pp. 011902, 2013.

[86] E. A. Starke, R. H. Cornelia, L. B. Gerszczuk, L. M. Karabin, J. J. Lewandowski, A. Saxena, J. C. Seferis, R. E. Tressler, and D. D. Ward, *Accelerated Aging of Materials and Structures: The Effects of Long-Term Elevated-Temperature Exposure*, Washington, D.C.: National Academy Press, 1996.

[87] K. Pielichowski, and J. Njuguna, *Thermal Degradation of Polymeric Materials*, Shawbury, Shrewsbury, Shropshire, SY4 4NR, UK: Rapra Technology Limited, 2005.

[88] T. L. Bergman, A. S. Lavine, F. P. Incropera, and D. P. DeWitt, *Fundamentals of heat and mass transfer, 7th edition*, Hoboken, NJ: John Wiley & Sons, Inc., 2011.

[89] N. Kürti, B. V. Rollin, and F. Simon, “Preliminary experiments on temperature equilibria at very low temperatures,” *Physica,* vol. 3, no. 1-4, pp. 266-274, 1936.

المنارة للاستشارات
www.manaraa.com

[90] P. L. Kapitza, "Heat transfer and superfluidity of helium II," *Physical Review,* vol. 60, no. 4, pp. 354-355, 15 August, 1941.

[91] R. Prasher, "Surface chemistry and characteristics based model for the thermal contact resistance of fluidic interstitial thermal interface materials," *ASME Journal of Heat Transfer,* vol. 123, no. 5, pp. 969-975, October, 2001.

[92] J. Suh, R. P. Dillon, and S. Tseng, *Thermal interface materials selection and application guidelines: In perspective of Xilinx Virtex-5QV thermal management*, Jet Propulsion Laboratory, Pasadena, CA, 2015.

[93] M. G. Cooper, B. B. Mikic, and M. M. Yovanovich, "Thermal contact conductance," *International Journal of Heat and Mass Transfer,* vol. 12, no. 3, pp. 279-300, March, 1969.

[94] D. G. Gilmore *Spacecraft Thermal Control Handbook, Volume I: Fundamental Technologies* El Segundo, CA: The Aerospace Press, 2002.

[95] L. Bharatham, W. S. Fong, C. J. Leong, and C. P. Chiu, "A study of application pressure on thermal interface material performance and reliability on FCBGA package," in International Conference on Electronic Materials and Packaging, Kowloon, China 2006.

[96] D. L. Zhao, X. Qian, X. K. Gu, S. A. Jajja, and R. G. Yang, "Measurement techniques for thermal conductivity and interfacial thermal conductance of bulk and thin film materials " *ASME Journal of Electronic Packaging,* vol. 138, no. 4, pp. 040802, 2016.

[97] J. J. Park, and M. Taya, "Design of thermal interface material with high thermal conductivity and measurement apparatus," *Journal of Electronic Materials,* vol. 128, no. 1, pp. 46-52, March, 2006.

[98] A. L. Pope, B. Zawilski, and T. M. Tritt, "Description of removable sample mount apparatus for rapid thermal conductivity measurements," *Cryogenics,* vol. 41, no. 10, pp. 725-731, October, 2001.

[99] W. G. Hess, "Thermocouple conduction error with radiation heat loss," Department of Aerospace and Mechanical Engineering, The University of Arizona, Tucson, AZ, 1965.

[100] K. M. F. Shahil, and A. A. Balandin, "Thermal properties of graphene and multilayer graphene: Applications in thermal interface materials," *Solid State Communications,* vol. 152, no. 15, pp. 1331-1340, August, 2012.

[101] J. R. Culham, P. Teertstra, I. Savija, and M. M. Yovanovich, "Design, assembly and commissioning of a test apparatus for characterizing thermal interface

المنارة للاستشارات
www.manaraa.com

materials," in 8th Intersociety Conference on Thermal and Thermomechanical Phenomena in Electronic Systems, ITHERM 2002, San Diego, CA, 2002, pp. 128-135.

[102] J. P. Gwinn, M. Saini, and R. L. Webb, "Apparatus for accurate measurement of interface resistance of high performance thermal interface materials," in 8th Intersociety Conference on Thermal and Thermomechanical Phenomena in Electronic Systems, ITHERM 2002, San Diego, CA, 2002, pp. 644-650.

[103] D. Kearns, "Improving accuracy and flexibility of ASTM D5470 for high performance thermal interface materials," in 19th IEEE Semiconductor Thermal Measurement and Management Symposium, 2003, pp. 129-133.

[104] V. Khuu, "Evaluation of thermal interface materials and the laser flash method," Mechanical Engineering, University of Maryland, College Park, MD, 2009.

[105] W. J. Parker, R. J. Jenkins, C. P. Butler, and G. L. Abbott, "Flash method of determining thermal diffusivity, heat capacity, and thermal conductivity," *Journal of Applied Physics,* vol. 32, no. 9, pp. 1679-1684, 1961.

[106] L. Vozár, and W. Hohenauer, "Flash method of measuring the thermal diffusivity. A review," *High Temperatures-High Pressures,* vol. 35/36, no. 3, pp. 253-264, 2003.

[107] D. G. Cahill, "Thermal conductivity measurement from 30 to 750 K: The 3ω method," *Review of Scientific Instruments,* vol. 61, no. 2, pp. 802-808, February, 1990.

[108] *Flashline thermal diffusivity measuring system*, Anter Corporation, Pittsburgh, PA, 2005.

[109] V. Khuu, M. Osterman, A. Bar-Cohen, and M. Pecht, "Considerations in the use of the laser flash method for thermal measurements of thermal interface materials," *IEEE Transactions on Components, Packaging and Manufacturing Technology,* vol. 1, no. 7, pp. 1015-1028, July, 2011.

[110] *Standard test method for thermal diffusivity by the flash method*, vol. 14.05, Huazhong University of Science, West Conshohocken, PA, 2013.

[111] I. M. Abdulagatov, Z. Z. Abdulagatova, S. N. Kallaev, A. G. Bakmaev, and P. G. Ranjith, "Thermal-diffusivity and heat-capacity measurements of sandstone at high temperatures using laser flash and DSC methods," *International Journal of Thermophysics,* vol. 36, no. 4, pp. 658-691, April, 2015.

[112] H. S. Carslaw, and J. C. Jaeger, *Conduction of Heat in Solids, 2nd Edition*, London: Oxford University Press, 1986.

المنارة للاستشارات

www.manaraa.com

[113] J. A. Cape, and G. W. Lehman, "Temperature and finite pulse - time effects in the flash method for measuring thermal diffusivity," *Journal of Applied Physics,* vol. 34, no. 7, pp. 1909-1913, July, 1963.

[114] R. E. Taylor, and J. A. Cape, "Finite pulse - time effects in the flash diffusivity technique," *Applied Physics Letters,* vol. 5, no. 10, pp. 212-213, 15 November, 1964.

[115] D. A. Watt, "Theory of thermal diffusivity by pulse technique," *British Journal of Applied Physics,* vol. 17, no. 2, pp. 231-240, 1966.

[116] T. Azumi, and Y. Takahashi, "Novel finite pulse - width correction in flash thermal diffusivity measurement," *Review of Scientific Instruments,* vol. 52, no. 9, pp. 1411-1413, September, 1981.

[117] L. M. Clark III, and R. E. Taylor, "Radiation loss in the flash method for thermal diffusivity," *Journal of Applied Physics,* vol. 46, no. 2, pp. 714-719, February, 1975.

[118] F. I. Chu, R. E. Taylor, and A. B. Donaldson, "Thermal diffusivity measurements at high temperatures by the radial flash method," *Journal of Applied Physics,* vol. 51, no. 1, pp. 336-341, 1980.

[119] R. D. Cowan, "Pulse method of measuring thermal diffusivity at high temperatures," *Journal of Applied Physics,* vol. 34, no. 4, pp. 926-927, April, 1963.

[120] A. B. Donaldson, and R. E. Taylor, "Thermal diffusivity measurement by a radial heat flow method," *Journal of Applied Physics,* vol. 46, no. 10, pp. 4584-4589, October, 1975.

[121] H. J. Lee, and R. E. Taylor, "Thermal diffusivity of dispersed composites," *Journal of Applied Physics,* vol. 47, no. 1, pp. 148-151, 1976.

[122] R. C. Heckman, "Finite pulse - time and heat - loss effects in pulse thermal diffusivity measurements," *Journal of Applied Physics,* vol. 44, no. 4, pp. 1455-1460, April, 1973.

[123] R. C. Heckman, *Error analysis of the flash thermal diffusivity technique*, p.^pp. 491-498, New York, NY: Springer, 1976.

[124] J. A. Koski, "Improved data-reduction methods for laser-pulse-diffusivity determination with the use of minicomputers," in International Joint Conference on Thermophysical Properties, Gaithersburg, MD, 1981, pp. 94-103.

[125] V. Gektin, "Thermal management of voids and delamination in TIMs," in The Pacific Rim/ASME International Intersociety Electronic & Photonic Packaging Conference, San Francisco, CA, 2005, pp. 641-645.

المنارة للاستشارات
www.manaraa.com

[126] R. K. McGeary, “Mechanical packing of spherical particles,” *Journal of the American Ceramic Society,* vol. 44, no. 10, pp. 513-522, October, 1961.

[127] R. Prasher, P. Koning, J. Shipley, and A. Devpura, “Dependence of thermal conductivity and mechanical rigidity of particle-laden polymeric thermal interface material on particle volume fraction,” *ASME Journal of Electronic Packaging,* vol. 125, no. 3, pp. 386-391, September, 2003.

[128] R. C. Progelhof, J. L. Throne, and R. R. Ruetsch, “Methods for predicting the thermal conductivity of composite systems: A review,” *Polymer Engineering and Science,* vol. 16, no. 9, pp. 615-625, September, 1976.

[129] H. Vinh-Thang, and S. Kaliaguine, “Predictive models for mixed-matrix membrane performance: A review,” *Chemical Reviews,* vol. 113, no. 7, pp. 4980-5028, 10 July, 2013.

[130] M. M. Awad, and Y. S. Muzychka, “Effective property models for homogeneous two-phase flows,” *Experimental Thermal and Fluid Science,* vol. 33, no. 1, pp. 106-113, 2008.

[131] R. Pal, “Permeation models for mixed matrix membranes,” *Journal of Colloid Interface Science,* vol. 317, no. 1, pp. 191-198, 1 January, 2008.

[132] J. C. Maxwell, *A treatise on electricity and magnetism*, Oxford, England: Oxford: Clarendon Press, 1873.

[133] J. C. Maxwell Garnett, “Colours in metal glasses and metallic films,” *Proceedings of the Royal Society of London,* vol. 73, pp. 443-445, 2 June, 1904.

[134] L. Rayleigh, “On the influence of obstacles arranged in rectangular order upon the properties of a medium,” *Philosophical Magazine Series 5,* vol. 34, no. 211, pp. 481-502, 1892.

[135] D. A. G. Bruggeman, “Berechnung verschiedener physikalischer Konstanten von heterogenen Substanzen (Calculation of various physical constants of heterogeneous substances),” *Annalen der Physik,* vol. 416, no. 7, pp. 636-664, 1935.

[136] R. Landauer, “The electrical resistance of binary metallic mixtures,” *Journal of Applied Physics,* vol. 23, no. 7, pp. 779-784, July, 1952.

[137] T. B. Lewis, and L. E. Nielsen, “Dynamic mechanical properties of particulate-filled composites,” *Journal of Applied Polymer Science,* vol. 14, no. 6, pp. 1449-1471, June, 1970.

[138] S. Kirkpatrick, “Percolation and conduction,” *Reviews of Modern Physics,* vol. 45, no. 4, pp. 574-588, October, 1973.

المنارة للاستشارات

www.manaraa.com

[139] A. Devpura, P. E. Phelan, and R. S. Prasher, "Size effects on the thermal conductivity of polymers laden with highly conductive filler particles," *Microscale Thermophysical Engineering,* vol. 5, no. 3, pp. 177-189, 2001.

[140] J. K. Carson, "Prediction of the thermal conductivity of porous food," Food Engineering, Massey University, Palmerston North, New Zealand, 2002.

[141] G. C. J. Bart, "Thermal conduction in non homogeneous and phase change media," Delft University of Technology, Netherlands, 1994.

[142] J. K. Carson, S. J. Lovatt, D. J. Tanner, and A. C. Cleland, "Thermal conductivity bounds for isotropic, porous materials," *International Journal of Heat and Mass Transfer,* vol. 48, no. 11, pp. 2150-2158, 8 March, 2005.

[143] T. Zakri, J. P. Laurent, and M. Vauclin, "Theoretical evidence for 'Lichtenecker's mixture formulae' based on the effective medium theory," *Journal of Physics D: Applied Physics,* vol. 31, no. 13, pp. 1589-1594, 1998.

[144] H. Fricke, "A mathematical treatment of the electric conductivity and capacity of disperse systems I. The electric conductivity of a suspension of homogeneous spheroids," *Physical Review,* vol. 24, no. 5, pp. 575-587, 1 November, 1924.

[145] H. C. Burger, "Das lertvermogen verdunnter mischkristallfreier lonsunge," *Physikalische Zeitschrift,* vol. 20, pp. 73-76, 1915.

[146] R. L. Hamilton, and O. K. Crosser, "Thermal conductivity of heterogeneous two-component systems," *Industrial & Engineering Chemistry Fundamentals,* vol. 1, no. 3, pp. 187-191, August, 1962.

[147] L. E. Nielsen, "The thermal and electrical conductivity of two-phase systems," *Industrial & Engineering Chemistry Fundamentals,* vol. 13, no. 1, pp. 17-20, February, 1974.

[148] A. Ochsner, and G. E. Murch, *Heat Transfer in Multi-Phase Materials*: Springer-Verlag Berlin Heidelberg, 2011.

[149] A. G. Every, Y. Tzou, and R. Raj, "The effect of particle size on the thermal conductivity of ZnS/diamond composites," *Acta Metallurgica et Materialia,* vol. 40, no. 1, pp. 123-129, January, 1992.

[150] C. W. Nan, R. Birringer, D. R. Clarke, and H. Gleiter, "Effective thermal conductivity of particulate composites with interfacial thermal resistance," *Journal of Applied Physics,* vol. 81, no. 10, pp. 6692-6699, 15 May, 1997.

المنارة للاستشارات
www.manaraa.com

[151] D. P. H. Hasselman, and L. F. Johnson, “Effective thermal conductivity of composites with interfacial thermal barrier resistance,” *Journal of Composite Materials,* vol. 21, no. 6, pp. 508-515, June, 1987.

[152] Y. Benveniste, “Effective thermal conductivity of composites with a thermal contact resistance between the constituents: Nondilute case,” *Journal of Applied Physics,* vol. 61, no. 8, pp. 2840-2843, 1987.

[153] K. Pietrak, and T. S. Wiśniewski, “A review of models for effective thermal conductivity of composite materials,” *Journal of Power Technologies,* vol. 95, no. 1, pp. 14-24, 2015.

[154] I. Tavman, and T. Evgin, “Metal particle filled, thermally conductive polymer composites for electronic packaging applications,” in 21st International Symposium for Design and Technology in Electronic Packaging (SIITME), Brasov, Romania, 2015, pp. 31-35.

[155] R. Landauer, "Electrical conductivity in inhomogeneous media." pp. 2-45.

[156] Z. Hicsasmaz, and J. T. Clayton, “Characterization of the pore structure of starch based food materials,” *Food Structure,* vol. 11, no. 2, pp. 115-132, 1992.

[157] A. Devpura, P. E. Phelan, and R. S. Prasher, “Percolation theory applied to the analysis of thermal interface materials in flip-chip technology,” in 7th Intersociety Conference on Thermal and Thermomechanical Phenomena in Electronic Systems, ITHERM 2000 Las Vegas, NV, 2000, pp. 21-28.

[158] S. Kanuparthi, X. Zhang, G. Subbarayan, B. G. Sammakia, T. Siegmund, and S. Tonapi, “Random network percolation models for particulate thermal interface materials,” in 10th Intersociety Conference on Thermal and Thermomechanical Phenomena in Electronic Systems, ITHERM 2006, San Diego, CA, 2006, pp. 1192-1198.

[159] G. Q. Zhang, Y. P. Xia, H. Wang, Y. Tao, G. L. Tao, S. T. Tu, and H. P. Wu, “A percolation model of thermal conductivity for filled polymer composites,” *Journal of Composite Materials,* vol. 44, no. 8, pp. 963-970, 2010.

[160] M. Monde, and Y. Mitsutake, “A new estimation method of thermal diffusivity using analytical inverse solution for one-dimensional heat conduction,” *International Journal of Heat and Mass Transfer,* vol. 44, no. 16, pp. 3169-3177, August, 2001.

[161] X. Q. Fang, “Scattering of thermal waves and non-steady effective thermal conductivity of composites with coated particles,” *Applied Thermal Engineering,* vol. 29, no. 5-6, pp. 925-931, 2009.

المنارة للاستشارات
www.manaraa.com

[162] L. C. Davis, and B. E. Artz, “Thermal conductivity of metal - matrix composites,” *Journal of Applied Physics,* vol. 77, no. 10, pp. 4954-4960, 15 May, 1995.

[163] J. Yvonnet, Q. C. He, and C. Toulemonde, “Numerical modelling of the effective conductivities of composites with arbitrarily shaped inclusions and highly conducting interface,” *Composites Science and Technology,* vol. 68, no. 13, pp. 2818-2825, 2008.

[164] C. Yue, Y. J. Zhang, Z. L. Hu, J. Liu, and Z. N. Cheng, “Modeling of the effective thermal conductivity of composite materials with FEM based on resistor networks approach,” *Microsystem Technologies,* vol. 16, no. 4, pp. 633-639, 2010.

[165] B. Dan, S. Kanuparthi, G. Subbarayan, and B. Sammakia, “An improved network model for determining the effective thermal conductivity of particulate thermal interface materials,” in ASME InterPACK Conference, San Francisco, CA, 2009, pp. 69-81.

[166] S. Kanuparthi, G. Subbarayan, T. Siegmund, and B. Sammakia, “An Efficient Network Model for Determining the Effective Thermal Conductivity of Particulate Thermal Interface Materials,” *IEEE Transactions on Components and Packaging Technologies,* vol. 31, no. 3, pp. 611-621, 2008.

[167] T. T. Zhang, B. Sammakia, and H. Wang, “Nanocomposite pastes for thermal and mechanical bonding,” in 64th Electronic Components & Technology Conference, Orlando, FL, 2014, pp. 2175-2180.

[168] S. Magdassi, A. Bassa, Y. Vinetsky, and A. Kamyshny, “Silver nanoparticles as pigments for water-based ink-jet inks,” *Chemistry of Materials* vol. 15, no. 11, pp. 2208-2217, 2003.

[169] A. Kamyshny, J. Steinke, and S. Magdassi, “Metal-based inkjet inks for printed electronics,” *The Open Applied Physics Journal,* vol. 4, no. 1, pp. 19-36, 2011.

[170] S. S. Shankar, A. Rai, A. Ahmad, and M. Sastry, “Rapid synthesis of Au, Ag, and bimetallic Au core-Ag shell nanoparticles using Neem (Azadirachta indica) leaf broth,” *Journal of Colloid and Interface Science,* vol. 275, no. 2, pp. 496-502, 15 July, 2004.

[171] M. J. Bloemer, J. W. Haus, and P. R. Ashley, “Degenerate four-wave mixing in colloidal gold as a function of particle size,” *Journal of the Optical Society of America B,* vol. 7, no. 5, pp. 790-795, May, 1990.

[172] A. Otto, T. Bornemann, Ü. Ertürk, I. Mrozek, and C. Pettenkofer, “Model of electronically enhanced Raman scattering from adsorbates on cold-deposited silver,” *Surface Science,* vol. 210, no. 3, pp. 363-386, 3 March, 1989.

المنارة للاستشارات
www.manaraa.com

[173] A. Otto, I. Mrozek, H. Grabhorn, and W. Akemann, “Surface-enhanced Raman scattering,” *Journal of Physics: Condensed Matter,* vol. 4, no. 5, pp. 1143-1212, 1992.

[174] Q. Jiang, S. H. Zhang, and J. C. Li, “Grain size-dependent diffusion activation energy in nanomaterials,” *Solid State Communications,* vol. 130, no. 9, pp. 581-584, 2004.

[175] S. L. Lai, J. Y. Guo, V. Petrova, G. Ramanath, and L. H. Allen, “Size-dependent melting properties of small tin particles: Nanocalorimetric measurements,” *Physical Review Letters,* vol. 77, no. 1, pp. 99-102, 1 July, 1996.

[176] K. Katayama, H. Nomura, H. Ogata, and T. Eitoku, “Diffusion coefficients for nanoparticles under flow and stop-flow conditions,” *Physical Chemistry Chemical Physics,* vol. 11, no. 44, pp. 10494-10499, 28 November, 2009.

[177] M. Valden, X. Lai, and D. W. Goodman, “Onset of catalytic activity of gold clusters on titania with the appearance of nonmetallic properties,” *Science,* vol. 281, no. 5383, pp. 1647-1650, 11 September, 1998.

[178] K. L. Kelly, E. Coronado, L. L. Zhao, and G. C. Schatz, “The optical properties of metal nanoparticles: The influence of size, shape, and dielectric environment,” *Journal of Physical Chemistry B,* vol. 107, no. 3, pp. 668-677, 21 December, 2003.

[179] C. Sonnichsen, B. M. Reinhard, J. Liphardt, and A. P. Alivisatos, “A molecular ruler based on plasmon coupling of single gold and silver nanoparticles,” *Nature Biotechnology,* vol. 23, no. 6, pp. 741-745, June, 2005.

[180] S. B. Fuller, E. J. Wilhelm, and J. M. Jacobson, “Ink-jet printed nanoparticle microelectromechanical systems,” *Journal of Microelectromechanical Systems,* vol. 11, no. 1, pp. 54-60, February, 2002.

[181] A. L. Dearden, P. J. Smith, D. Y. Shin, N. Reis, B. Derby, and P. O'Brien, “A low curing temperature silver ink for use in ink-jet printing and subsequent production of conductive tracks,” *Macromolecular Rapid Communications,* vol. 26, no. 4, pp. 315-318, February, 2005.

[182] H. H. Lee, K. S. Chou, and K. C. Huang, “Inkjet printing of nanosized silver colloids,” *Nanotechnology,* vol. 16, no. 10, pp. 2436-2441, Oct, 2005.

[183] J. Perelaer, B. J. de Gans, and U. S. Schubert, “Ink-jet printing and microwave sintering of conductive silver tracks,” *Advanced Materials,* vol. 18, no. 16, pp. 2101-2104, 2006.

المنارة للاستشارات
www.manaraa.com

[184] J. Perelaer, C. E. Hendriks, A. W. de Laat, and U. S. Schubert, “One-step inkjet printing of conductive silver tracks on polymer substrates,” *Nanotechnology,* vol. 20, no. 16, pp. 165303, 22 April, 2009.

[185] A. Hu, J. Y. Guo, H. Alarifi, G. Patane, Y. Zhou, G. Compagnini, and C. X. Xu, “Low temperature sintering of Ag nanoparticles for flexible electronics packaging,” *Applied Physics Letters,* vol. 97, no. 15, pp. 153117, 2010.

[186] M. Singh, H. M. Haverinen, P. Dhagat, and G. E. Jabbour, “Inkjet printing-process and its applications,” *Advanced Materials,* vol. 22, no. 6, pp. 673-685, 9 February, 2010.

[187] M. Hösel, and F. C. Krebs, “Large-scale roll-to-roll photonic sintering of flexo printed silver nanoparticle electrodes,” *Journal of Materials Chemistry,* vol. 22, no. 31, pp. 15683-15688, 2012.

[188] J. Perelaer, A. W. M. de Laat, C. E. Hendriks, and U. S. Schubert, “Inkjet-printed silver tracks: low temperature curing and thermal stability investigation,” *Journal of Materials Chemistry,* vol. 18, pp. 3209–3215, 2008.

[189] I. Reinhold, C. E. Hendriks, R. Eckardt, J. M. Kranenburg, J. Perelaer, R. R. Baumann, and U. S. Schubert, “Argon plasma sintering of inkjet printed silver tracks on polymer substrates,” *Journal of Materials Chemistry,* vol. 19, no. 21, pp. 3384-3388, 2009.

[190] M. Zhang, M. Y. Efremov, F. Schiettekatte, E. A. Olson, A. T. Kwan, S. L. Lai, T. Wisleder, J. E. Greene, and L. H. Allen, “Size-dependent melting point depression of nanostructures: Nanocalorimetric measurements,” *Physcal Review B,* vol. 62, no. 15, pp. 10548-10557, 15 October, 2000.

[191] E. A. Olson, M. Y. Efremov, M. Zhang, Z. Zhang, and L. H. Allen, “Size-dependent melting of Bi nanoparticles,” *Journal of Applied Physics,* vol. 97, no. 3, pp. 034304, 2005.

[192] H. Yu, L. L. Li, and Y. J. Zhang, “Silver nanoparticle-based thermal interface materials with ultra-low thermal resistance for power electronics applications,” *Scripta Materialia,* vol. 66, no. 11, pp. 931-934, June, 2012.

[193] L. F. Dong, Z. L. Cui, and Z. K. Zhang, “Gas sensing properties of nano-ZnO prepared by arc plasma method,” *NanoStructured Materials,* vol. 8, no. 7, pp. 815-823, 1997.

[194] A. Yabuki, and N. Arriffin, “Electrical conductivity of copper nanoparticle thin films annealed at low temperature,” *Thin Solid Films,* vol. 518, no. 23, pp. 7033-7037, 2010.

المنارة للاستشارات
www.manaraa.com

[195] W. H. Chung, Y. T. Hwang, S. H. Lee, and H. S. Kim, "Electrical wire explosion process of copper/silver hybrid nano-particle ink and its sintering via flash white light to achieve high electrical conductivity," *Nanotechnology,* vol. 27, no. 20, pp. 205704, 20 May, 2016.

[196] K. M. M. A. El-Nour, A. Eftaiha, A. Al-Warthan, and R. A. A. Ammar, "Synthesis and applications of silver nanoparticles," *Arabian Journal of Chemistry,* vol. 3, no. 3, pp. 135-140, 2010.

[197] F. E. Kruis, H. Fissan, and A. Peleda, "Synthesis of nanoparticles in the gas phase for electronic, optical and magnetic applications-a review," *Journal of Aerosol Science,* vol. 29, no. 5-6, pp. 511-535, 1 June, 1998.

[198] M. T. Swihart, "Vapor-phase synthesis of nanoparticles," *Current Opinion in Colloid & Interface Science,* vol. 8, no. 1, pp. 127-133, 2003.

[199] C. B. Murray, C. R. Kagan, and M. G. Bawendi, "Synthesis and characterization of monodisperse nanocrystals and close-packed nanocrystal assemblies," *Annual Review of Materials Science,* vol. 30, no. 1, pp. 545-610, August, 2000.

[200] T. Trindade, P. O'Brien, and N. L. Pickett, "Nanocrystalline semiconductors: Synthesis, properties, and perspectives," *Chemistry of Materials,* vol. 13, no. 11, pp. 3843-3858, 2001.

[201] B. K. Park, S. Jeong, D. Kim, J. Moon, S. Lim, and J. S. Kim, "Synthesis and size control of monodisperse copper nanoparticles by polyol method," *Journal of Colloid and Interface Science,* vol. 311, no. 2, pp. 417-424, 15 July, 2007.

[202] Y. Akada, H. Tatsumi, T. Yamaguchi, A. Hirose, T. Morita, and E. Ide, "Interfacial bonding mechanism using silver metallo-organic nanoparticles to bulk metals and observation of sintering behavior," *Materials Transactions,* vol. 49, no. 7, pp. 1537-1545, 2008.

[203] K. Ankireddy, S. Vunnam, J. Kellar, and W. Cross, "Highly conductive short chain carboxylic acid encapsulated silver nanoparticle based inks for direct write technology applications," *Journal of Materials Chemistry C,* vol. 1, no. 3, pp. 572-579, 2013.

[204] X. L. Qiu, Y. Cao, T. S. Lin, P. He, J. Wang, P. Liu, and X. L. Gu, "Large-scale synthesis of silver nanoparticles by aqueous reduction for low-temperature sintering bonding," *Journal of Nanomaterials,* vol. 2014, pp. 1-8, 21 May, 2014.

[205] A. G. Skirtach, A. A. Antipov, D. G. Shchukin, and G. B. Sukhorukov, "Remote activation of capsules containing Ag nanoparticles and IR dye by laser light," *Langmuir* vol. 20, no. 17, pp. 6988-6992, 2004.

المنارة للاستشارات

www.manaraa.com

[206] R. G. Chaudhuri, and S. Paria, “Core/shell nanoparticles: Classes, properties, synthesis mechanisms, characterization, and applications,” *Chemical Reviews,* vol. 112, no. 4, pp. 2373-2433, 11 April, 2012.

[207] Q. H. Tran, V. Q. Nguyen, and A. T. Le, “Silver nanoparticles: Synthesis, properties, toxicology, applications and perspectives,” *Advances in Natural Sciences: Nanoscience and Nanotechnology,* vol. 4, no. 3, pp. 033001, 14 May, 2013.

[208] K. S. Moon, H. Dong, R. Maric, S. Pothukuchi, A. Hunt, Y. Li, and C. P. Wong, “Thermal behavior of silver nanoparticles for low-temperature interconnect applications,” *Journal of Electronic Materials,* vol. 34, no. 2, pp. 168-175, February, 2005.

[209] D. Kim, and J. Moon, “Highly conductive ink jet printed films of nanosilver particles for printable electronics,” *Electrochemical and Solid-State Letters,* vol. 8, no. 11, pp. J30-33, 2005.

[210] T. H. J. van Osch, J. Perelaer, A. W. M. de Laat, and U. S. Schubert, “Inkjet printing of narrow conductive tracks on untreated polymeric substrates,” *Advanced Materials,* vol. 20, no. 2, pp. 343-345, 2008.

[211] M. L. Allen, M. Aronniemi, T. Mattila, A. Alastalo, K. Ojanpera, M. Suhonen, and H. Seppa, “Electrical sintering of nanoparticle structures,” *Nanotechnology,* vol. 19, no. 17, pp. 175201, 30 April, 2008.

[212] Y. Noguchi, T. Sekitani, T. Yokota, and T. Someya, “Direct inkjet printing of silver electrodes on organic semiconductors for thin-film transistors with top contact geometry,” *Applied Physics Letters,* vol. 93, no. 4, pp. 043303, 2008.

[213] S. H. Ko, H. Pan, C. P. Grigoropoulos, C. K. Luscombe, J. M. J. Fréchet, and D. Poulikakos, “Air stable high resolution organic transistors by selective laser sintering of ink-jet printed metal nanoparticles,” *Applied Physics Letters,* vol. 90, no. 14, pp. 141103, 2007.

[214] S. Magdassi, M. Grouchko, O. Berezin, and A. Kamyshny, “Triggering the sintering of silver nanoparticles at room temperature,” *ACS Nano,* vol. 4, no. 4, pp. 1943-1948, 7 April, 2010.

[215] J. Perelaer, P. J. Smith, D. Mager, D. Soltman, S. K. Volkman, V. Subramanian, J. G. Korvink, and U. S. Schubert, “Printed electronics: the challenges involved in printing devices, interconnects, and contacts based on inorganic materials,” *Journal of Materials Chemistry,* vol. 20, no. 39, pp. 8446-8453, 2010.

[216] J. G. Bai, Z. Z. Zhang, J. N. Calata, and G. Q. Lu, “Low-temperature sintered nanoscale silver as a novel semiconductor device-metallized substrate interconnect

المنارة للاستشارات
www.manaraa.com

material," *IEEE Transactions on Components and Packaging Technologies,* vol. 29, no. 3, pp. 589-593, September, 2006.

[217] M. Jakubowska, M. Jarosz, K. Kiełbasinski, and A. Młożniak, "New conductive thick-film paste based on silver nanopowder for high power and high temperature applications," *Microelectronics Reliability,* vol. 51, no. 7, pp. 1235-1240, 2011.

[218] D. V. Goia, "Preparation and formation mechanisms of uniform metallic particles in homogeneous solutions," *Journal of Materials Chemistry,* vol. 14, no. 4, pp. 451-458, 2004.

[219] L. W. Huang, "Sintering metal nanoparticle films," Mechanical Engineering, Binghamton University, Binghamton, NY, 2012.

[220] T. Kumpulainen, J. Pekkanen, J. Valkama, J. Laakso, R. Tuokko, and M. Mäntysalo, "Low temperature nanoparticle sintering with continuous wave and pulse lasers," *Optics & Laser Technology,* vol. 43, no. 3, pp. 570-576, 2011.

[221] K. Mylsamy, and I. Rajendran, "The mechanical properties, deformation and thermomechanical properties of alkali treated and untreated Agave continuous fibre reinforced epoxy composites," *Materials and Design,* vol. 32, no. 5, pp. 3076-3084, 2011.

[222] U. Holzwarth, and N. Gibson, "The Scherrer equation versus the 'Debye-Scherrer equation'," *Nature Nanotechnology,* vol. 6, no. 9, pp. 534, 28 August, 2011.

[223] M. Y. Fan, L. Wei, Z. Z. He, W. Wei, and X. N. Lu, "Defect inspection of solder bumps using the scanning acoustic microscopy and fuzzy SVM algorithm," *Microelectronics Reliability,* vol. 65, pp. 192-197, 2016.

[224] A. Khaled, S. Brand, M. Kögel, T. Appenroth, and I. De Wolf, "Investigating stress measurement capabilities of GHz scanning acoustic microscopy for 3D failure analysis," *Microelectronics Reliability,* vol. 64, pp. 336-340, 2016.

[225] K. Zaraska, J. Gaudyn, A. Bienkowski, M. Dohnalik, and A. Czerwinski, "X-ray inspection of LTCC devices: Theory and practice," *Journal of Microelectronics and Electronic Packaging,* vol. 8, pp. 49-57, 2011.

[226] F. W. Maur, "Detecting amd analyzing wafer bump voids with X-ray inspection," in 6th International Conference on Electronic Packaging Technology, Shenzhen, China, 2005.

[227] D. Mery, *Computer Vision for X-ray Testing*, Santiago, Chile: Springer, 2015.

المنارة للاستشارات
www.manaraa.com

[228] E. Ide, S. Angata, A. Hirose, and K. F. Kobayashi, "Metal-metal bonding process using Ag metallo-organic nanoparticles," *Acta Materialia,* vol. 53, no. 8, pp. 2385-2393, 2005.

[229] N. E. Resources. " Materials and Processes," https://www.nde-ed.org/EducationResources/CommunityCollege/Materials/Mechanical/Loading.htm.

[230] T. M. Nelson, and R. W. Smith, "Scanning acoustic microscopy," *Advanced Materials and Processes,* vol. 162, no. 12, pp. 29-32, December, 2004.

[231] A. Gowda, D. Esler, S. Tonapi, K. Nagarkar, and K. Srihari, "Voids in thermal interface material layers and their effect on thermal performance," in 6th Electronics Packaging Technology Conference, Singapore, 2004, pp. 41-46.

[232] *Dage 4000 bondtester*, Nordson Company, Aylesbury, UK.

[233] D. Davidson, "Fluid dynamics and heat transfer considerations for gel thermal interface materials," Mechanical Engineering, Binghamton University, Binghamton, NY, 2006.

[234] *Characteristics of thermal interface materials*, 3M Company, St. Paul, MN, 2001.

[235] *TPN-68 Thermal diffusivity by the flash method*, TA Instruments, Springfield, VA, 2012.

[236] D. Davidson, *Documentation for ASTM-D5470-style thermal interface material test device in ADL*, Binghamton University, Binghamton, NY, 2013.

[237] *Flashline operation and maintenance manual*, Anter Corporation, Pittsburgh, PA, 2005.

[238] *Differential Scanning Calorimeter: Getting Started Giude*, TA Instrument, New Castle, DE, 2007.

[239] M. Khaliji Oskouei, and Z. Tamainot-Telto, "Effect of packing density on thermal properties of granular activated carbon packed bed by using of inverse heat conduction method," in 10th International Conference on Heat Transfer, Fluid Mechanics and Thermodynamics, Orlando, FL, 2014, pp. 944-948.

[240] S. A. Faroughi, and C. Huber, "Effective thermal conductivity of metal and non-metal particulate composites with interfacial thermal resistance at high volume fraction of nano to macro-sized spheres," *Journal of Applied Physics,* vol. 117, no. 5, pp. 055104, 2015.

المنارة للاستشارات

www.manaraa.com